Doctoral Dissertations   Graduate School

Summer 2012

A nanostructured Fabry-Perot interferometer for label-free biodetection

Tianhua Zhang

A NANOSTRUCTURED FABRY-PEROT

INTERFEROMETER FOR LABEL-

FREE BIODETECTION

by

Tianhua Zhang, B. E., M. S.

A Dissertation Presented in Partial Fulfillment
of the Requirements of the Degree
Doctor of Philosophy

COLLEGE OF ENGINEERING AND SCIENCE
LOUISIANA TECH UNIVERSITY

August 2012

UMI Number: 3533096

UMI®

Dissertation Publishing

ProQuest®

LOUISIANA TECH UNIVERSITY

THE GRADUATE SCHOOL

MARCH 19, 2012

Date

We hereby recommend that the dissertation prepared under our supervision
by Tianhua Zhang, M.S.

entitled

A Nanostructured Fabry-Perot Interferometer for Label-Free Biodetection

be accepted in partial fulfillment of the requirements for the Degree of
Doctor of Philosophy

Supervisor of Dissertation Research
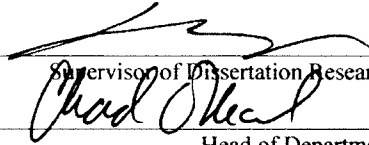
Head of Department

Engineering

Department

Recommendation concurred in:

Advisory Committee

Approved:

Director of Graduate Studies

Dean of the College

Approved:

Dean of the Graduate School

ABSTRACT

A polymer nanostructured Fabry-Perot interferometer (FPI) based biosensor has been developed, fabricated, and tested. Different from a conventional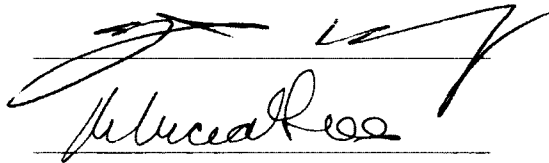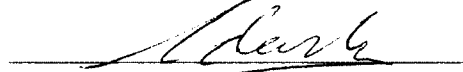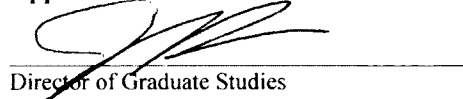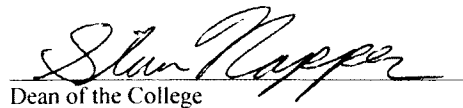 FPI, this nanostructured FPI has a layer of Au-coated nanopores inside its cavity. The Au-coated nanostructure layer offers significant enhancement of optical transducing signals due to the localized surface Plasmon resonance (L-SPR) effect. Compared to a traditional FPI for label-free biosensing applications, the polymer nanostructured FPI based biosensor offers increased sensing surface area, extended penetration depth of the excitation light, and amplification of optical transducing signals. Using a nanostructured FPI, measurements taken had great improvements in free spectral range (FSR), finesse, and contrast of optical transducing signals over a traditional FPI without any device performance optimization.

Several chemicals have been evaluated using the prototype device. Fourier Transform has been performed on the measured optical signals to facilitate the analysis of the transducing signals. Control experiments incubating immunoglobulin G (IgG) on a gold surface confirmed the small affinity of IgG to the Au-coated sensing surface. Then, using fluorescent images, shifts of interference fringes for IgG and BSA interaction were indirectly confirmed.

Using this technical platform, the immobilization of capture proteins (Protein A) on the nanostructure layer and their binding with IgG was monitored in real time,

resulting in the direct observation of the shift in interference fringes of the optical transducing signals. The results showed that the detectionof limit (DOL) for this kind of biosensor should be lower than 10 pg/mL, which is approximately 55 fM of IgG, for IgG-Protein A binding. Control experiments were performed to confirm that the biodetection is only specific to Protein A and IgG recognition.

After the proof-of-concept demonstration for IgG-Protein A binding, the ultrasensitive label-free detection of a cancer biomarker free prostate specific antigen (f-PSA) using this kind of nanostructured FPI was carried out. Experiments found that the DOL of the fabricated nanostructured FPI microchip for f-PSA is about 5 pg/mL and the upper detection range for f-PSA can be dynamically changed by varying the amount of mAb immobilized on the sensing surface. Control experiments have also demonstrated that the immunoassay protocol used shows excellent specificity and selectivity, suggesting great potential to detect cancer biomarkers at trace levels in biofluids.

Given its nature of low cost, simple operation, and batch fabrication capability, the nanostructured FPI microchip based platform could provide an ideal technical tool for point-of-care diagnostic applications and anti-cancer drug screening and discovery.

APPROVAL FOR SCHOLARLY DISSEMINATION

The author grants to the Prescott Memorial Library of Louisiana Tech University the right to reproduce, by appropriate methods, upon request, any or all portions of this Dissertation. It is understood that "proper request" consists of the agreement, on the part of the requesting party, that said reproduction is for his personal use and that subsequent reproduction will not occur without written approval of the author of this Dissertation. Further, any portions of the Dissertation used in books, papers, and other works must be appropriately referenced to this Dissertation.

Finally, the author of this Dissertation reserves the right to publish freely, in the literature, at any time, any or all portions of this Dissertation.
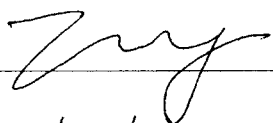
Author _____

Date ___07/27/2012___

TABLE OF CONTENTS

LIST OF FIGURES

LIST OF TABLES

ACKNOWLEDGMENTS

I wish to express my sincere gratitude to my mentor and advisor, Dr. Long Que, for giving me this opportunity to study and do research in one of the best research institutions in the world, for the generous sharing of his profound knowledge with me, for his time and guidance. Throughout my doctoral study and research, he encouraged me to be independent and professional in research, academy and profession.

I especially thank Dr. Chester Wilson, Dr. Rebecca R. Giorno, Dr. Shengnian Wang, and Dr. Adarsh D. Radadia for their guidance and for serving on my advisory committee for this dissertation.

I wish to thank Dr. Weimin Sun who introduced my doctoral research in the U. S. and Dr. Jianjun Wei for his helpful advice and generous time during my doctoral research.

I am also grateful to work with my colleagues Dr. Zhongcheng Gong, Mr. Siva Prasad Raju, Mr. Venu Kotipalli, Mr. Shantan Talla, Mr. Pushparaj Pathak, Mr. Shashi Yadav, Mr. Sukrut Karandikar, Mr. John Sweeney, Mr. Yuan He, Mr. Yi-Hsuan Tseng, Mr. Xiang Li, and my friends Miss Krystal Sno Corbett, Mr. Bryan Cox, and Mr. William Clower for their much useful advice and support.

I thank IfM staff members, Mr. Ji Fang, Mr. Alfred Gunasekaran, and Mrs. Debbie Wood for the experimental support.

Finally, I would like to thank my family. My parents and grandparents have supported and encouraged me with their love and patience throughout my life.

CHAPTER 1

INTRODUCTION

1.1 Overview of Biosensors

The human body is a perfect biosensing system. It can sense light, sound, smell, taste and touch by means of eyes, ears, nose, tongue, and fingers, respectively. For thousands of years, people have tried to mimic the function of the human body, with temperature sensors in refrigerators and airconditioners, gas sensors in gas-ovens, infrared sensors in televisions, speed sensors in vehicles, and so on.

The first description of a biosensor was given by Leland C. Clark in 1962 as "a device that transforms chemical information, ranging from the concentration of a specific sample component to total composition analysis, into an analytically useful signal. Chemical sensors usually contain two basic components connected in series: a chemical (molecular) recognition system (receptor) and a physicochemical transducer. Biosensors are chemical sensors in which the recognition system utilizes a biochemical mechanism" [1]. Thereafter, there has been an explosive growth of research on biosensors [2-5], which have been used for a wide variety of applications such as environmental monitoring, biomedical, and biological research.

According to the International Union of Pure and Applied Chemistry (IUPAC), a biosensor is defined as a self-contained device, integrated with a biological recognition element and a transducing element [6]. Since biosensors have evolved over the past five

decades, this definition is no longer appropriate. A more "modern" definition of biosensor is given by Newman et al. as "a compact analytical device incorporating a biological or biologically-derived sensing element either integrated within or intimately associated with a physicochemical transducer" [7].

Abiosensor consists of analyte, bioreceptor, transducer, and signal detector [8]. The component of the biosensor is shown in Figure 1.1.
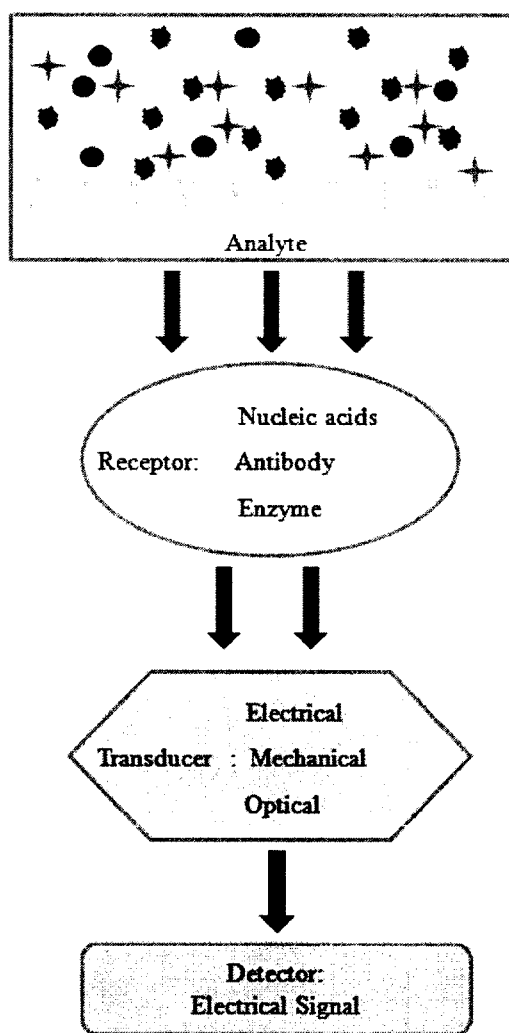
Figure 1.1 Biosensor components [7].

Analytes are chemical substances whose properties are measured for analytical purposes. Receptors are responsible for immobilizing analytes on the surface of a transducer. They include the antibody, enzyme, nucleic acid, etc. Antibodies are specific to certain antigens. The interaction between an antibody and an antigen is just like the relationship between a lock and a key. A specific antibody can only bind with a specific antigen, and enzymes have specific binding capabilities. Enzymes are also well known for their catalytic activities. In enzyme bioreceptor recognition, the detection is usually enhanced by catalyzed reaction. By using an enzyme cascade, the catalyzed reaction can be greatly amplified [9]. Nucleic acid is another type of bioreceptor. During the past two decades, with the emerging of deoxyribonucleic acid (DNA) and ribonucleic acid (RNA), which are the basis of genetics, scientists and researchers have shown more and more interest in nucleic acids [10-15]. There are adenine : thymine (A : T) and cytosine : guanine (C : G) pairs in DNA. They are the basis of the nucleic acid recognition. Knowing one part of the pair, the other part can be synthesized which is usually identified with labels such as fluorescent dyes. Transducers are components that transform signals from one form to another that can be detected such as electrical, mechanical or optical signals. Detectors are components that recover bio transducing signals and transform them into electrical, mechanical or optical signals that can show information of interest for analytical purposes.

Biomolecules are very small, weighted from less than 100 daltons to over 1,000 daltons. The typical size is from a few nanometers to a few microns, as shown in Figure 1.2.

4

Eyesight limit

1mm	100μm	10μm	1μm	100nm	10nm	1nm	0.1nm
10^{-3}m	10^{-4}m	10^{-5}m	10^{-6}m	10^{-7} m	10^{-8}m	10^{-9}m	10^{-10}m

Ant   Hair   Bacteria   Virus   Protein   DNA   Atoms
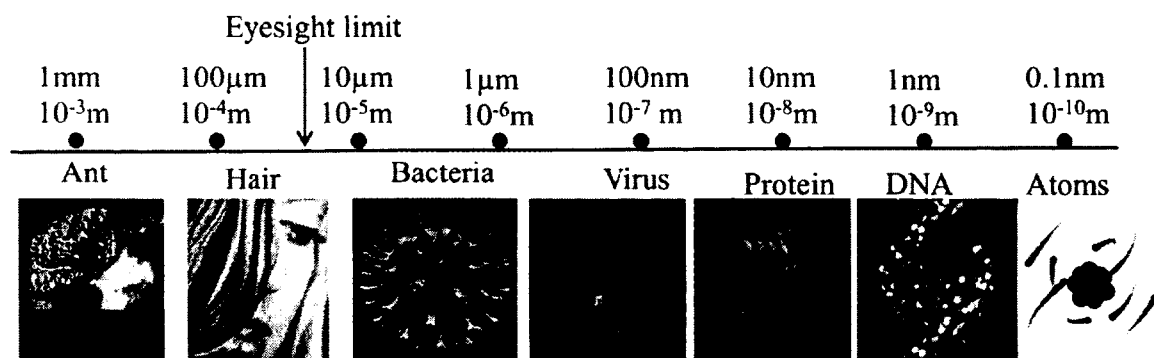
Figure 1.2 Scale sizes of biomolecules [10-15]

Transducing signals from biomolecules are very weak. In order to measure weak signals from small biomolecules, devices with nano- or microscale are needed. To this end, micro- and nanotechnologies have started to play a very important role in the enhancement of the sensitivity and DOL of biosensing technologies. Representative technologies include fluorescence [16], light scattering [17, 18], surface enhanced Raman spectroscopy (SERS) [19], surface Plasmon resonance (SPR) [20], photonic crystal [21, 22], electrochemical immunosensing electrode [23], quartz crystal microbalance [24], (micro-) nanocantilever [25, 26], nanowire [27, 28], carbon nanotube [29], nanoparticle based localized SPR [30], nanohole and array [31], quantum dot [32, 33], magneto-nanosensor [34], nanopore thin film [35, 36] technologies. Furthermore, recent technical advancement in nanofabrication, nanomaterial synthesis, micro/nanofluidics and bioassay has also enhanced the sensitivity or chip adaptability for the detection and quantification of protein biomarkers in biological samples via the binding to antibodies or aptamers [37].

Biosensing can be realized by either the labeled or the label-free technique [38-41]. The labeled biosensors require such labels as fluorescent dyes, radioisotopes, epitope tags [42-44] to be attached to the analytes in order to identify whether or not there are interactions. However, this technology has its own shortcomings such as the limited shelf

life of labels, the inherent toxicity caused by the labels which could also modify the properties of biomolecules and the need for specific read-out instrumentswith intelligent software and skilled lab personnel [8, 41].

In contrast to labeled biosensing, the label-free technique is attractive for biosensing since no labels such as fluorescent dyes need to be attached to the biomolecules. As a result, the experimental cost can be reduced dramatically, and the possible perturbation of properties of biomolecules can be completely avoided. Label-free biosensing is a very important and efficient technique for environmental monitoring, biomedical, and biological research applications.

1.2   Label-Free Biosensors

There are three main categories of label-free biosensors in terms of transducing mechanisms, as shown in Figure 1.3. These transducing mechanisms include electrical, mechanical, and optical responses [27, 45, 46].
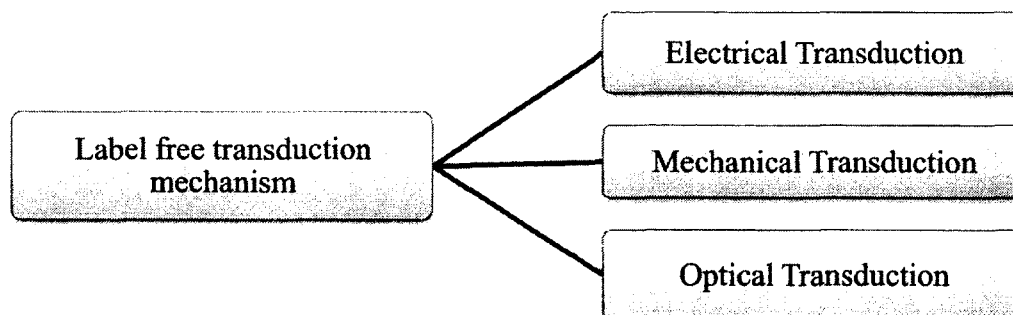
Figure 1.3 Classification of label free biosensors.

1.2.1   Electrical Label-Free
         Biosensors

Electrical transduction is enabled by carbon nanotubes (CNTs) or nanowires

(NWs) where the electrical conductance of the CNTs or NWs changes upon the binding

between the receptors (antibodies-Abs) immobilized on them and the targets (antigens-

Ags). For example, the schematic of a NW based biosensor is shown in Figure 1.4.
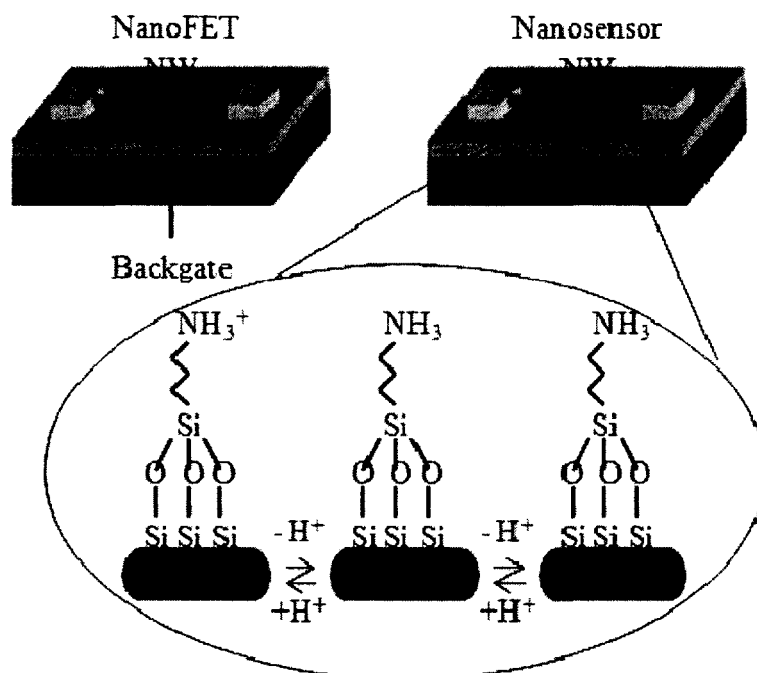
Figure 1.4 Schematic of a NW based biosensor [47].

The receptors (Abs) are first immobilized on NWs. Then, the targets (Ags) bind

with the receptors. The electrical conductance of the NWs changes upon the binding

between the receptors immobilized on them and the targets [27, 48, 49].

1.2.2   Mechanical Label-Free
         Biosensors

Mechanical transduction is achieved by MEMS (Microelectromechanical systems)

or NEMS (Nanoelectromechanical systems) cantilevers where the binding between an

antigentic target and an antibody immobilized cantilever surface changes the surface stress of the cantilever, resulting in its bending and the shifting of the resonant frequency. For example, the schematic of a MEMS cantilever based biosensor is shown in Figure 1.5.
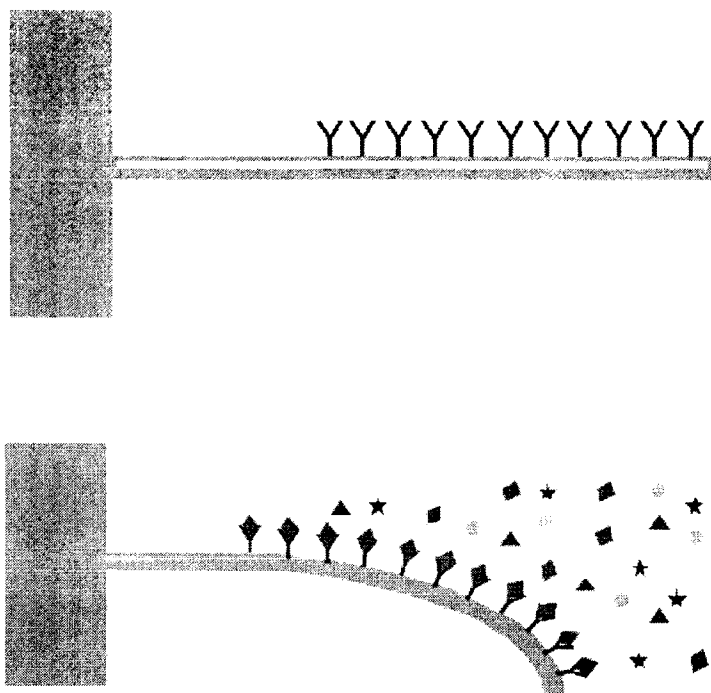
Figure 1.5 Schematic of a MEMS cantilever based biosensor [50].

The receptors (Abs) are first immobilized on the tips of the MEMS cantilever. Then, the targets (Ags) bind with the receptors. The binding between an antigentic target and an antibody immobilized cantilever surface changes the surface stress of the cantilever, resulting in its bending and the shifting of resonant frequency [50].

1.2.3   Optical Label-Free
         Biosensors

Due to its non-invasive nature, high degree of sensitivity, capability of multiplexing, and immunity to environmental noise, the optical technique is very attractive for sensing applications. As nanotechnology has undergone explosive growth in

the past two decades, many optical components or systems such as lenses, gratings, mirrors, microring resonators, and interferometers have, therefore, been miniaturized for various sensing applications [51-56]. As a result, the field of microoptics and nanooptics has emerged, triggering extensive research to scale down the optics-based sensing platforms over the past decades. Optical label-free transduction can be achieved by such techniques as propagating surface Plasmon resonance (PSPR) [57], Raman spectroscopy [58], surface enhanced Raman spectroscopy (SERS) [59], localized SPR (L-SPR) [35], liquid core optical ring resonator (LCORR) [60], photonic crystal (PC) nanostructures [58, 61], light scattering, quantum dots, microspheres [58], opto-fluidic ring resonators [59], microring resonators [60], and thin film interferometric devices [35, 36]. These technologies can provide exceptional sensitivity. Some of them can even offer DOL down to the single molecular level, thus having great potential for the early stage detection of cancer/disease biomarkers. Specifically, using these technologies, the detection of a variety of disease biomarkers such as carcinoembryonic antigen (CEA) for colon cancer, prostate-specific antigen (PSA) for prostate cancer, HER2 for breast cancer and amyloid-beta derived diffusible ligands (ADDLs) for Alzheimer's disease has been demonstrated and reported [59, 60].

Surface plasmons (SP) can beexcited on a metal and dielectric interface by a monochromatic or nearmonochromatic optical source. Usually, a noble metal (gold, silver or platinum) thin film (50-100 nm) is coated on the surface of the substrate such as a glass slide or a prism, as shown in Figure 1.6.
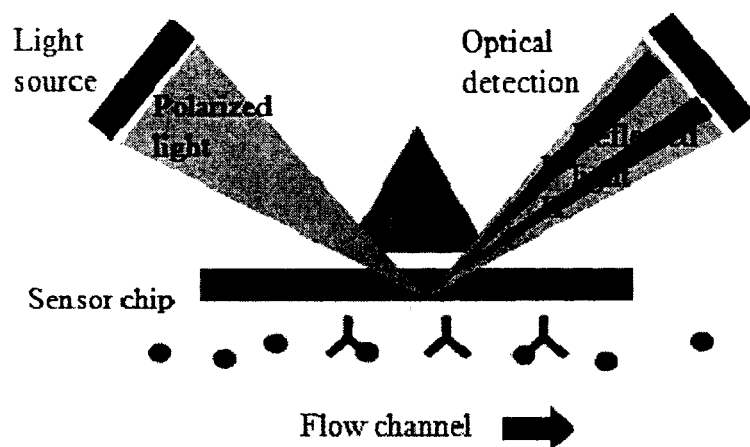
Figure 1.6 Schematic of a PSPR based label free biosensor [62].

The fields associated with the SP extend into the medium adjacent to the interface and decay exponentially away from it. The penetration into the medium is in the range of <100-200 nm. Consequently, the SP is very sensitive to changes in thickness or refractive index in the environment near the interface between the metal and dielectric layers, and therefore, is used as a sensing probe. Beyond this range, the biomolecules can hardly be detected. Upon the excitation of the SPR, a valley in reflectance from the interface occurs. The position of the valley shifts to a different angle of incidence given any changes in the local environment at the interface. The SPR technique has seen tremendous growth over the past decades and has been used for a variety of applications such as drug discovery and homeland security [62].

Recently, LCORR technology has been demonstrated for multiplexed biosensing by placing LCORR in contact with multiple anti-resonant reflecting optical waveguides (ARROWs). It utilizes the ARROWs to excite the whispering gallery modes of a LCORR sensor [63]. The schematic of a LCORR based label-free biosensor is shown in Figure 1.7.
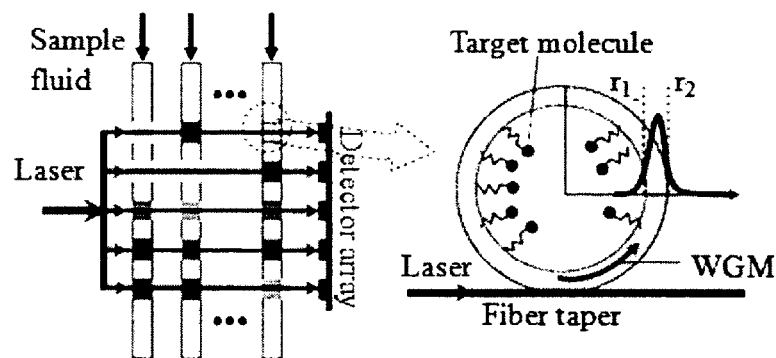
Figure 1.7 Schematic of a LCORR based label-free biosensor [63].

One type of photonic crystal (PC) biosensors consists of a silicon waveguide adjacent to 1D photonic crystal microcavity [64], which is evanescently coupled to each other [21]. A change in the refractive index of the near field region surrounding the optical cavity results in a shift of the resonant wavelength, as shown in Figure 1.8.
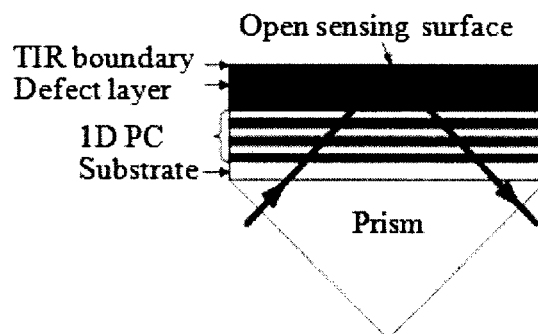
Figure 1.8 Schematic of a PC based label-free biosensor [64].

Microsphere biosensors utilize the whispering gallery modes (WGMs) technique for the detection and analysis of microorganisms. The recirculation of photons in the cavities of the microsphere can tremendously enhance the signal of the evanescent wave between the microsphere and the surrounding medium. The enhancement of the evanescent field can be exploited for ultrasensitive biodetection [58]. Using microsphere technology, label-free biodetection can be achieved by measuring the shift of resonance

frequency before and after the biosample is immobilized on the surface of the microsphere. However, specific detections of biomaterials need treatment or modification of the mircrosphere cavity surface.

Porous silicon and alumina thin film interferometry for label-free DNA and protein interaction biodetection were pioneered by Sailor and co-workers [35, 65], yet engineering efforts are still needed for nanopore thin film sensors to achieve microfluidics-based multiplexed biosensing. A very important example of interferometric device is Fabry-Perot interferometer (FPI). FPIs have been designed, micromachined, and implemented for chemical sensing, gas sensing, ultrasonic sensing, and as optical modulators [51, 52]. As a chemical and gas sensor, the FP cavity serves as a sensing area. The output signals reflect or transmit intensity through FPI, which changes with different chemicals [51, 52]. For ultrasonic sensing, the micromachined capacitive acoustic transducer consists of an FPI cavity with embedded optical diffraction gratings on a transparent substrate. The detection sensitivity can be maintained at an optimum level by deflecting the membrane of the FPI. For optical modulation, an FPI contains a cross-linked electro-optic polymer inside its cavity, offering the potential for high time-bandwidth modulation.

Various MEMS actuation mechanisms make some unique features of a μFPI possible. For instance, tunable μFPIs have been demonstrated with electrostatic and thermal actuators. They have been exploited and utilized for wavelength division multiplexing (WDM) in optical communications [53] and Raman spectroscopy [54], oxygen detection in blood sample [55], and spectral endoscope optical imaging [56]. For WDM application, tunable μFPI serves as a tunable filter, selecting different wavelengths

by changing the gap size of the FPI cavity. For oxygen detection in blood samples, the proposed μFPI device can detect a wide range of wavelength from visible to near infrared light, offering sufficient characteristics to analyze the spectrum of the blood [55]. For spectral endoscope optical imaging, the device can acquire spectral images of a target at each pixel [56]. Recently, μFPI has been used to study nanoscale fluid dynamics, indicating its potential for nanoscience and nanotechnology research.

Usually, μFPIs are fabricated from silicon, polysilicon, silicon nitride, silicon oxide thin film or other semiconductor materials and are often operated by a laser source. In order to further simplify the operational procedure and lower the cost, recently a white-light source operated polymer FPI has been developed for (bio-) chemical sensing by our group.

A FPI sensor is usually based on the principle of multiplebeam interference. In order to show the basic principle of a FPI sensor, a simplified FPI sensor is demonstrated. The refractive index inside an FPI sensor is related to its density, composition, pressure and temperature. The structure of a conventional FPI sensor is shown in Figure 1.9.
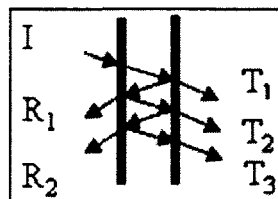
Figure 1.9 Structure of a conventional FPI sensor.

I is the input light, R_1, R_2, $\wedge$ are reflected light and E_1, E_2, E_3, $\wedge$ are transmitted light. Optical fibers are used to collect reflected light into a spectrometer and the cavity is formed by two metal coated mirrors. However, this structure results in high coupling loss

when reflected light is coupled into optical fibers and low resolution [66]. The metal

coated mirror on one end is usually used as the input end of light and the other coated

mirror as the feedback mirror. In order to introduce the model, basic theories and

methods must be described. One must consider two parallel transparent plates of

refractive index n_1, surrounded by a medium of refractive index n_2, and suppose that a

plane wave of monochromatic light shines on the plate at incident angle θ. The

corresponding phase difference is

$$\delta = \frac{4\pi}{\lambda} n_1 h \cos\theta, \tag{1-1}$$

where h is the thickness of the plate and λ is the wavelength in vacuum. Let E_0 be the

amplitude of the electric vector of the incident wave, complex amplitudes of the waves

reflected from the plate are rE_0, $tt'r'E_0 e^{i\delta}$, $tt'r'^3 E_0 e^{2i\delta}$, $\wedge$, $tt'r'^{(2p-3)} E_0 e^{i(p-1)\delta}$, $\wedge$, where

r is the reflection coefficient, t is the transmission coefficient for a wave incident from the

surrounding medium toward the plate, and r' and t' are the corresponding quantities for

waves traveling from the plate toward surrounding medium [66, 67]. The ratio of

reflected light intensity to incident light intensity is

$$R = \frac{4r^2 \sin^2 \frac{\delta}{2}}{(1-r^2)^2 + 4r^2 \sin^2 \frac{\delta}{2}}. \tag{1-2}$$

Finesse is a key parameter of FPI. It is defined as the distance between the

interference peaks $\Delta\lambda$, divided by the full width half maximum (FWHM) $\delta\lambda$ of the

peaks. Conceptually, finesse can be thought of as the number of interfering beams within

the Fabry-Perot cavity, as illustrated in Figure 1.10.
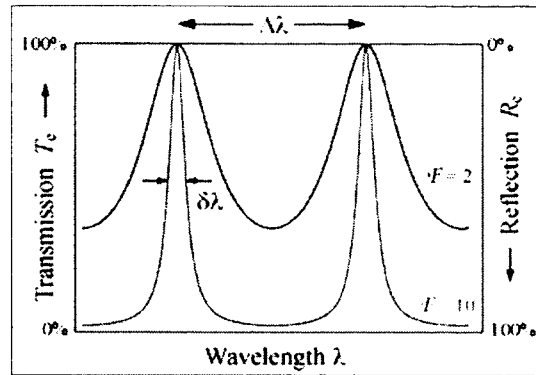
Figure 1.10 Transmission spectrum of a FPI [67].

The slope of the constructive peak is determined by finesse. The larger the finesse value, the sharper the constructive peak and the larger the distance between two separate peaks, which means a higher resolution. The original finesse depends solely on the mirror reflectance in an ideal FPI and is commonly approximated (for $R > 0.5$) by

$$N_R = \frac{\pi \cdot \sqrt{R}}{1 - R}.$$

(1-3)

The higher the reflectance, the larger the finesse. The finesse can be degraded by the defects of the mirror, such as imperfect flatness and imperfect parallelism [66, 67].

The ratio of the energy of reflected light to incident light from a dielectric is given by the Fresnel equations. In the case of normal incidence,

$$R = \left| \frac{E_r}{E_i} \right|^2 = (\frac{n_2 - n_1}{n_2 + n_1})^2,$$

(1-4)

where E_r and E_i are reflected and incident spectral intensities, respectively. The spectrometer is the equipment used to measure the reflectance [67].

All of these technologies in the above review have shown excellent detection sensitivity and ultra low DOL. However, these label-free optical techniques are plagued by some or all of the following issues: expensive nanofabrication processes (i. e. PC

sensors), complicated and expensive optical setup for operation (i. e. PC, LCORR, and SPR sensors), and difficulty of miniaturization (i. e. LCORR and SPR sensors) for microfabricating arrayed sensors for multiplexed detection. Even though the traditional µFPI shows elegant sensitivity and performance for various sensing applications, its limitations are obvious: limited sensing area due to the small surface areas of the planar plates of the µFPI, limited penetration depth of the excitation light in the sensing area, and limited intensity of the transducing signal due to the optical power losses of the reflected or transmitted light from the FPI at the interface of air and the FPI plates. These issues contribute to the difficulty of making these platforms cost-effective and compact.

1.3   Previous Work and Problems

A new type of disposable label-free optical biosensors based on micromachined polymer Fabry-Perot interferometers (µFPIs) has been developed [68]. The schematic of a white-light source operated µFPI chemo/biosensor is given in Figure 1.11, showing immobilized antibodies (Abs) on the surface of the Au-coated glass surfaceand the binding between Abs and antigens (Ags).
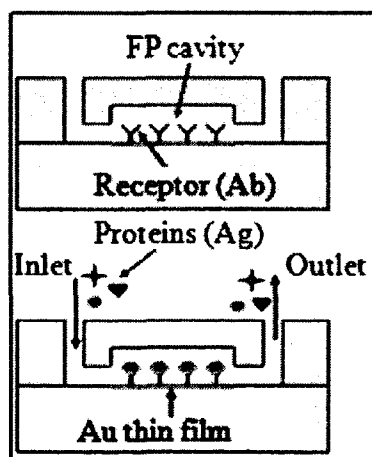
Figure 1.11 Schematic of a PDMS based µFPI chemo/biosensor.

This type of µFPI is fabricated using polydimethylsiloxane (PDMS) plate and a glass plate. The PDMS and glass plates serve as two FPI planar plates. The sensing surface is the glass plate inside the FPI cavity, which is about 100 µm × 100 µm in area. A µFP cavity with a gap of 50 µm is formed between them, serving as the sensing area. At the current stage, both plates do not have any thin film coating to enhance their reflectivity like the traditional macroscale FPI or reported µFPI. The fiber optics based testing setup is illustrated in Figure 1.12.
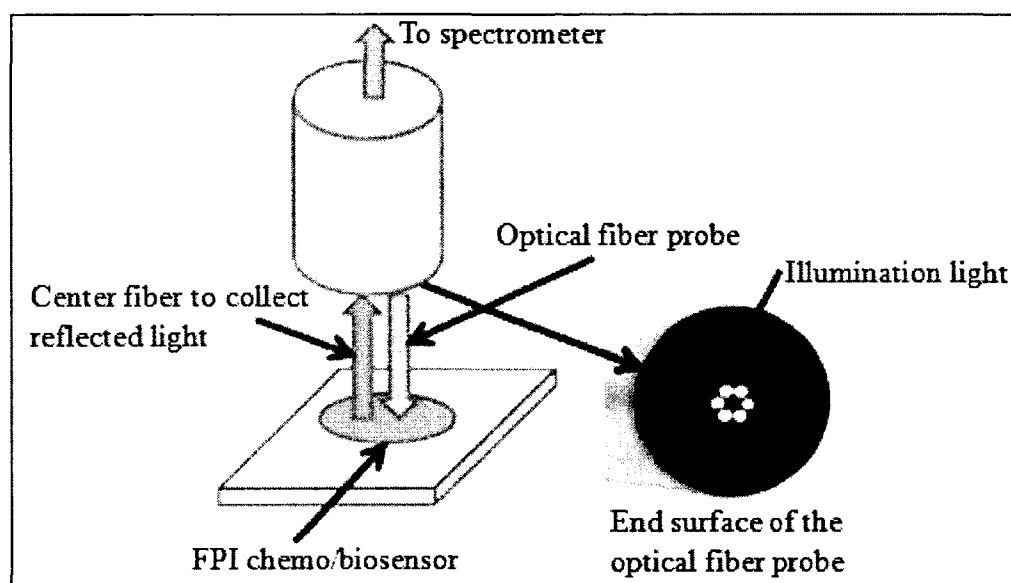
Figure 1.12 Optical setup of a FPI biosensor.

The customized optical fiber probe delivers the white-light to the sensor as well as receiving the reflected transducing signals from the µFPI sensor, which are coupled to a spectrometer. The optical fiber probe consists of a tight bundle of seven optical fibers in a stainless steel ferrule. The center fiber collects the reflected light while the outer six fibers deliver illumination light to the FPI chemo/biosensor.

The operation principle of this sensor is shown in Figure 1.13. Upon entering the FPI cavity, the operation light undergoes multiple internal reflections between the two FPI plates and interferences inside the cavity. The reflected and transmitted light goes through the FPI as output transducing optical signals.
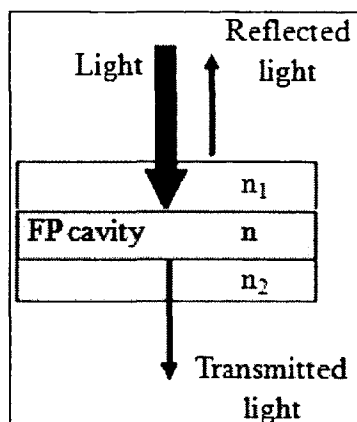
Figure 1.13 Operational principle of a FPI.

As a result, modulated output transducing signals, such as reflected or transmitted interference fringes, are generated as shown in Figure 1.14.
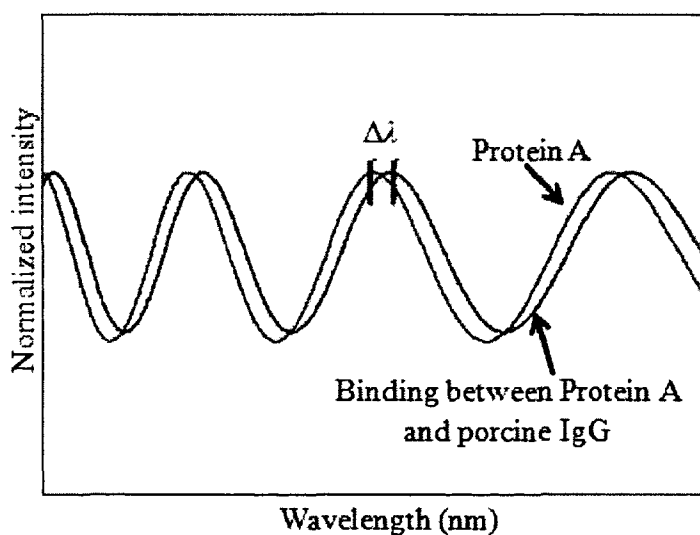
Figure 1.14 Inference fringe shift before and after binding.

The shift is due to the effective index of refraction changes in the FPI cavity with the binding between Protein A and Porcine IgG. More specifically, Protein A molecules serve as the probes and are immobilized on one FPI plate surface. When a variety of IgG antibodies are flowed through the cavity, they bind to Protein A, causing changes of the effective index of refraction. The binding results in the interference fringes shift ($\Delta\lambda$), which serves as the optical transducing signals.

The performance of the FPI is determined by its finesse F, which is related to the free spectra range (FSR=$\Delta\lambda$) and the full-width at half-maximum (FWHM) $\delta\lambda$ [67]. The sketch of the optical system, including the optical fiber and the μFPI for the modeling, is illustrated in Figure 1.15.
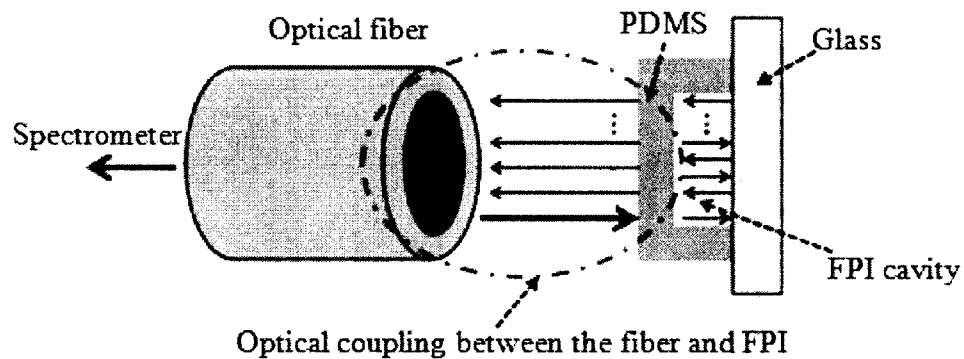
Figure 1.15 Sketch of the optical system.

The system includes the optical fibers and the μFPI device: the indices of refraction of PDMS, medium in FPI cavity and glass are n_1, n_2 and n_3. A customized optical fiber probe delivers the white-light from a tungsten halogen source perpendicularly to a biochemical sensor. This probe also receives the reflected signals from the sensor, which is eventually coupled to a spectrometer [67]. The loss of the optical coupling between the fiber and μFPI sensor needs to be considered.

One may assume the loss coefficient of μFPI cavity is L and the loss between the fiber probe and μFPI is $L_{fiber-FPI}$; then, the reflected intensity I_r from this system, coupled to the spectrometer, is written as,

$$I_r = I_i \exp(-\frac{2(\lambda - \lambda_0)^2}{\omega^2}) \times L_{fiber-FPI} \times f(R_{air-PDMS}, R_{air-glass}), \tag{1-5}$$

where

$$f(R_{air-PDMS}, R_{air-glass}) = \frac{r_2^2 + r_3^2 L_{FPI}^2 - 2r_2 r_3 L_{FPI} \cos(2kn_2 d)}{1 - r_2^2 r_3^2 L_{FPI}^2 - 2r_2 r_3 L_{FPI} \cos(2kn_2 d)}, \tag{1-6}$$

$r_2 = -r_1 = \frac{n_2 - n_1}{n_2 + n_1}$, $r_3 = \frac{n_2 - n_3}{n_2 + n_3}$, $I_i exp(-2(\lambda-\lambda_0)^2/\omega^2)$ is incident light intensity, λ_0 is the center wavelength of the light source, ω is the beam radius at the beam waist, $f(R_{air-PDMS}, R_{air-glass})$ is the reflectivity from the μFPI, $R_{air-PDMS}$ and $R_{air-glass}$ are reflectivities at the interface between air and PDMS, and air and glass, respectively, d is the gap size of FPI cavity, and n_1, n_2 and n_3 are the indices of refraction of PDMS, the medium in FPI cavity, and glass, respectively.

The measured output signal from a μFPI device with air inside its cavity is given in Figure 1.16 based on the model proposed in principle of FPI. The calculated transducing signals with air in the FPI cavity match the measured signals quite well as shown in Figure 1.16. Note that the intensity of the white-light source across the wavelength range, from 360-2,500 nm, is not uniform. The envelope of the interference fringes is the profile of the intensity of the white-light source.
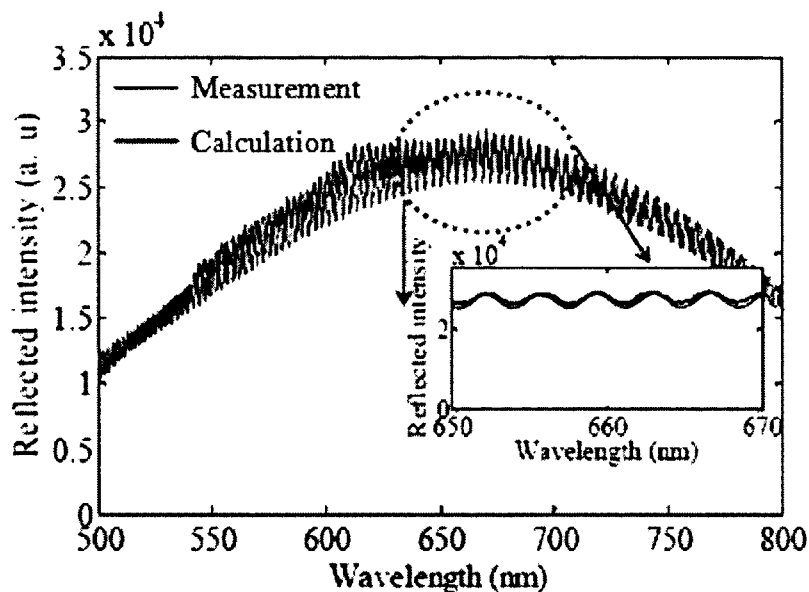
Figure 1.16 Calculated and measured transducing signals.

A protein-protein binding assay has been used to demonstrate the operation and biomolecular detection capability of the polymer based μFPI at room temperature. The measured transducing signals for PBS, immobilized Protein A, Protein A bound with Porcine IgG, Protein A bound with sheep IgG and Protein A bound with rabbit IgG have been tested. The shifts in interference fringes are clearly observed, indicating differences of effective refraction indices of these three different types of IgGs.

In previous work, a polymer based μFPI biochemical sensor had been developed and its biomolecular detection capability demonstrated successfully. The simple, cost effective, and disposable nature of this type of sensor is attractive for point-of-care biodetection applications. The experiments show that DOL of this sensor is between 50 and 5 ng/ml for the rabbit IgG.

However, for biochemical sensing, a conventional μFPI has intrinsic limitations. First, it has a limited sensing surface area (100 μm × 100 μm), which means that binding

sites available for biomolecules are limited, resulting in low transducing signals. Second, the optical sensitive range/area is essentially limited only on the surface of the planar glass plate. Finally, it has a limited intensity of the transducing signals due to the optical power losses of the reflected light from the FPI at the interface of air and the FPI plates. It is highly possible to enhance the sensitivity and detection of limit significantly by introducing some nanostructures inside the FPI cavity [69, 70].

1.4   Dissertation Objectives

The aim of this dissertation research is to develop and investigate a novel nanostructured Fabry-Perot interferometer which is able to realize ultrasensitive label-free biodetection. First, a nanostructured Fabry-Perot interferometer will be introduced and demonstrated. Then, Raman signal enhancement and interferometer signal enhancement based on gold coating nanostructured devices will be demonstrated to enhance optical transducing signals, including improving the finesse, the free spectral range,improving the DOL and enhancing the intensity of output signal. Based on this concept, a nanostructured device will be developed. Proof-of-concept demonstrations using IgG-Protein Abiodetection will be performed first. Thereafter, further experiments and experimental analysis will be carried out for ultrasensitive detection of a cancer biomarker using this technical platform.

1.5   Organization of Dissertation

Chapter1 introduced biosensors and their components and reviewed three major types of label-free transduction mechanisms, which include an electrical biosensing mechanism, a mechanical biosensing mechanism and an optical biosensing mechanism.

Related work of developing biosensors that utilize electrical, mechanical, and optical transductons has been reviewed. Advantages and disadvantages have been investigated by comparing the previous work. Most recent examples of research on polymer based μFPI biosensors and their future have been presented. Chapter 2 will cover the materials and equipment which will be used in later experiments.

Chapter 3 will introduce the design of nanostructured Fabry-Perot interferometer based biosensors and the fabrication process. The prototype device will be evaluated using several chemicals. Fourier transform will be performed on the measured optical signals to facilitate the analysis ofthe transducing signals. Finally, the device will be functionalized for subsequent immunosensing.

Chapter 4 will investigate Raman signal enhancement and interferometer signal enhancement based on gold coating nanostructured devices to enhance optical transducing signals, including improving the finesse, the free spectral range, the DOL, and enhancing the intensity of the output signal. Then, a finite element analysis (FEA) of signal enhancement will be performed to simulate the signal enhancement.

Chapter 5 will indirectly confirm the shifts of interference fringes for label-free biodetectionof IgG and BSA interaction using fluorescent imaging. A control experiment incubating immunoglobulin G (IgG) on gold surface will be carried out to confirm the small affinity of IgG to the gold coated sensing surface.

Chapter 6 will describe and investigate a protein-protein (Protein A and Porcine IgG) binding assay based biosensor using this nanostructured Fabry-Perot interferometer for proof-of-concept demonstration. The DOL will be tested for this biosensing technical platform. Control experiments will be performed to check if Sea Block binds with Protein

A or IgG to confirm that the biodetection is only specific to Protein A and IgG recognition.

Chapter 7 will describe and investigate the application for the ultrasensitive label-free detection of a cancer biomarker using this technical platform. Specifically, the prostate cancer biomarker free prostate-specific antigen (f-PSA) will be detected with a mouse anti-human PSA monoclonal antibody (mAb) as the receptor. The DOL of this nanostructured FPI microchip for f-PSA and the upper detection range for f-PSA will be determined. The control experiments will be carried out to demonstrate that the immunoassay protocol used in the experiments shows excellent specificity and selectivity, suggesting the great potential to detect the cancer biomarkers at trace levels in biofluids.

Chapter 8 will give the conclusion for the dissertation. Recommendations for future work will be further discussed.

CHAPTER 2

MATERIALS AND EQUIPMENT

2.1   Materials

The assay reagents used in the experiments included Protein A (Pierce Biotechnology, Inc.), bovine serum albumin (BSA) (Sigma-Aldrich, Co.), buffer solution phosphate buffered saline (PBS) (Sigma-Aldrich, Co.), Sea Block (Pierce Biotechnology, Inc.), Porcine, Rabbit and Goat IgG (Sigma-Aldrich, Co.) and free-PSA monoclonal antibody (Anogen-YES Biotech Laboratories, Ltd.).

2.1.1   Immunoglobulin G
and Protein A

An antibody is usually a Y-shaped protein with large molecular weight. The foreign targets, such as bacteria and viruses, are called antigens. Due to the existence of antibodies, large foreign molecules, such as antigens, could be detected by theimmune system, neutralized and then cleaned out of the body. Antibodies are specified to their corresponding antigens with high affinity. In the field of clinical research, this feature makes antibodies a good choice of biological agents for treating a variety of diseases [71]. The structure of an antibody is shown in Figure 2.1.
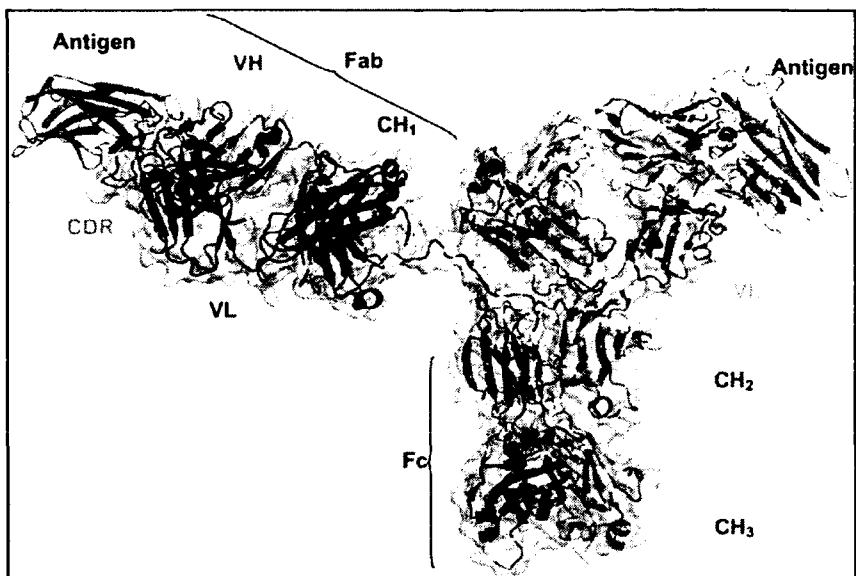
Figure 2.1 Structure of an antibody [71].

An antibody usually has a Y shape. The arms of the Y shape have their unique functions. The upper two arms consist of binding sites for antigens. This region is termed the "fragment, antigen binding (Fab) region" [29]. The base of the Y-shape contains the function group, carboxyl group COOH, and is used for further binding. This region is termed the "fragment crystallizable(Fc) region" [29].

As a type of antibody, IgG is specified to detect Protein A. This technology is widely used in biological research. In this work, Porcine IgG is purchased from Sigma-Aldrich, Co.

Protein A is usually derived from the cell wall of staphylococcus aureus bacteria. It has a large molecular weight of 40-60 kDa. The structure of Protein A is shown in Figure 2.2.
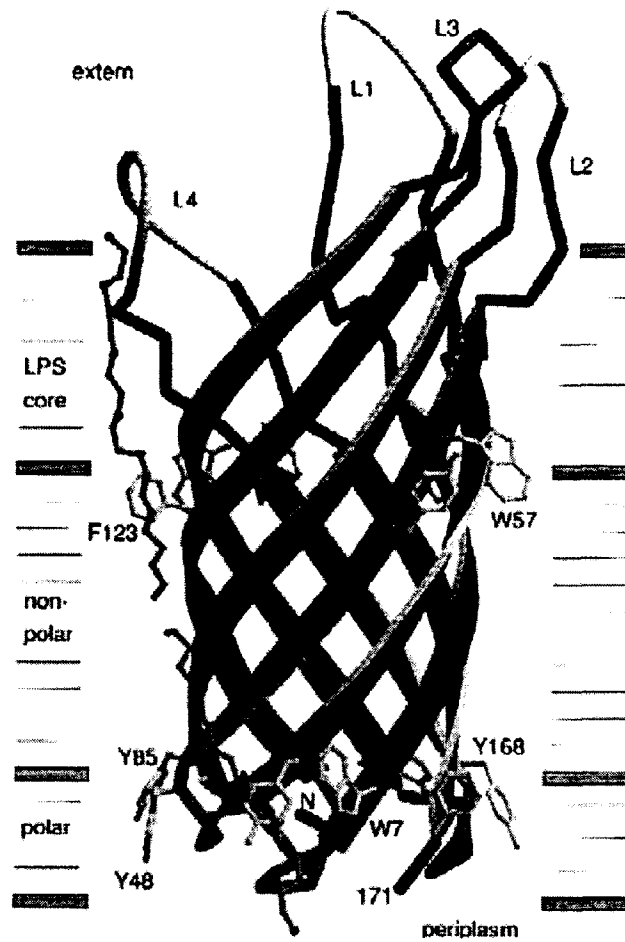
Figure 2.2 Structure of a protein molecule [72].

Due to its capability of binding with IgG, Protein A has been widely in biomedical research. Its structure consists of five homologous Ig binding sites, each of which could bind with different IgGs with different affinities. However, Protein A loses its function when it is denatured.

In this work, Protein A was purchased from Pierce Biotechnology, Inc. Usually, Protein A is first immobilized onto a substrate. The immobilized Protein A is used to purify IgG from a mixture sample such as serum or ascites fluid [73].

2.1.2   <u>Bovine Serum Albumin and</u>
        <u>Anti-Bovine Serum Albumin</u>

Bovine serum albumin (BSA) is a serum albumin protein prepared from cows. There is a lot of serum albumin in the human body and other mammals, making it essential for body fluids. However, it is also harmful if there is too much serum albumin in the body.

BSA has a molecular weight of 66.5 kDa. It has a high affinity and specificity for the anti-BSA antibody. BSA has been widely used inthe pharmacological and toxicological field [74]. In this work, BSA was obtained from Sigma-Aldrich, Co. It was diluted with PBS (pH=7.5) solution at several different concentrations of 50, 100, 500, 5,000 pg/mL. The analyte was anti-BSA IgG. In this work, anti-BSA Rabbit IgG and anti-Rabbit Goat IgG were also purchased from Sigma-Aldrich, Co. They were prepared by conjugating the IgG fraction of anti-bovine serum albumin (BSA) to cyanogen bromide-activated agarose.

Secondary anti-BSA Rabbit IgG labeled with FITC was used to confirm the binding between BSA and primary anti-BSA Rabbit IgG and verify the weak affinity of primary anti-BSA Rabbit IgG to gold surface. In this work, secondary anti-BSA Rabbit IgG labeled with FITC was purchased from Sigma-Aldrich, Co.

2.1.3   <u>Phosphate Buffered Saline</u>
        <u>and Sea Block</u>

Phosphate buffered saline (PBS) was used to prepare the Protein A, IgG, and BSA solutions. In this work, PBS was purchased from Sigma-Aldrich, Co. PBS was prepared by mixing sodium and potassium chloride with small quantities of Na_2HPO_4 and KH_2PO_4 in distilled or deionized water. It had the pH value of 7.5 at 25 °C.

Sea Block was purchased from Pierce Biotechnology, Inc. It is a protein based blocking buffer prepared from steelhead salmon serum in PBS. It is widely used as a blocking agent in immunohistochemistry and biological detection using mammalian samples.

2.1.4   SU8 and Poly Dimethylsiloxane

SU8 is a photosensitive epoxy-based polymer. SU8 is becoming widely used in the fields of micromechanics and microfluidics mainly by soft lithography [75, 76]. The structure of a SU8 molecule is shown in Figure 2.3.
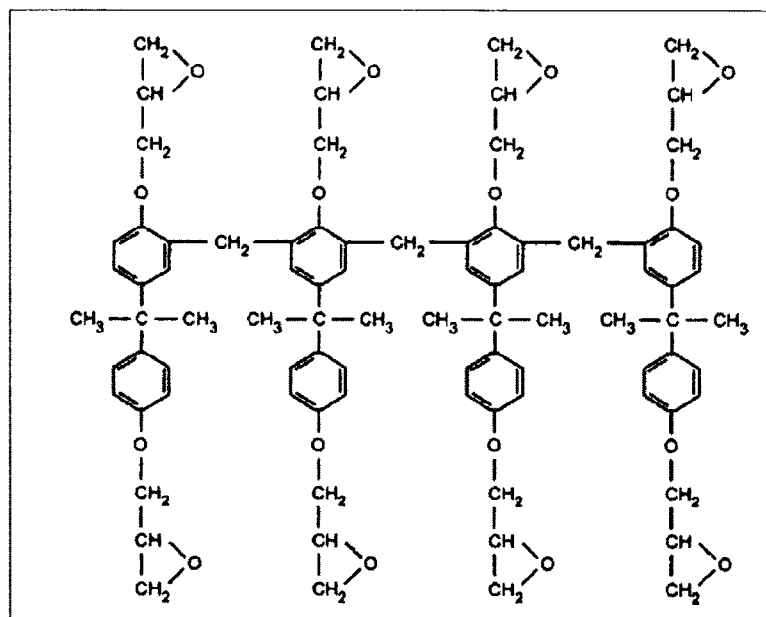
Figure 2.3 Structure of a SU8 molecule [77].

A structure of a SU8 molecule consists of eight epoxy groups. SU8 is a negative photo resist. Upon exposure to UV light, the SU8 molecules cross link, making the mold solidified. Usually, SU8 can be spun up to a thickness of 0.1 μm to form high aspect ratio structures [78]. In this work, SU8 2050 is purchased from MicroChem, Corp. and was used for fabricating the mold for the bio interaction chamber on a silicon wafer.

Poly (dimethylsiloxane) (PDMS) was well known as a silicon-based organic polymer. It has such biocompatibility as nonirritating to skin, no adverse effect on mice or rabbit. It is highly hydrophobic, with contact angles from $90°$ to $120°$. Its melting point is above $40°$. It has been widely used to make the replica from SU8 mold to construct microfluidic devices [79]. The structure of PDMS is shown in Figure 2.4.
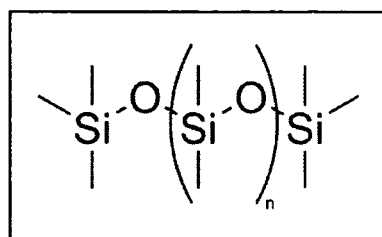
Figure 2.4 Structure of PDMS [80].

PDMS has such advantages as cost effective, easy to fabricate and optically transparent. These features make PDMS suitable for fabricating optically integrated devices using micro molding [79, 81]. PDMS is also inert to many chemicals and non-toxic and non-flammable. These features make PDMS suitable for biomedical testing [82].

In this work, PDMS (MicroChem, Corp.) was used to bond with the substrate to form the sensing chamber and micro fluidic channels. The surface of PDMS was hydrophobic after being cured. The surface of PDMS was treated with oxygen and bonded with the substrate.

2.1.5   Rhodamine 6G

Rhodamine 6G (R6G) is a chemical compound and its structure is shown in Figure 2.5.
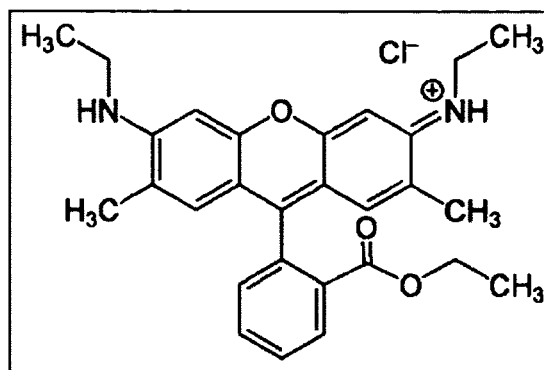
Figure 2.5 Structure of Rhodamine 6G [83].

R6G is a tracer dye and also a laser dye. As a tracer dye, its fluorescent efficiency is amongst the highest, and it is highly stable [84]. It is easy and inexpensive to detect with fluorometers. Therefore, R6G has been extensively used in environmental monitoring, food analysis, and biological research [85].

As a laser dye (also called gain medium), it has the characterization of low cost, higher photochemical stability, and lower lasing threshold [86]. Noble metals such as gold, silver can cause multiphoton induced emission on roughened surfaces. R6G can significantly enhance themultiphoton induced emission [87].

In this work, R6G (Lightning Powder Company, Inc.) was used to evaluate the optical signal enhancement capability of the Au-coated nanopore layers by measuring its Raman signals. A 250 µM R6G solution was prepared by mixing 0.12 mg R6G powder with 1 mL DI water. Substrates was immersed in R6G aqueous solution and incubated. Then, Raman spectroscopy measurements were performed on these substrates.

2.1.6   Free Prostate Specific Antigen

Mouse anti-human PSA monoclonal antibody (detector mAb) (catalog # T40081B,

clone # CHYH2), ELISA kits for human f-PSA (catalog # 10050) were obtained from

Anogen-YES Biotech Laboratories, Ltd. (Mississauga, Canada). The 10 ng/mL free-PSA

standard solution was used for the preparation of free-PSA solutions with lower

concentrations using sample dilutant provided in the ELISA kit. The 10 ng/mL free-PSA

standard solution was prepared in a protein matrix solution according to the WHO

standard by the vendor. The concentrations of diluted free-PSA included 0, 5, 10, 50, 100,

500, 5000 pg/mL for the experiments. Absolute ethanol was obtained from Thermo

Fisher Scientific, Inc., USA. Dionized (DI) water is obtained from a DI water purification

system (Millipore, France).

2.2   Equipment

The experimental setup is shown in Figure 2.6. It includes a white-light source,

optical probe, optical fibers, stage, syringe pumps, spectrometer, and data analysis system.
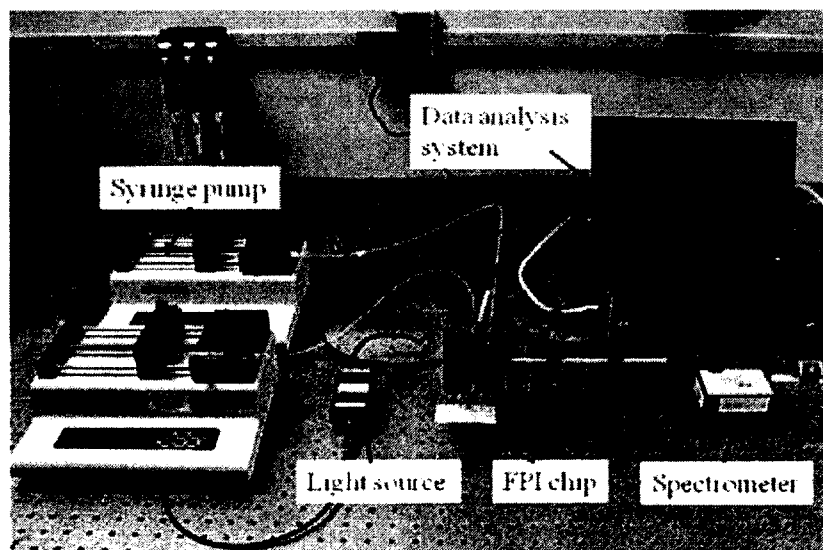
Figure 2.6 Experimental setup for optical testing.

2.2.1 White-Light Source

The white-light source shown in Figure 2.7 was purchased from Ocean Optics, Inc. It is a tungsten halogen white-light source (LS-1), with a spectrum range from 360 nm to 2,500 nm. The LS-1 is featured with an SMA 905 connector, which can be easily coupled to optical fibers with SMA 905 connectors.

Figure 2.7 Photograph of a white-light source.

2.2.2 Spectrometer

The spectrometer was also purchased from Ocean Optics, Inc. The spectrometer (USB4000) has a resolution of 0.21 nm and the smallest integration time is 3 ms. The USB4000 is featured with an SMA 905 connector, which can be easily coupled to optical fibers with SMA 905 connectors, as shown in Figure 2.8.
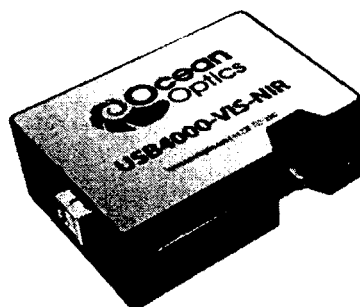
Figure 2.8 Photograph of a spectrometer.

2.2.3 Optical Fiber and Probe

The optical fiber probe was customized from Ocean Optics, Inc. The optical fiber probe consists of a tight bundle of seven optical fibers in a stainless steel ferrule, as shown in Figure 2.9. The center fiber was used to collect the reflected light while the outer six fibers deliver the illumination light to the FPI chemo/biosensor. This optical fiber probe delivers white-light from a tungsten halogen source perpendicularly to a biochemical sensor. This probe also receives the reflected signals from the sensor, which was eventually coupled to a USB4000 spectrometer.
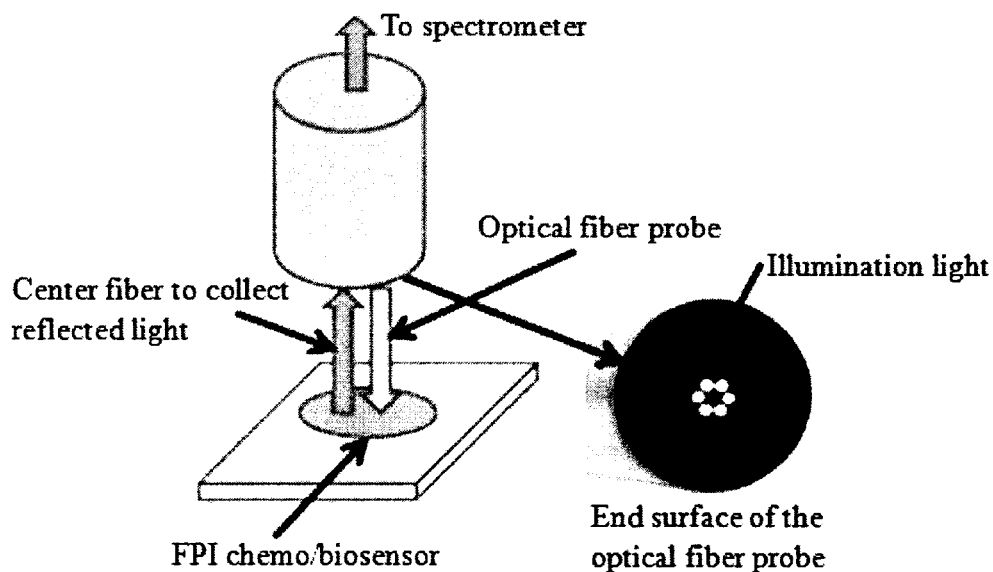
Figure 2.9 Schematic of an optical testing setup.

2.2.4 Opto-Mechanical Components

According to the manufacturers, opto-mechanical components should be set up on top of an optical platform (Newport, Inc.) to hold the optical fiber probe. The optical fiber probe was fixed on a probe holder kinematic mount with three-screw adjustment (Edmund Optics, Inc.), as shown in Figure 2.10. The holder can adjust the angle of the probe. Other posts, holders and adaptors were purchased from Thorlabs, Inc.
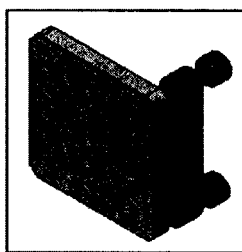
Figure 2.10 Probe holder.

2.2.5 Raman Microscope

SENTERRA Raman Microscope (Bruker Optics, Inc.) was used to measure the Raman signals of R6G on glass, AAO, and Au-coated AAO substrates, respectively. The system is shown is Figure 2.11.
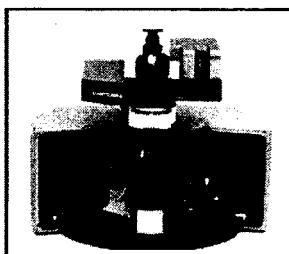
Figure 2.11 Photograph of a Raman microscope.

In this Raman spectroscopy, a 785 nm laser was used for exciting Raman signals. This instrument incorporates a patented automatic fluorescence rejection (AFR) method

for eliminating fluorescence from samples, thereby increasing the ratio of signal-to-noise of Raman signals.

2.2.6 Sputter Coater

The sputtering machine Cressington 108 Sputter Coater used to sputter gold was made by Cressington Scientific Instruments, Inc.

The sputter coater can work in two modes, either manual or automatic. In the automatic mode, there are two options. The first option is multi-thickness mode (MTM). In this option, the coating process stops when assigned thickness is reached. The second option is timer-control mode. In this option, the coating process stops when assigned time was reached.

CHAPTER 3

DESIGN, FABRICATION, AND EVALUATION

3.1   Design

A schematic of two microfluidic nanostructured FPI devices on a single chip is illustrated in Figure 3.1. Each device consists of a PDMS plate, an Au-coated nanopore layer, and a glass plate. The Au-coated nanopore layer is anchored inside the FPI cavity. The average size of nanopores before Au coating is ~50 nm in diameter and the gap size of the FPI cavity is 50 μm. Note that for some nanostructured μFPI devices, the nanopore layer is not Au coated for comparison in some experiments.
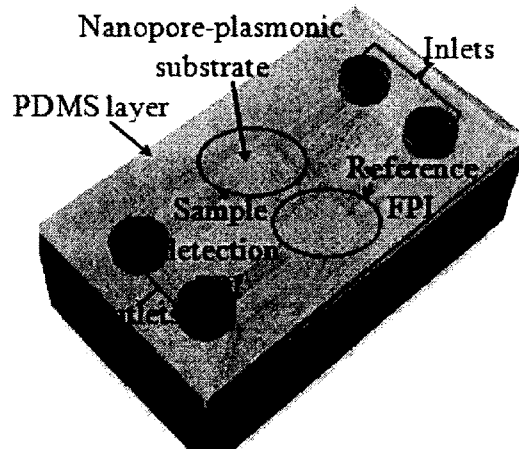
Figure 3.1 Schematic of two nanostructured FPIs.

3.1.1 Microfluidic Chip

For conventional immunoassays, probe molecules and target molecules are pipetted to the wells of the immunoassays and incubated for reaction without stirring. One of the disadvantages of conventional immunoassays is the relative large amount of samples, which are expensive. This problem can be solved by using the micro or nanotechnology to reduce the volume of the samples to nano- or picoliters. The other disadvantage of conventional immunoassays is the relatively long incubation time, which occurs because of its dependence on the diffusion time. The large molecules used in the experiments such as IgGs (150 kDa), diffuse very slowly in the wells of the immunoassays. The relation between the diffusion time and the diffusion distance inside a well follows the Einstein-Smoluchowski equation, as shown in Eq. (3-1)

$$d = (2Dt)^{1/2}, \tag{3-1}$$

where d is the diffusion distance, t is the diffusion time, and D is the diffusion coefficient.

For IgGs with a diffusion coefficient D of $4 \times 10^{-7}\,\mathrm{cm^2/s}$, it takes about three and one-half hours to diffuse 1 mm distance, which is the order of distance in a well of an immunoassay. However, the much smaller chamber dimensions, such as 50 μm, in this design, could reduce the diffusion distance, and therefore, the diffusion time to less than 1 min. Thanks to the micro- and nanotechnology, microfluidic chips based on the polymer PDMS was used to shrink the dimensions of the sensing chamber and speed up the detection and analysis process.

3.1.2 Nanostructured Fabry-Perot Interferometer

The embedded nanopores inside the FPI cavity were used for increasing the sensing surface area, namely increasing the number of binding sites for the biomolecules. The cross section view of the nanostructured FPI biosensor is shown in Figure 3.2.
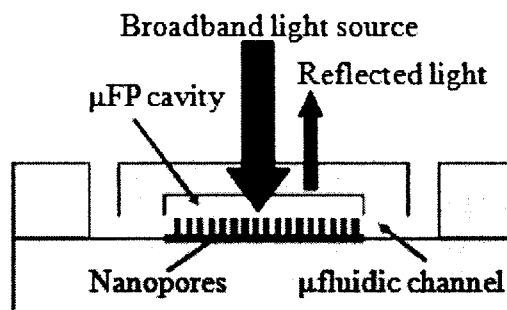
Figure 3.2 Cross section view of a nanostructured FPI.

The sensing surface area includes the top, bottom surfaces of the nanopore layer, and sidewalls of the nanopores. The thickness of the nanopore layer is 3 μm. Therefore, the penetration depth of the light can be 3 μm. In other words, the optical sensitive range had been extended to 3 μm from the top surface of the nanopore layer. The Au thin film that is coated on the nanopore layer and sidewalls of the nanopores was used for enhancing the optical signal intensity.

3.2   Fabrication

The fabrication of a nanostructured Fabry-Perot interferometer includes the PDMS based microfluidic chip, the porous anodic aluminum oxide, the gold thin film coating, and the assembly of the chip.

3.2.1   <u>Fabrication of PDMS Based</u>
        <u>Microfluidic Chip</u>

The device was fabricated using an inexpensive and rapid soft lithography process

[88]. First, SU8 was spin coated on a standard 100 mm diameter silicon wafer. An optical

micrograph of the SU8 mold of one single μFPI device showing the integrated channel

for sample delivery to the FP cavity is given in Figure 3.3. The diameter of the FPI plate

was 250 μm. The thickness of the SU8 mold of the device was 50 μm.

Figure 3.3 Optical micrograph of a SU8 mold.

A 50 μm high SU8 mold was formed on the silicon wafer as shown in Figure 3.4

(A). PDMS was casted on the mold, followed by a 1.5 hr curing at a temperature of 65 °C,

as shown in Figure 3.4 (B). Then, the PDMS layer was peeled off from the mold. After

this step, the input and output channels were made in the PDMS layer using a 1.5 mm

diameter hole puncher, as shown in Figure 3.4 (C).

SU 8 mold

(A)

PDMS replica

(B)

PDMS layer

(C)
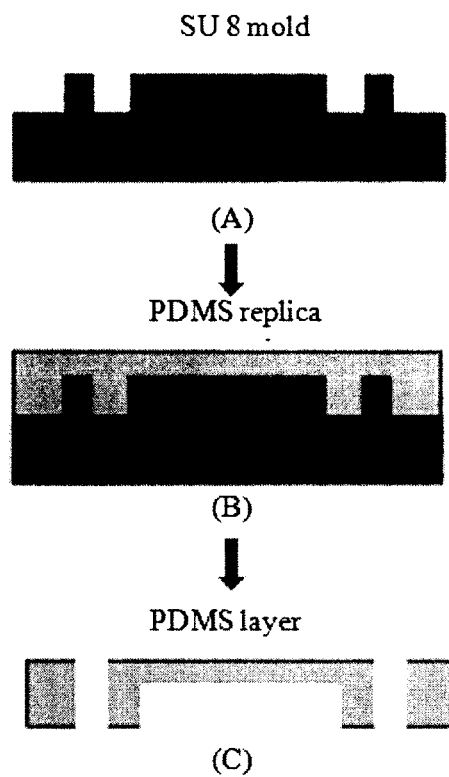
Figure 3.4 Fabrication process of a PDMS microfluidic chip.

An optical image of a 2 × 2 PDMS FPI device is shown in Figure 3.5. The cavity length is 50 μm. The diameter of each FPI chamber is 250 μm.

Figure 3.5 Optical micrograph of 2 × 2 PDMS-FPIs.

3.2.2 Fabrication of Porous Anodic Aluminum Oxide

The device consisted of a PDMS layer and an Au-coated nanopore layer. The nanopore layer was a porous anodic aluminum oxide (PAAO) layer. The PAAO layer was fabricated from an aluminum substrate using a standard two-step anodization process [89]. The fabrication process of the nanostructures began with a polished aluminum plate, as shown in Figure 3.6 (A). Then, the nanopores were formed using two-step anodization process, as shown in Figure 3.6 (B). A 5 Å Cr adhesion thin film was sputter coated on AAO, as shown in Figure 3.6 (C). Finally, a 50 Å Au thin film was sputter coated, as shown in Figure 3.6 (D).

Aluminum

(A)

Porous AAO

(B)

Sputter Cr

(C)

Sputter Au

(D)
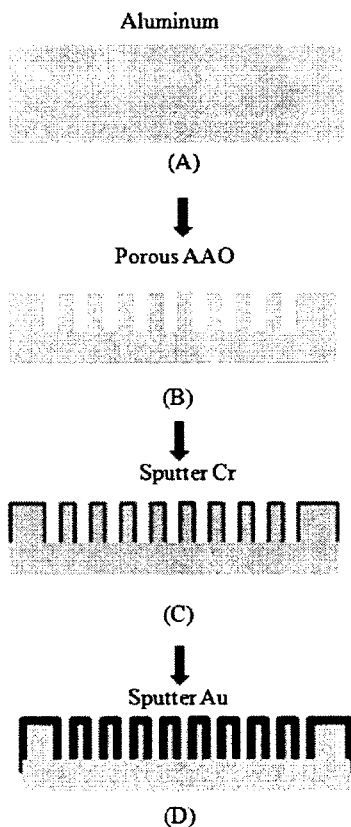
Figure 3.6 Fabrication process of nanostructures.

Major steps for the anodic aluminum oxide (AAO) fabrication included polishing of the aluminum substrate, two-step anodization process, and release of the AAO barrier layer.

The aluminum plate was purchased from Alfa Aesar, Inc. During the initial experiment, the aluminum plate was first cut into small square pieces while trying to better perform the fabrication process. The SEM image of the close-up of a bare nanopore structure layer is shown in Figure 3.7.
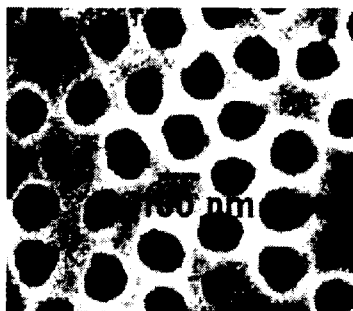
Figure 3.7 Close-up SEM image of a bare nanopore layer.

It has arrayed pores with size of about 50 nm in diameter. The size of the nanostructure as well as the space among them, can be tuned by changing the operational parameters during the fabrication process.

It should be noted that depending on specific applications, the size of nanostructure as well as the space among them, can be readily tuned during the fabrication process from several ten nanometers to several hundred nanometers (e. g., 100-200 nm) in diameter [89]. Hence, the nanopores are big enough and can provide sufficient volumes and surface areas for biomolecular interaction inside them.

3.2.3   Gold Thin Film Coating

After fabricating the nanostructures, in order to enhance the optical transducing signal, a thin layer of gold was coated on top of the nanopore layer using sputter coating. First, a layer of 5 Å thick Cr was deposited onto PAAO as an adhesive layer. Then, a layer of Au thin film was deposited. Au thicknesses were from 5 Å to 100 Å in these experiments. For comparison, close-up SEM images of a bare AAO layer and an Au-coated AAO layer are given in Figure 3.8. As shown, the Au thin film on AAO layer clearly consists of Au nanoparticles with size in the range of 10-20 nm. The gold nanoparticles in this structure play the major role in enhancing the intensity of the optical signal due to the localized surface Plasmon resonance effect [90, 91].

Figure 3.8 SEM images of bare AAO and Au-coated AAO.

In order to have a three dimensional view of the nanostructure, an AFM image of a topside view of the nanopore layer and a 3D AFM image of the nanopore layer are given in Figure 3.9, showing the nanopores uniformly distributed. On the left, there is a top side view of the nanopore layer. On the right, there is a 3D AFM image of the nanopore layer.

Figure 3.9 AFM images of nanopores.

3.2.4 Assembly of the Biosensing Platform

Finally, the PDMS layer and the Au coated nanopore layer were bonded together to complete the device fabrication after an oxygen plasma treatment. The input and output wells were made in the PDMS layer for the delivery of samples to the nanopore-FPI or Au-nanopore-FPI devices.

The fabrication process flow and the assembly of the nanostructured FPI biosensor began with the SU8 mold by the soft lithography process, as shown in Figure 3.10 (A). Then, PDMS microfluidic channel was formed using the SU8 mold, as shown in Figure 3.10 (B). The input and output channels were punched with a 1.5 mm diameter hole puncher, as shown in Figure 3.10 (C). The nanopore layer began with a polished aluminum plate using a two-step anodization process, as shown in Figure 3.10 (D). A 5Å Cr adhesion thin film was sputter coated on AAO, as shown in Figure 3.10 (E). Then, a 50 Å Au thin film was sputter coated on top, as shown in Figure 3.10 (F). Finally, the PDMS microfluidic chip was bonded with the Au coated AAO to form the biosensor chip, as shown in Figure 3.10 (G).
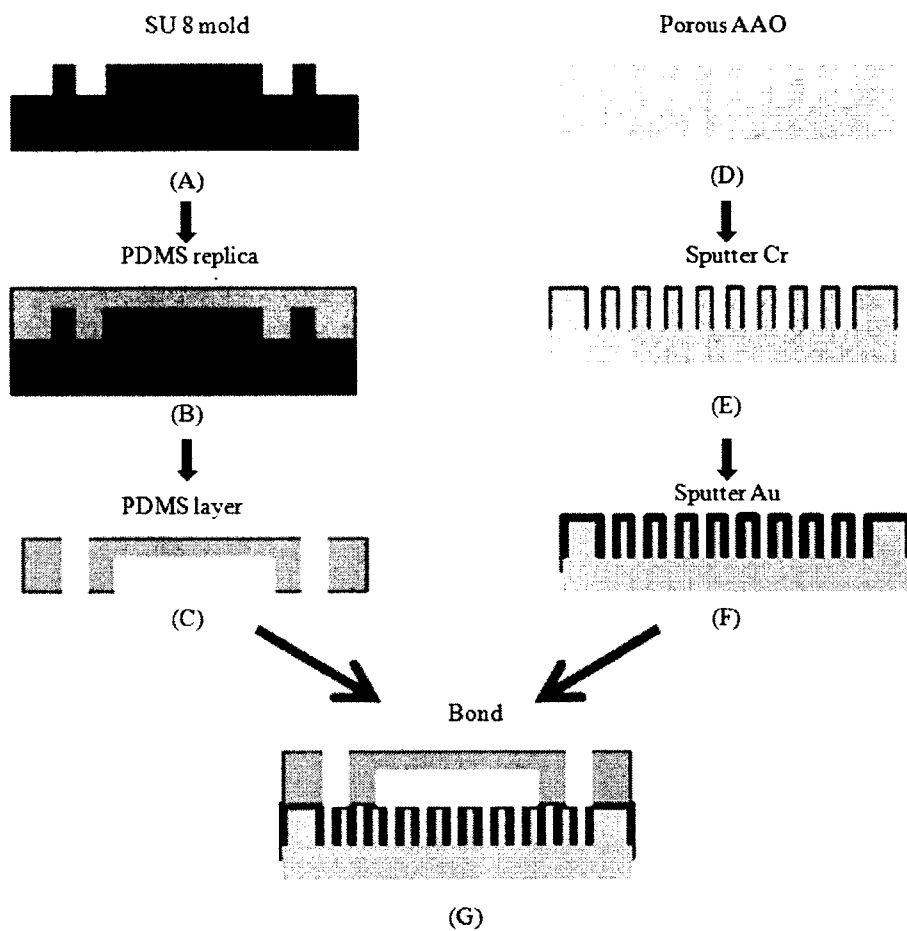
Figure 3.10 Assembly process flow of the biosensing platform.

The optical micrograph of the assembled polymer Au-nanopre-FPI is shown in Figure 3.11, compared with a nickel.
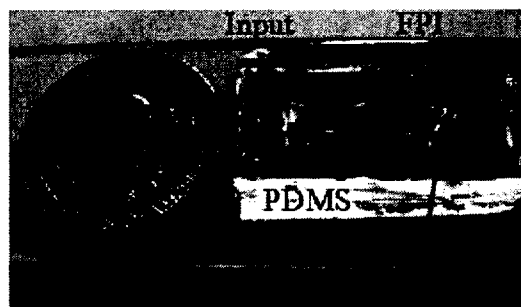
Figure 3.11 Photograph of a PDMS-based nanostructured FPI.

The arrayed devices can be readily and rapidly batch-fabricated, offering a cost effective and disposable biosensing technical platform with high throughput.

3.3   Evaluation

The prototype Au-nanopore-FPI sensor has also been evaluated with some chemicals such as IPA, ethanol, and water. As expected, clear shifts of the interference fringes has been observed in Figure 3.12 due to their different refractive indices. The coated Au thickness was 20 Å.
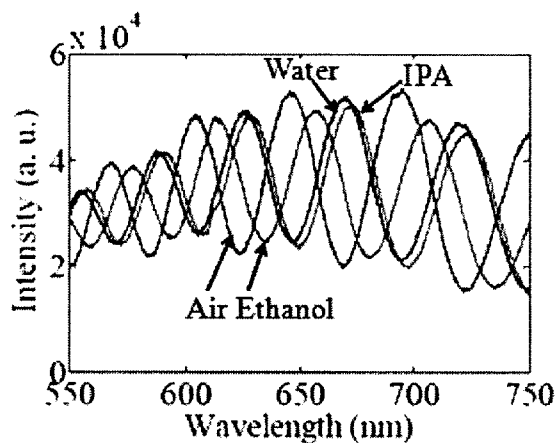
Figure 3.12 Evaluation of a prototype device.

In Table 3.1, the average fringe peak shifts relative to air inside the FPI cavity are summarized. The average shift was obtained by averaging the shift of the fringe peaks between the 400 nm to 1100 nm spectrum window. Given the resolution of the USB4000 Spectrometer is 0.02 nm, the measurement error for the fringe peak shift is ± 0.01 nm. It should be noted that if the nanopores are blocked due to thicker Au coating, the interference fringes will disappear as observed in these experiments. This result confirmed that the nanopores play an important role in the formation of interference fringes.

Table 3.1 Fringe peak shift and EOT change.

Material	Average interference peak shift relative to air (400 nm-1100 nm)	Calculated EOT change relative to air (nm)
Water	24.94 ± 0.01 nm	517.8 nm
IPA	37.09 ± 0.01 nm	776.7 nm
Methanol	22.67 ± 0.01 nm	258.9 nm

In order to simplify the analysis of transducing signals, Fourier Transform (FT) was performed on measured optical signals. For an FPI device, the wavelength (λ) of the peak maxima in the interference spectrum is given by: $m\lambda=2nL$, where m is the spectral fringe order, n is the effective refractive index of nanostructure layer and its contents in the cavity, L is the geometric thickness of nanostructure layer and FPI cavity gap. $2nL$ represents the effective optical thickness (EOT) and can be obtained from FT of measured spectrum in Figure 3.12 [92]. As a result, only a single peak was presented for each case, as shown in Figure 3.13, in which the x-axis was EOT [92]. Changes of EOT for different chemicals relative to air inside the FPI cavity are summarized in Table 3.1.
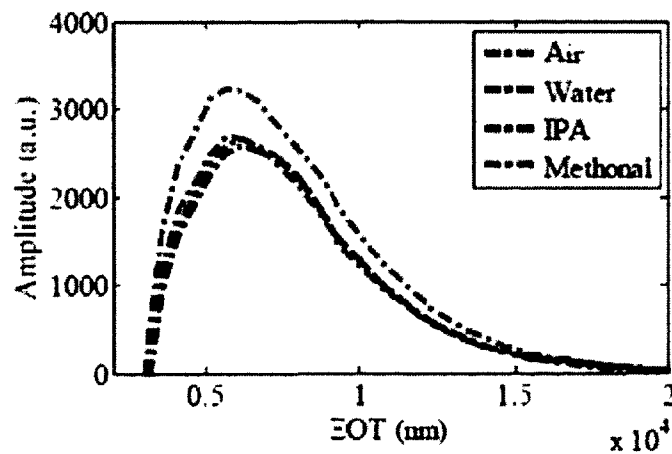
Figure 3.13 The FT plot for evaluation.

3.4   Functionalization

The antibody IgG is usually a Y-shaped protein with large molecular weight. The foreign targets such as bacteria and viruses are called antigens. Due to the existence of antibodies, large foreign molecules such as antigens could be detected by the immune system, neutralized, and cleaned out of the human body. Antibodies are specified to their corresponding antigens with high affinity. In the field of clinical research, this feature makes antibodies a good choice of biological agents for treating a variety of diseases [71]. The schematic of an antibody structure is shown in Figure 3.14. The arms of the Y-shape have their own unique functions. The upper two arms consist of binding sites for antigens. This region is termed the "fragment, antigen binding (F_{ab}) region" [29]. The base of the Y-shape contains the function group, carboxyl group COOH, and is used for further binding with the antigen. This region is termed the "fragment crystallizable (F_c) region" [29].
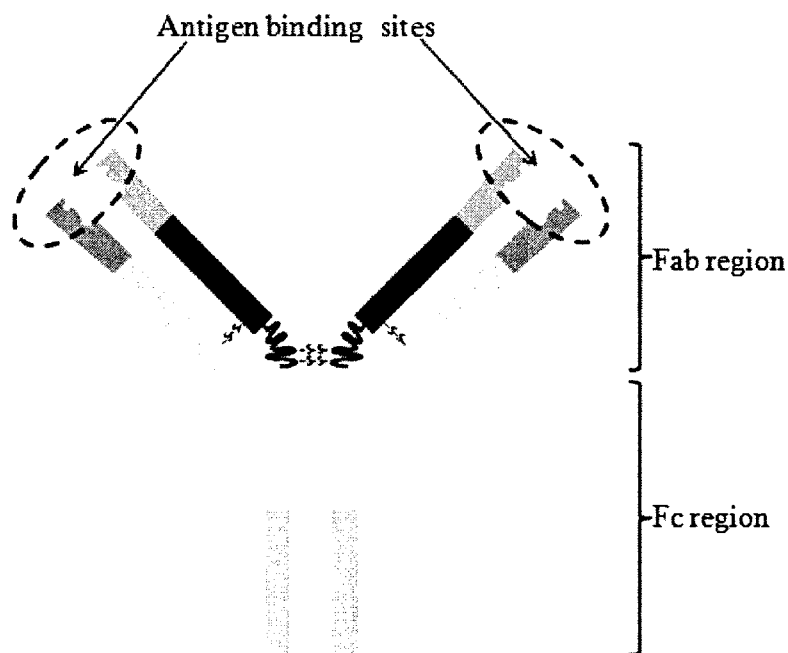
Figure 3.14Schematic of an antibody structure [29].

In this work, the part of the antibody used to detect the antigen was the F_c domain of IgG. It contained the base as the binding site, which was used to bind with Protein A. It should be noted that different from the conventional immobilization of IgG first and binding with Protein A sequence, Protein A was immobilized due to its high affinity with gold surface and used to orient IgG.

As a type of antibody, IgG is specified to detect the antigen Protein A. Protein A is usually derived from the cell wall of staphylococcus aureus bacteria. It has a large molecular weight of 40-60 kDa. Due to its capability of binding with IgG, Protein A has been widely used in biomedical research. Its structure consists of five homologous IgG binding sites, each of which could bind with different IgGs with different affinities. However, Protein A loses its function when it is denatured.

Protein A was first immobilized onto a substrate. Then, the immobilized Protein A was used to purify IgG from a mixture sample such as serum or ascites fluid [73]. At a pH value of 7.4, Protein A is negatively charged [29]. It can be immobilized on gold surface by physical forces. Initially, PBS was pumped into the FPI cavity to rinse the device. Thereafter, the Protein A solution is applied into the device and allowed to stay for 30 min at room temperature, as shown in Figure 3.15 (A). The Protein A had sufficient time to bind to the Au-coated surface of the nanopore structures and served as capture proteins. The unbound Protein A was then washed away using PBS solution. The washing routine consisted of at least three cycles of pumping PBS through the device and each cycle lasting for 3mins. The measurement of the optical transducing signals was taken at each cycle for three times and checked for measurement repeatability. In order to block the sites on the nanopore layer unoccupied by Protein A, the solution was pumped

next into the device. The solution was allowed to stay for 15 mins at room temperatureas shown in Figure 3.15 (B). Then, the solution was pumped out and the wash and measurement routine was performed. Thereafter, the IgG solution was applied onto the device and allowed to settle and bind with Protein A for 15 to 30 mins at room temperature as shown in Figure 3.15 (C). The measurement was taken after washing the excess unbound IgG using PBS solution.

Protein A

(A)

Sea Block

(B)

IgG

(C)
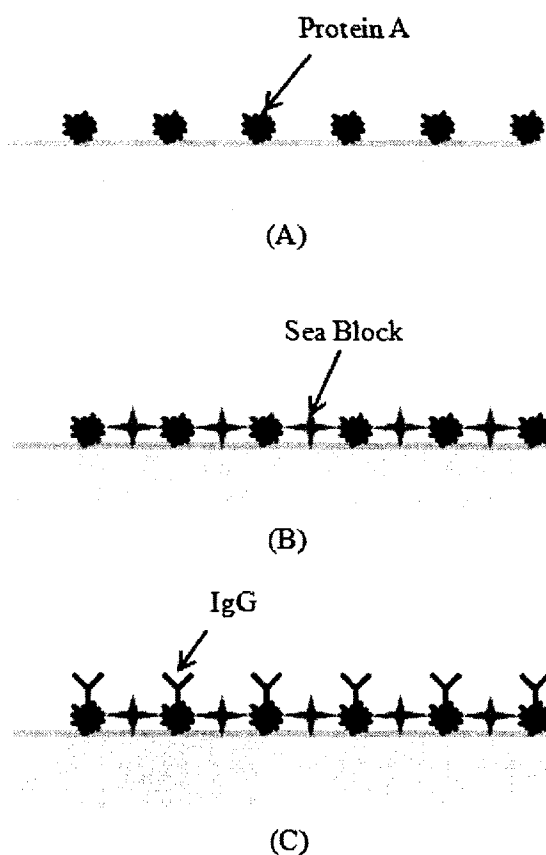
Figure 3.15 Functionalization process.

In this surface modification process, the capture probe Protein A was used to bind with the antibody IgG and used to orient IgG.

3.5 Summary

In summary, a polymer-based nanostructured-FPI device has been developed and fabricated, its performance evaluated, and the device functionalized for subsequent immunosensing. The nanostructured-FPI device offered some unique properties such asincreased sensing area, extended penetration depth of the excitation light, and the tremendous amplification of the optical transducing signals. It is anticipated that this new type of nanostructured-FPI device can offer an ultrasensitive (e. g., femtomole) technical platform forlabel-free biosensing. The simple, cost-effective, and disposable nature of this type ofsensor is attractive for rapid point-of-care and field biodetection applications as well. Fourier Transform of the measured spectrum can simplify the data analysis since only one single peak presents in its corresponding plot for different samples whose x-axis coordinate is the EOT of the nanostructure layer and the gap size of the FPI cavity. Finally, the device has been functionalized for subsequent immunosensing.

CHAPTER 4

ENHANCEMENT OF OPTICAL
TRANSDUCING SIGNALS

4.1   Raman Signal Enhancement

To analyze the signal enhancement mechanism for the Au-coated nanostructured

FPI, two methods can be used. One is to measure the near field optical intensity

distribution directly using a near field scanning optical microscope [93]. The other is the

indirect measurement which can be achieved by measuring the Raman signal

enhancement of molecules on the nanostructure in the optical far field [94].

The Raman signals of R6G in Figure 4.1 of the same concentration of 250 µM

have been obtained on Au-coated AAO, AAO, and glass substrates, respectively.
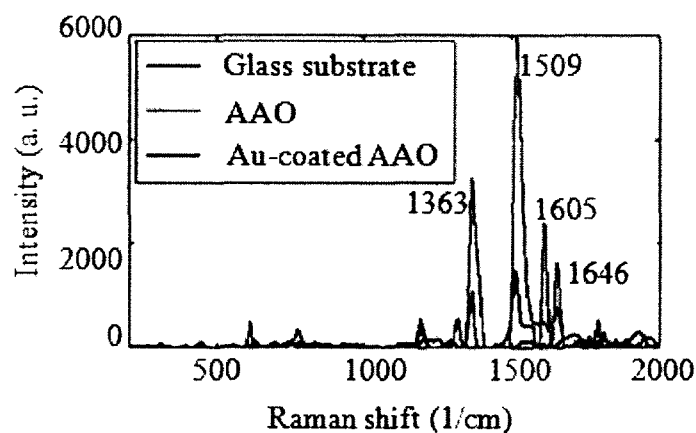
Figure 4.1 Measured Raman spectra of R6G.

A SENTERRA Raman microscope was used to measure the Raman signals of R6G on glass, AAO, and Au-coated AAO substrates, respectively. In this Raman spectroscopy, a 785 nm laser was used for exciting Raman signals. This instrument incorporates a patented AFR method for eliminating fluorescence from samples, thereby increasing the ratio of signal-to-noise of Raman signals. R6G was used to evaluate the optical signal enhancement capability of the Au-coated nanopore layers by measuring their Raman signals. A 0.12 mg of R6G powder was mixed with 1 mL DI water to get a 250 μM R6G solution. A glass substrate, an AAO substrate, and an Au-coated AAO substrate were immersed in a R6G aqueous solution for 30 mins, separately. Thereafter, all of the three substrates are rinsed with DI water rigorously. Then, they were dried in a vacuum dryer for 1 hr at room temperature before Raman spectroscopy measurements were performed on these substrates.

As a result, the Raman signal of R6G was amplified significantly on the Au-coated AAO. The result indicated that the optical signal enhancement was enabled by the nanoscale roughness of the Au thin film coated on the nanopore structures due to the L-SPR [70].

4.2   Interferometer Signal
Enhancement

In order to examine the optical transducing signals of a gold thin film coated nanostructured FPI, a comparative experimental study ona conventional μFPI and nanostructured FPIs (with and without Au thin film coating) was carried out. The testing setup is shown in Figure 4.2.
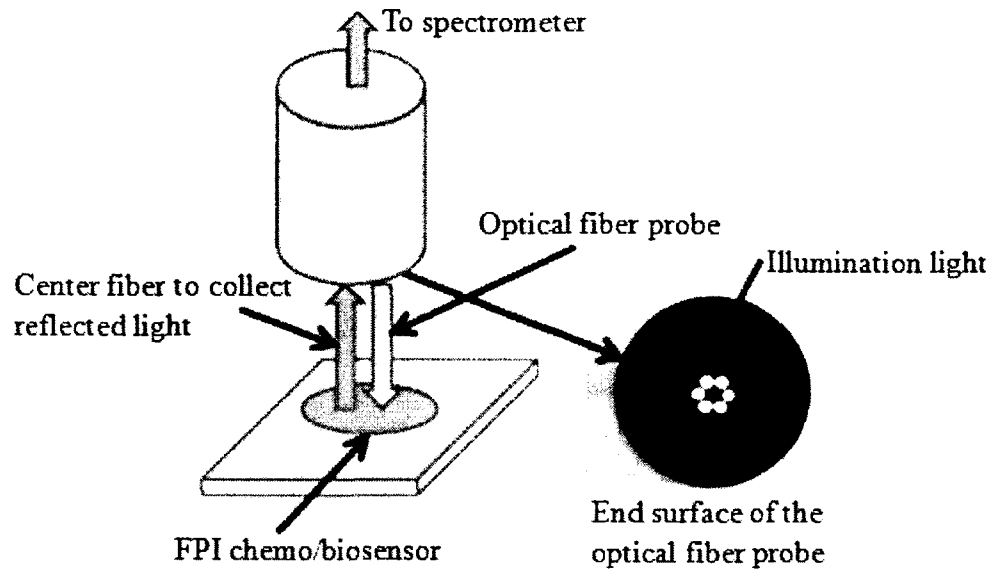
Figure 4.2 Testing setup of optical signal enhancement.

An isometric sketch of a nanostructured FPI is shown in Figure 4.3. All the FPIs had the same FPI cavity size of 50 µm.
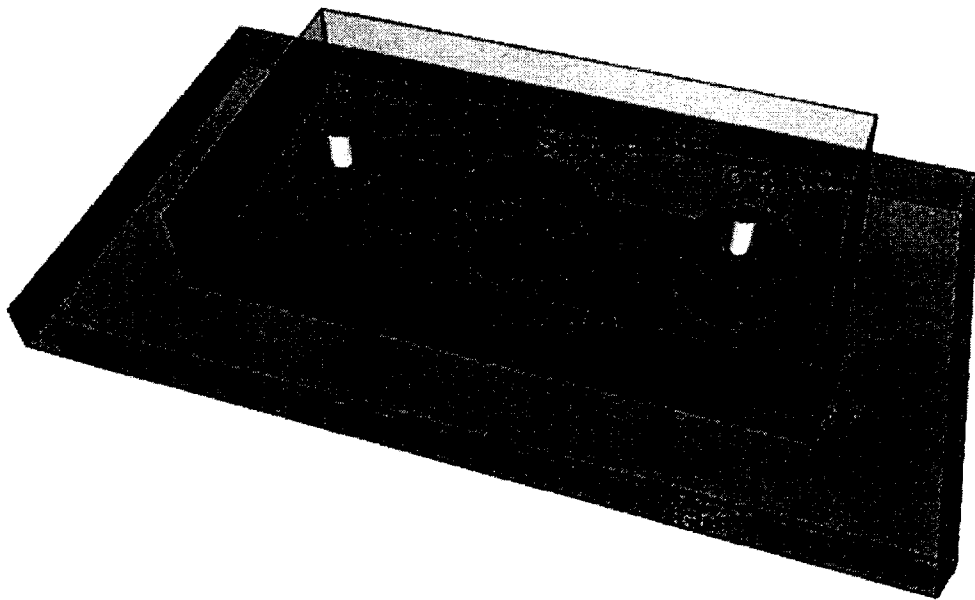
Figure 4.3 Isometric sketch of a nanostructured FPI.

For the nanostructured FPIs, one nanostructured FPI had an Au-coated nanopore layer and the other had the same nanopore layer but without Au coating inside its FPI cavity. Prior to any addition of fluid, optical transducing signals of each device were compared with air inside FPI cavities. Optical transducing signals were from three devices with a conventional μFPI, a nanostructured FPI without gold coating, and a nanostructured FPI with a 50 Å gold coated thin film layer. The optical transducing signal was amplified significantly for the gold coated device as shown in Figure 4.4.
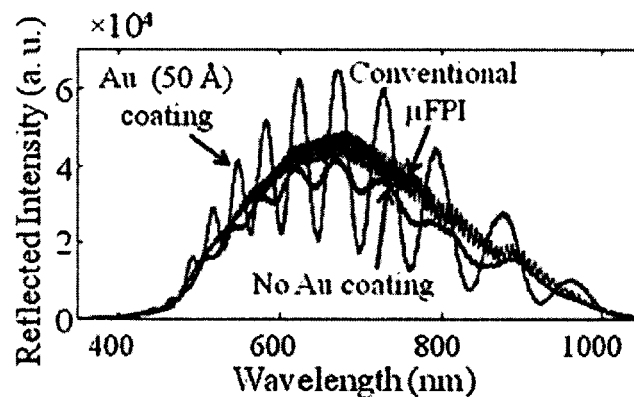
Figure 4.4 Enhancement of optical transducing signals.

Systematic experiments found that an Au-coated nanostructured FPI with a nanopore size of 50 nm had around twenty times improvement in FSR, around two times improvement in finesse, and around four times improvement in contrast of optical transducing signals over a traditional μFPI even without any device performance optimization. The FSR of a conventional μFPI was approximately 3 nm, which was determined by the 50 μm of the FPI cavity gap. In contrast, the FSR (around 60 nm) of a nanostructured FPI was essentially determined by the geometrical dimensions (nanopore size, pitch, and depth) of the nanopore layer. The comparison of these optical parameters of different types of devices is summarized in Table 4.1.

Table 4.1 Comparison of optical parameters.

	FSR	Finesse	Output contrast
uFPI	Low	Low	Low
FPI w/o Au	20 ×	Low	Low
FPI w/Au	20 ×	2 ×	4 ×

4.3   Finite Element Analysis
of Signal Enhancement

The simulation for the signal enhancement by arrayed nanopores was carried out using COMSOL. The module used was the electromagnetic wave module. The preset study was in frequency domain. The equation solved was the Maxwell equation. The parameters are shown in Table 4.2.

Table 4.2 Global parameters.

Name	Expression	Description
na	1	Refractive index, air
nb	1.77	Refractive index, alumina
Lam0	600 nm	Wavelength
f0	c_const/lam0	Frequency

The simulation result for Au-coated nanopores is shown in Figure 4.5. Due to the nanoscale roughness of the Au thin film, the transducing signal was greatly amplified.
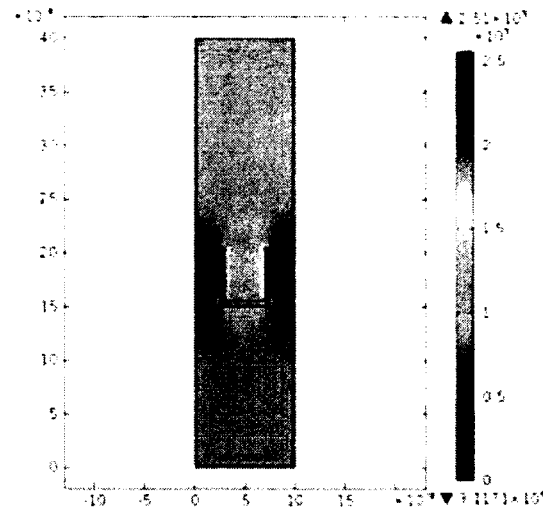
Figure 4.5 Illumination profile surrounding Au-coated nanopores.

The simulation result for bare nanopores is shown in Figure 4.6. Compared with the illumination profile for Au-coated nanopores, there is negligible enhancement.
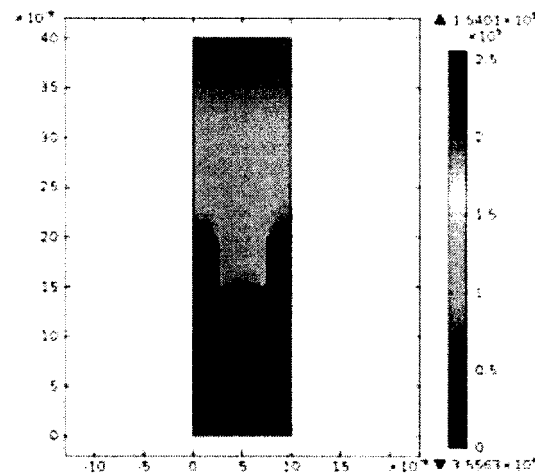
Figure 4.6 Illumination profile surrounding bare nanopores.

The electric field norm means the length of the electric field vector in COMSOL [95]. For a 50 nm diameter and a 100 nm distance from pore to pore at the wavelength of 600 nm and the gold thickness of 5 nm, the ratio of the electric field norm of Au-coated nanopores to that of bare nanopores is approximately twenty times. The intensity of

reflected light is the square of the electric field norm. Therefore, the enhancement of the light intensity is approximately 400 times.

In order to get a white-light spectrum, simulation for different wavelengths was performed. The wavelength ranged from 500nm to 800nm, with a step size of 100nm. Enhancements for different wavelengths are summarized in Table 4.3.

Table 4.3 Enhancements for different wavelengths.

Wavelength (nm)	Enhancement
500	385.7532
600	377.7853
700	369.8852
800	363.0092

The relationship between intensity enhancementsand wavelengths has been plotted in Figure 4.7. In the white-light range, the 5 nm thick gold coated arrayed nanopores with a diameter of 50 nm and a distance of 100 nm from pore to pore had approximately 400 times enhancement for the light intensity. There was a slightly more enhancement for a shorter wavelength.
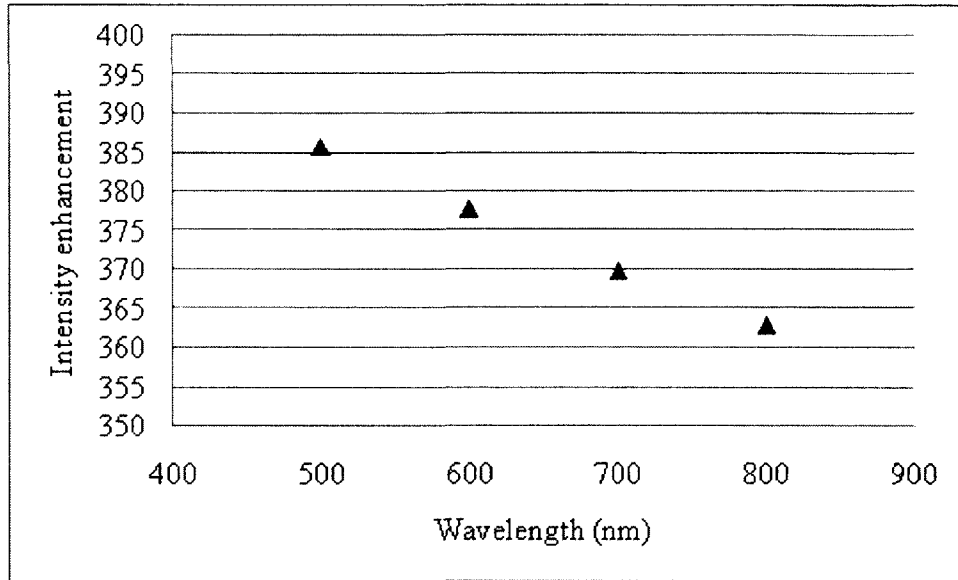
Figure 4.7 Relationship between enhancements and wavelengths.

Enhancements for different thicknesses are summarized in Table 4.4. The relationship between enhancements and thicknesses has been plotted in Figure 4.8. Among 2 nm, 5 nm, and 8 nm thicknesses, the 8 nm thick Au-coated structure has the greatest enhancement.

Table 4.4 Enhancements for different gold thicknesses.

Thickness (nm)	Enhancement
2	267.5057
5	377.7853
8	489.7280
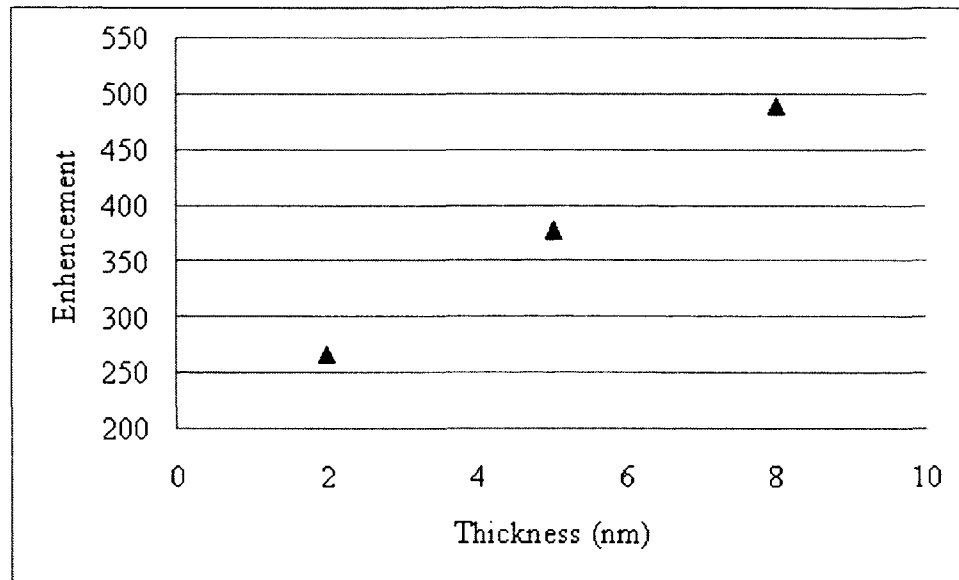
Figure 4.8 Relationship between enhancements and thicknesses.

In order to study the effect of different nanopore structures, numerical analysis for different pore diameters and pitch sizes was carried out. Pitch is the distance from pore to pore. Pitch ratio is defined as the ratio of the pitch to the diameter of the nanopore. Enhancements for 50 nm and 100 nm diameter nanopores are shown in Table 4.5 and Table 4.6, respectively.

Table 4.5 Enhancements for 50 nm diameter nanopores.

Pitch ratio	Enhancement
2	378
3	671
4	1226

Table 4.6 Enhancements for 100 nm diameter naonpores.

Pitch ratio	Enhancement
2	214
3	574
4	1473

The relationship between enhancements and pitch ratios is plotted in Figure 4.9. Among diameters of 50 nm and 100 nm, and pitch ratios of 2, 3, and 4, the nanostructure with a diameter of 100 nm and a pitch ratio of 4 had the greatest enhancement.
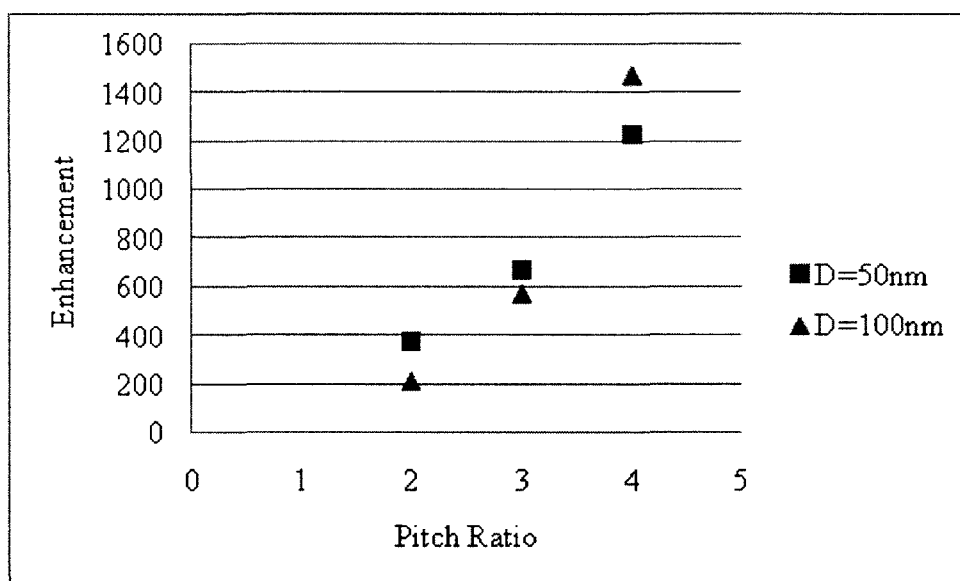
Figure 4.9 Relationship between enhancements and pitch ratios.

4.4   Summary

In summary, experiments for enhancements of optical transducing signals were carried out by both the Raman spectroscopy and the Fabry-Perot interferometer. Enhancements of Raman signals indirectly confirmed enhancements of optical

transducing signals. The FEA of the intensity distribution for arrayed nanopores was also performed. The calculated results confirmed the great enhancement of the optical transducing signals using the Au-coated nanopores.

CHAPTER 5

USEING FLUORESCENT IMAGING TO
CONFIRM FRINGE SHIFTS

5.1   Overview

The flow chart and the photograph of the experimental setup are shown in Figure

5.1 and Figure 2.6, respectively.
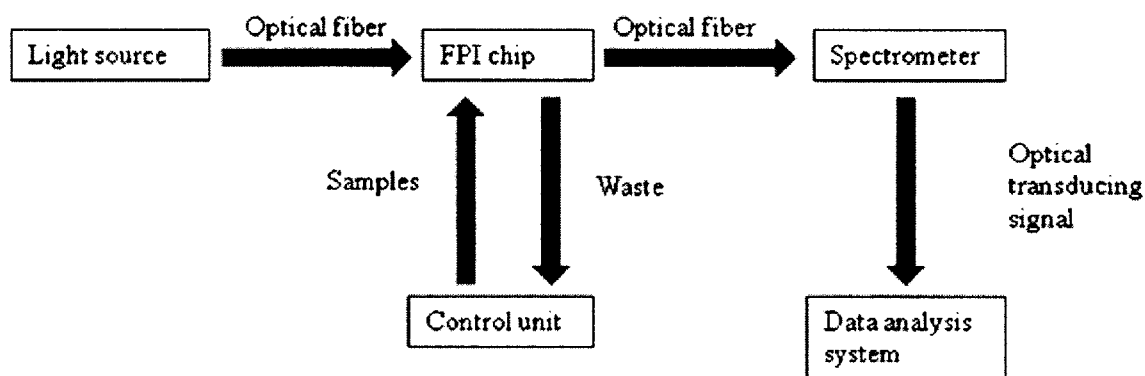
Figure 5.1 Flow chart of the experimental setup.

Before starting actual experiments, the small affinity of IgG for gold surface

compared with the affinity of BSA for gold surface needed to be confirmed.

Confirmation step began with incubating a 0.5 mg/mL anti-BSA rabbit IgG (diluted in

PBS) on gold surface for 45 mins. Then, the gold surface was rinsed with PBS to wash

away unbonded anti-BSA rabbit IgG. The second incubation was done with 0.5 mg/mL

of anti-rabbit goat IgG labeled with FITC fluorescent dye (diluted in PBS) on the

63

previous surface for 45 mins. Finally, the gold surface was rinsed with PBS to wash away unbonded anti-rabbit goat IgG. The measured interference fringe result showed that there was no interference fringes shift before and after the incubation of anti-BSA rabbit IgG on the gold surface. This whole process was also monitored under a fluorescence microscope, and the observation did not show any kind of fluorescent signal. The absence of shift in the interference fringes and the absence of any kind of fluorescence signal confirmed that IgG exhibited a relatively small affinity for gold surface at pH=7.5.The experimental process for BSA detection is described in Figure 5.2.
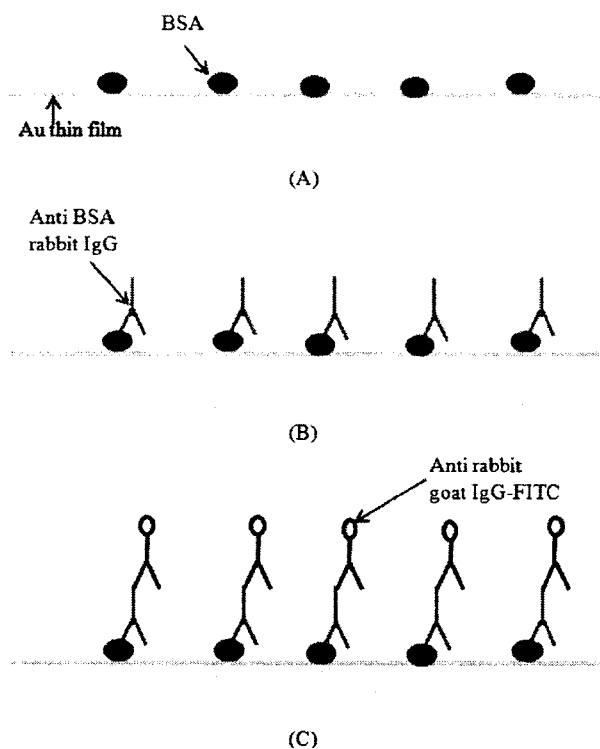
Figure 5.2 Experimental process for BSA-IgG detection

The actual experiment began with washing the surface of the nanostructured Fabry-Perot interferometer based biosensor, as shown in Figure 5.2 (A). A 0.5 mg/mLBSA (diluted in PBS) solution was pumped into the device to ensure the

nanostructure sensing surface was fully occupied by BSA, as shown in Figure 5.2 (B). The incubation time was 45 mins. This was followed by three cycles of rigorous PBS rinsing. Then, a primary antibody, anti-BSA rabbit IgG, was pumped into the device and allowed to incubate for 45 mins, as shown in Figure 5.2 (C), followed by PBS rinsing. Thereafter, a secondary antibody, anti-rabbit goat IgG labeled with FITC fluorescent dye, was pumped into the device to ensure the binding of secondary antibody to the primary antibody, as shown in Figure 5.2 (D). The incubation time was 45 mins and followed by three cycles of rigorous PBS rinsing.

5.2   Indirect Confirmation of Biosensing Signals

While shifts of interference fringes from a nanostructured Fabry-Perot interferometer based biosensor were optically monitored in real time, their corresponding fluorescent images were obtained at the same time to indirectly confirm the biosensing signals.

5.2.1   Shift of Fringes for Biodetection

The experimental process was the same as described above. This whole process was monitored by a spectrometer in real time. The interference fringes for each step of the biointeractions are shown in Figure 5.3.
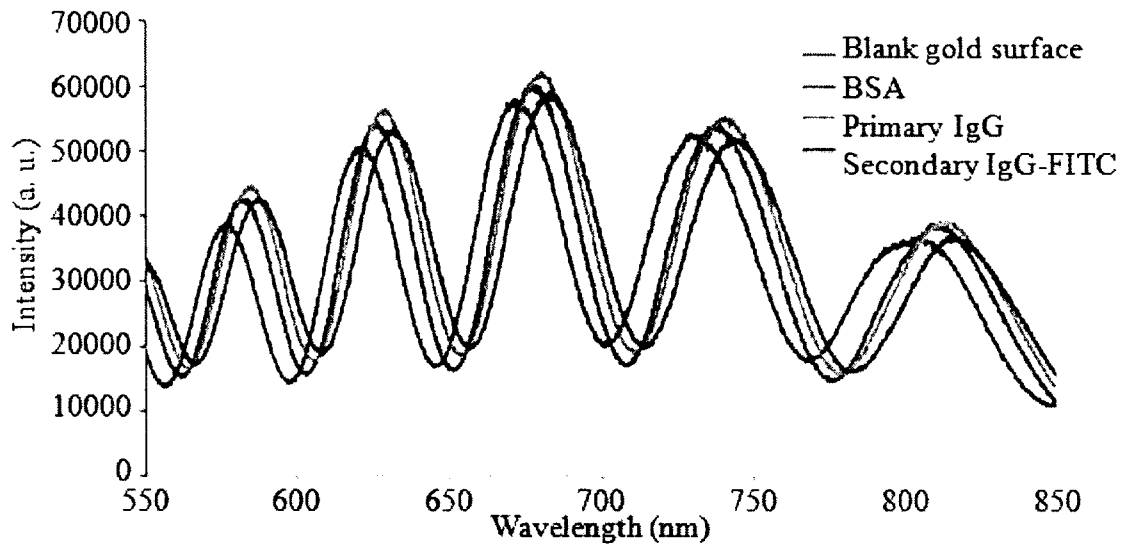
Figure 5.3 Optical transdusing signals for BSA-IgG detection.

The clear shift between the primary IgG anti-BSA rabbit IgG and BSA indicated there was binding between the primary IgG and BSA. The clear shift between the secondary IgG anti-rabbit goat IgG labeled with FITC and the primary IgG indicated there was binding between the primary IgG and the secondary IgG as well.

5.2.2   Fluorescent Imaging
         for Biodetection

In order to indirectly confirm shifts of interference fringes from the experiment above, their corresponding fluorescent images were simultaneously obtained.

The whole experimental process was monitored under a fluorescence microscope at the same time, and fluorescent images are shown in Figure 5.4.

(A)

(B)

(C)
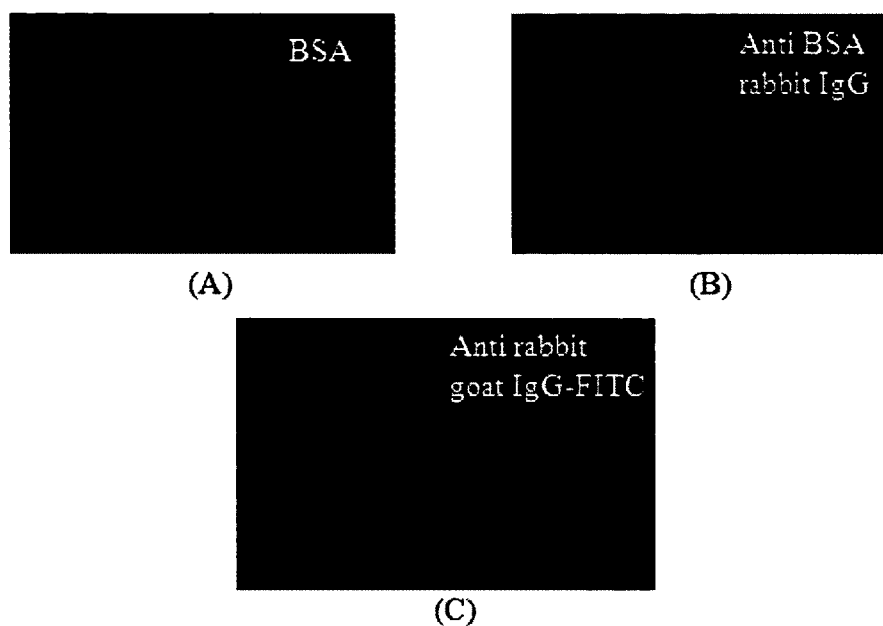
Figure 5.4 Fluorescent images for BSA-IgG detection.

Figure 5.4 (A) is a fluorescence image taken after applying BSA to the sensing surface of the biosensor. Figure 5.4 (B) is a fluorescence image taken after binding the primary IgG anti-BSA rabbit IgG to BSA treated sensing surface. Figure 5.4 (C) is a fluorescence image taken after binding the secondary IgG anti-rabbit goat IgG labeled with FITC and the primary IgG. From the images, one may see that no fluorescent signals were detected before the secondary IgG treatment, and clear fluorescent signals were detected after the secondary IgG treatment. This result indicated there is immobilization of BSA to the sensing surface and binding between the primary antibody and BSA.

The fluorescent images indirectly confirmed shifts of interference fringes from the experiment work for BSA and anti-BSA IgG interaction.

5.3 Summary

In this chapter, the control experiment was first carried out to confirm the small affinity of IgG to the gold coated sensing surface. Then, using fluorescent images, shifts of interference fringes for IgG and BSA interaction were indirectly confirmed.

CHAPTER 6

A PROTEIN BASED BIOSENSOR
FOR IGG DETECTION

6.1   Overview

The schematic of a nanostructured FPI sensor was given in Figure 3.1. The biosensor was fabricated from PDMS and glass plate with its FPI cavity formed between them. Different from a conventional FPI, inside its cavity there was a layer of nanopore structures, serving as the biosensing area. This nanopore layer increased a great deal of the sensing area, thus enhancing the sensitivity of the senor greatly. In addition, this layer of nanopore was coated with Au thin film, typically ranging in thickness of several tens of angstroms. Due to the nanoscale roughness of the Au thin film, the transducing signal (e. g., reflected light) was amplified tremendously. Its operation procedure was reported previously by T. Zhang et al. [61]. The ease-of-fabrication of arrayed FPI sensors on a single chip facilitated its applications for highly multiplexed biosensing.

A brief explanation of the operation principle was given as follows. As a refractive-index sensitive optical sensor, both immobilization of probes on the nanopore surfaces and their binding with different Immunoglobulin G (IgG) caused changes of effective refractive index and changes of EOT of the nanopore-structure layer inside the cavity. As a result, the interference fringes shifted, which could be monitored optically in real-time. More specifically, after Protein A adhered on the sidewall of nanopores, as

shown in Figure 6.1, the reflected optical signal from the sensor changed, resulting in the shift of the interference fringes of the reflected signal. The binding between Protein A and Porcine IgG are shown in Figure 6.1.
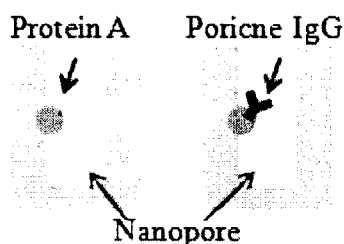
Figure 6.1 Closeup of a nanopore region.

The surface of nanostructures inside the FPI was first functionalized with probes (Protein A). The binding between Protein A and Porcine IgG antibody without tagging was monitored by the optical transducing signals: interference fringe shift ($\Delta\lambda$) upon the change of the effective refractive index.

6.2   Biodetection Procedures

The assay reagents used in the experiments included Protein A, buffer solution phosphate buffered saline (PBS), and Porcine IgG. Specifically, Protein A was prepared in PBS solution at a concentration of 500 µg/mL, which can be diluted accordingly for different concentrations. The blocking buffer, used to minimize the non-specific binding was mixed with PBS solution with a ratio of 1:4. Similarly, the Porcine IgG anti-sera were diluted with PBS with final concentrations of 500 µg/mL, 500 ng/mL, 50 ng/mL, and 5 ng/mL, respectively. The experimental procedures were as follows. First, the PBS solution was applied into the FPI cavity to rinse the sensor. Thereafter, the Protein A solution (500 µg/ml) was flowed into the device and allowed to stay inside the FPI cavity

for 30 mins at room temperature. Sufficient Protein A molecules were allowed to bind to the Au-coated surface of the nanopore structures and served as capture proteins. The unbound Protein A was then washed away using PBS solution. The washing routine is done at least three cycles of 3 mins each. The measurement was taken at each interval and checked for measurement repeatability. After this step, the solution was flowed into the device to block the unmodified or unbound sites in the FPI cavity. The solution was allowed to stay inside FPI cavity for 15 mins at room temperature. After the specified time, the solution was pumped out and the wash routine performed again to take some measurements. Similarly, the Porcine IgG solution made with PBS solution was applied into the device and allowed to settle for 15 to 30 mins in the FPI cavity at room temperature. The measurements were taken at regular intervals after washing the excess unbound Porcine IgG using PBS solution.

6.3   Results and Discussions

6.3.1   Protein and IgG Biodetection

The binding between Protein A and Porcine IgG in the nanostructured FPI sensor was monitored. Measured optical signals from the biosensor are shown in Figure 6.2.
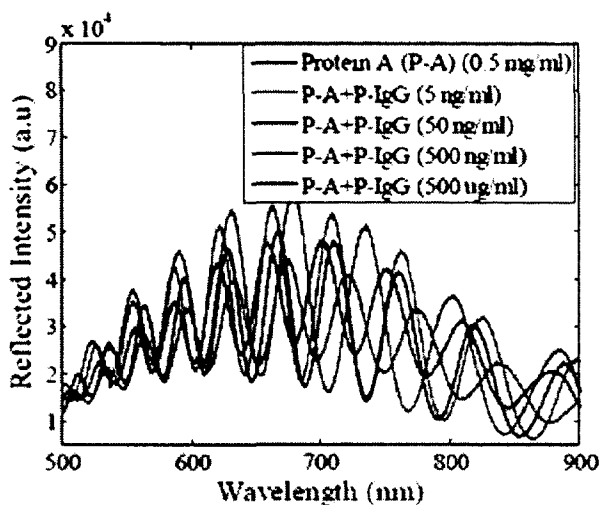
Figure 6.2 Measured signals for Protein A-IgG binding.

A clear shift in interference fringes was observed during the analyte binding process. For the same concentration of Protein A, the shifts for varied concentrations of Porcine IgG were different, which means that there was a change of the effective refractive index for each case. In other words, the higher the concentration of Porcine IgG, the more binding between Protein A and Porcine IgG, hence a higher effective refractive index and larger shift of interference fringes, as shown in Table 6.1.

Table 6.1 Summary of binding measurements.

Material (IgG represents Porcine-IgG, P-A represents Protein A)	Average peak shift relative to P-A (nm)	EOT change relative to P-A (nm)
P-A (0.5 mg/mL)	-----	------
P-A + IgG (0.5 mg/mL)	22.9	2072
P-A + IgG (500 ng/mL)	-5.6	1554
P-A + IgG (50 ng/mL)	-13.2	1036
P-A + IgG (5 ng/mL)	-16.9	518

While the measurement of the shift of interference fringes is a valid way to analyze and quantify the bioassay process, it is inconvenient to count and average shifts of hundreds of fringe peaks. In contrast, FT on the measured interference fringe data can simplify this process [92]. It is well known that the wavelength (λ) of the peak maxima in the interference spectrum for FPI is given by

$$m\lambda=2nL, \qquad\qquad (6\text{-}1)$$

where m is the spectral fringe order, n is the effective refractive index of nanostructure layer and its contents, L is the geometric gap of the FPI and thickness of nanostructure layer. $2nL$ represents EOT and can be obtained from FT of measured spectrum in Figure 6.3. A MATLAB program was written and implemented to perform the FT on the measured data. As seen with FT on the measured spectrum in Figure 6.3, only a single peak, whose x-axis position was EOT of the FPI cavity gap and the nanostructure layer, was presented.
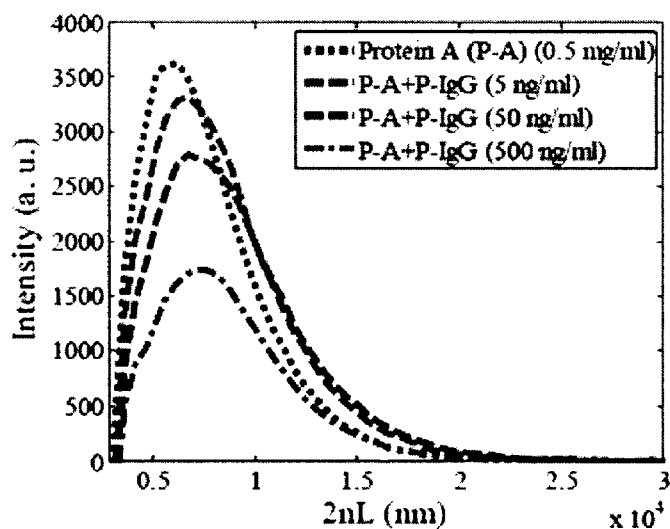
Figure 6.3 Fourier transform of reflectance spectrum.

The EOT with immobilized P-A (0.5 mg/mL) was 6214 nm. The EOT changed

after its binding with Porcine IgG (P-IgG) at varied concentrations as summarized in

Table 6.1. Again, for different concentration of P-IgG, the EOT was different. The higher

the concentration of P-IgG, the more binding between P-A and P-IgG occured, hence the

larger the EOT. The DOL of this sensor was evaluated by decreasing the concentration of

the P-IgG. Based on the measured data in Table 6.1, the EOT changed after its binding

with P-IgG at a concentration of 5 ng/mL up to 518 nm, which indicated the DOL of this

biosensor should be much lower than 5 ng/mL.

6.3.2   Detection of Limit

In order to test DOL downward, lower concentrations of Porcine IgG were tested.

Porcine IgG was diluted with PBS with final concentrations of 50 ng/mL, 5 ng/mL, and

10 pg/mL, respectively. The experimental procedures were the same as before.

The measured transducing signals from the biosensor are shown in Figure 6.4. As

can be seen, among different concentrations of IgG, the average shift in interference

fringes at a concentration of 10 pg/mL is the smallest.
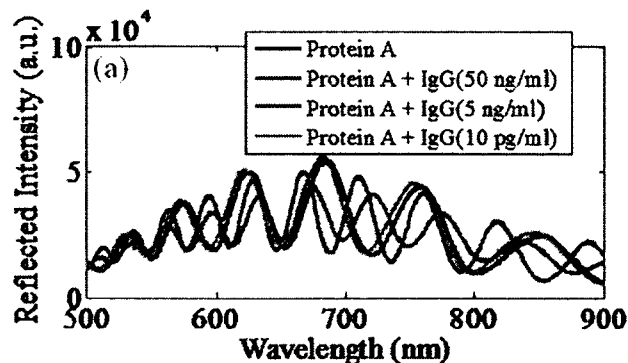
Figure 6.4 Measured signals for DOL test.

The FT on the measured spectra is shown in Figure 6.5. It shows the changes of EOT with different concentrations of Porcine IgG. Inset is a table summarizing the ΔEOT upon the binding between Protein A and Porcine IgG at different concentrations.

Material	Δ(EOT)
ProteinA (0.5 mg/ml)	---
ProteinA+IgG(50 ng/ml)	1036±2 nm
ProteinA +IgG(5 ng/ml)	518±2 nm
ProteinA +IgG(10 pg/ml)	256±2 nm
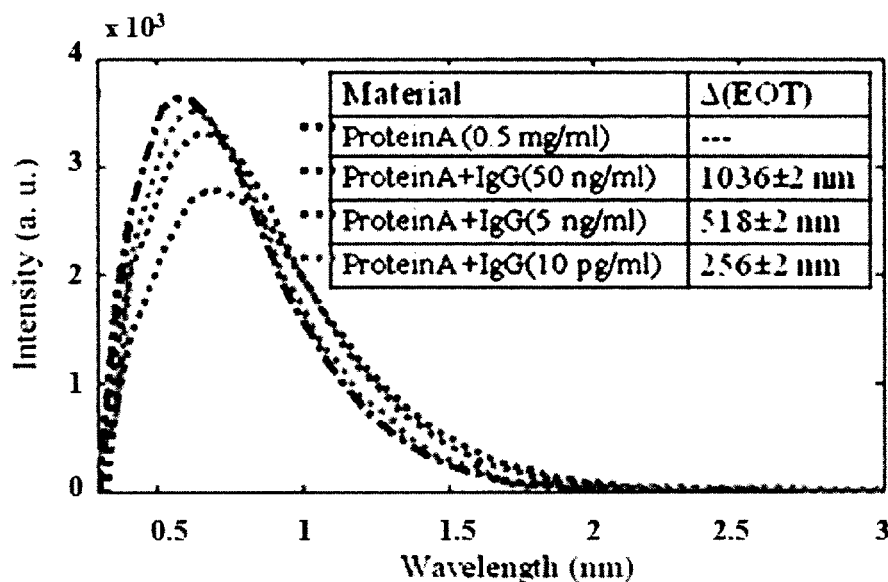
Figure 6.5 Fourier transform of signals for DOL test.

As expected, the ΔEOT decreased if the concentration of IgG decreased. The DOL of this technical platform was, therefore, the concentration of applied IgG where the ΔEOT approaches zero or undistinguished by the optical spectrometer. Experiments found that the ΔEOT after Protein A binding with IgGat a concentration of 10 pg/mL was still about 256 nm, which indicated that the DOL of this biosensor should be much lower than 10 pg/mL for IgG-Protein A binding.

6.3.3 Control Experiments

Control experiments were performed to check if Sea Block bonds with Protein A or IgG, to confirm that the biodetection is only specific to Protein A and IgG recognition.

The procedure for the control experiment to check if Sea Block bonds with

Protein A was carried out as follows. First, two cycles of undiluted solution were pumped

into two devices to ensure the nanostructure sensing surface was fully occupied. The

incubation time was 1 hr, followed by rigorous PBS rinsing. Then, Protein A was applied

and allowed to incubate for 45 mins followed by PBS rinsing. The measurement result is

shown in Figure 6.6. From the measurement result, interference fringes had negligible

shift, indicating Sea Block does not bind with Protein A.
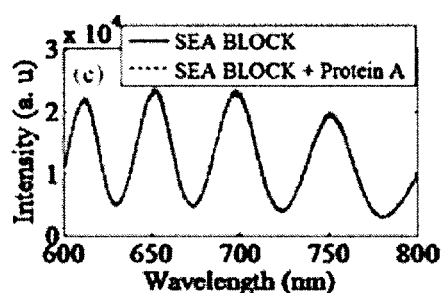
Figure 6.6 Control experiment for Protein A and Sea Block binding.

The procedure for the control experiment to check if Sea Block bonds with IgG

was carried out as follows. First, two cycles of undiluted solution were pumped into two

devices to ensure the nanostructure sensing surface was fully occupied. The incubation

timewas 1 hr and followed by rigorous PBS rinsing. Then, IgG was applied and allowed

to incubate for 45 mins followed by PBS rinsing. The measurement result is shown in

Figure 6.7.
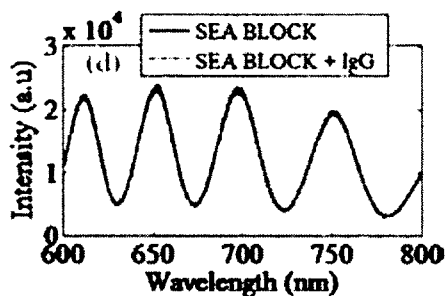
Figure 6.7 Control experiment for IgG and Sea Block binding.

From the measurement result, interference fringes had negligible shift, indicating Sea Block does not bind with IgG. The IgG used in this experiment was rabbit IgG.

6.4 Summary

In summary, a protein-protein (Protein A and Porcine IgG) binding assay has been used to demonstrate the operation and label-free biomolecular detection capability of the nanostructured FPI at room temperature. The Au-coated nanostructure layer inside the FPI cavity offered significantly enhanced optical interference signals due to the L-SPR effect and the increased sensing surface area. Immobilization of Protein A on the nanostructure layer and its binding with IgG inside the FPI cavity were monitored in real time, resulting in interference fringes shift. FT was performed on the measured interference spectra to simplify the analysis of the transducing signal. Experimental results indicated that DOL of the nanostructured FPI biosensor should be lower than 10 pg/mL, which is approximately 55 fM of IgG, for IgG-Protein A binding.

CHAPTER 7

ULTRASENSITIVE DETECTION
OF A CANCER BIOMARKER

7.1   Overview

The detection of cancers at their early stage is critical for survival of patients [97, 98]. In the field of genomics and proteomics, a variety of technologies have been developed for biomarker discovery and early detection such as various DNA microarrays [99], DNA sequence methods [100], enzyme-linked immunosorbent assay (ELISA) [101], two-dimensional polyarylamide gel electrophoresis (2D-PAGE) [102], mass spectrometry [103], proteomic pattern diagnostics [104], and protein/antibody microarrays [105]. However, most detection schemes suffer from a complicated fluorescent dye labeling process, bulk instrumentation and low sensitivity, and they are not applicable for trace detection of biomarkers at the early stage of tumor diseases. For instance, sandwich ELISA is the gold standard in the detection and quantification of protein/cancer biomarkers [38]. But sandwich assays are inconvenient for achieving large scale multiplexed measurements [39]. On the other hand, most fluorescent imaging based techniques are incapable of providing sufficient sensitivity to monitor biomarker affinity at concentrations of around 10 pM or lower without some forms of signal amplification [40]. The concentration of many clinically relevant biomarkers residing in biofluids (i. e., blood) is usually at picomolar concentrations or lower [39], about 5-7 orders of

magnitude lower than the most abundant plasma protein. Since there is no universal ultrasensitive enzymatic amplification method for proteins like polymerase chain reaction (PCR) for the detection of nucleic acid [39], a diagnostic tool with ultrasensitivity (picomolar, femtomolar concentration or lower) and high specificity is required.

To this end, micro- and nanotechnologies play a very important role in the enhancement of the sensitivity and DOL of the biosensing technologies. A variety of different detection technologies based on micro- and nanotechnologies have been developed in the past decades for the measurement of the tumor markers at a low concentration level, showing great promise for potential applications in point-of-care diagnostics and clinic settings. Among these technologies is the label-free optical detection technique. Label-free techniques are attractive for biosensing since no fluorescent dyes are needed to be attached to the biomolecules. As a result, the experimental cost can be reduced dramatically, and the possible perturbation of the properties of the biomolecules can be totally avoided.

In this work, a new class of inexpensive polymer-based nanostructured Fabry-Perot interferometer (FPI) optical microdevices was developed, offering a potentially powerful label-free technical platform for the detection of protein/cancer biomarkers.

Prior work of the nanostructured FPI microchip focused on the proof-of-concept demonstrations. Experiments found that the sensitivity of the chip could be down to a single layer of molecule level, and the DOL of binding between Protein A and Porcine IgG was lower than 10 pg/mL, which is ~55 fM of Porcine IgG. Herein, the detection of prostate cancer biomarker free prostate-specific antigen (f-PSA) is reported for the first time using this technical platform.

7.2 Biodetection Procedures

7.2.1 Immobilization of Detector mAb on Gold Surface

The immobilization of the detector mAb on the Au-coated surface of the nanostructured FPI microchip is schematically illustrated in Figure 7.1.
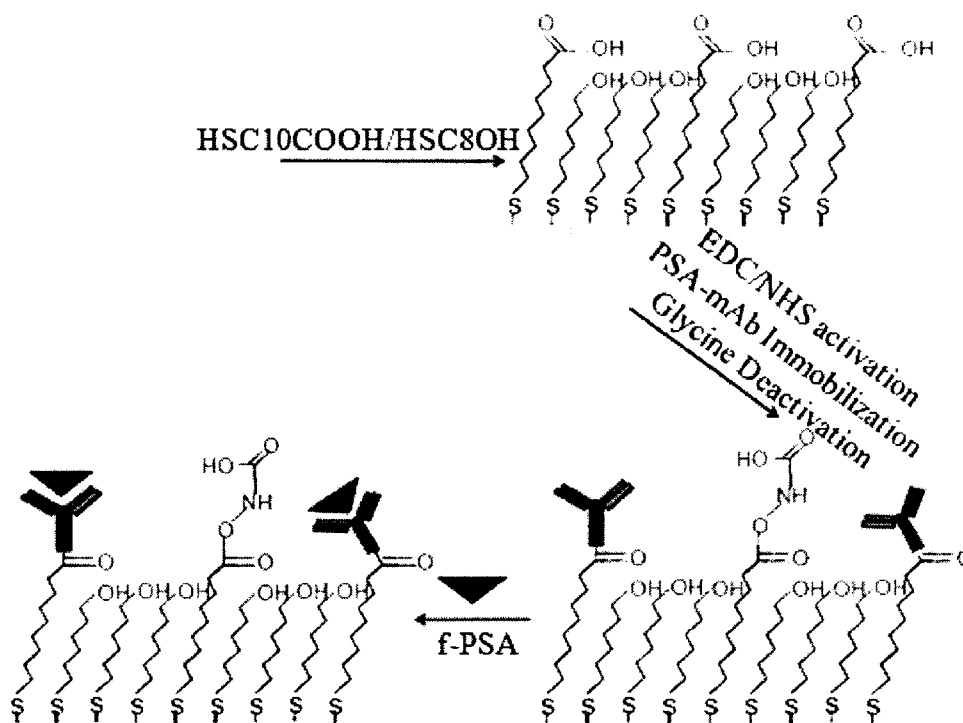
Figure 7.1 Illustration of SAM formation.

The Au-coated surface was first cleaned with O_2 plasma for 15 mins before being bonded with the PDMS microfluidic layer, followed by a self-assembled monolayer (SAM) process by incubation in a mixture of 1 mM HSC10COOH and HSC8OH with molar ratio of 1:10 in absolute ethanol solution overnight. The SAM then was activated by incubation in a pH=7.0, 10 mM phosphate buffer solution (PBS) containing 0.5 mM of EDC/NHS for 2 hrs. The activated SAM was rinsed with the 10 mM PBS and immediately flowed away by a freshly prepared 10 mM PBS solution containing 10

μg/mL of the detector mAb for a 2 or 4 hr incubation. The microchip was then rinsed with the PBS and followed by a 0.2 M glycine PBS solution for 10 mins in order to deactivate the remaining active sites at the SAM. Finally, the microchip was ready for free-PSA (f-PSA) binding detection.

7.2.2 Free PSA Detection

Once the antibodies (mAbs) had been immobilized on the Au-coated nanostructured surface in the microchip, the detection of f-PSA was ready. The f-PSA was the unbounded form of the antigen and normally at the level of 10% of total PSA. A higher amount of f-PSA in a test means a lower chance of cancer. During the experiments, PBS was used as a running buffer to help minimize the nonspecific adsorption of the f-PSA in the tubes and the microfluidic channels.

7.2.3 Control Experiment

Two types of control experiments were designed and carried out to evaluate the specificity/selectivity of the immunoassay using the nanostructured FPI microdevices. First, the binding between the detector mAb and BSA at concentrations of 50, 100, 500, 5,000 pg/mL was evaluated. In addition, the binding between the detector mAb and rabbit IgG at several different concentrations was evaluated.

7.3 Results and Discussions

The average shift of the fringes for the measured transducing signals is obtained by first obtaining the shift of each fringe peak relative to that of the blank Au-coated nanostructure surface or after the antibodies (mAbs) have been immobilized on the nanostructure surface, then averaging the shift of all the peaks. The reference for each average shift is specified in the context in the following sections.

The EOT of the nanostructurelayer and the biomolecules immobilized on it was obtained by performing FT on the measured optical transducing signals, which were described in detail in the report written by T. Zhang et al.[61]. A MATLAB program based on the fast FT algorithm was developed for this calculation.

7.3.1 Surface Functionalization of Au-Coated Nanostructures

The surface functionalization of the Au-coated nanostructures was performed step-by-step, following the protocol as illustrated in Figure 7.1. It is a well-established method to form a mixed SAM of alkanethiols by the adhesion reaction of the thiol group on gold surface. The monolayer was well packed and the tethered carboxylic acid was easily functionalized for biological molecule immobilization. Upon the presence of EDC/NHS, the carboxylic groups form active O-acylisourea intermediates, and readily reacted with primary amine groups which exist at the N-terminus of each polypeptide chain and in the side chain of lysine residues. Because of their positive charge at physiologic conditions, primary amines are usually outward-facing of proteins; hence, they were accessible for conjugation without denaturing protein structure. In such a way, the detector mAbs for f-PSA were covalently attached to the top of the mixed SAMs. The remaining active O-acylisourea intermediate groups were deactivated by the amino acid glycine to avoid non-specific biological attachment caused by the intermediates. At this stage, the mAbswere conjugated to the nanostructured surface and ready for next f-PSA detection.

Each surface chemical modification step changed the local refractive index and the effective optical thickness of the nanostructured surface and wasoptically monitored in real time. The real-time monitoring experiments were carried out on four individual

nanostructured FPI microchips in the Set I, giving consistent results. As an example, Figure 7.2 (A) gives a representative step-by-step measurement during the surface functionalization. The interference fringes (transducing signals) shifted clearly after each step of addition of organic molecules and biomolecules. It should be noted that all these measurements were performed at room temperature. The measured interference fringes for the antibody attachment were obtained after 2 hrs of incubation and three cycles of rigorous PBS solution rinsing. Compared to the fringes obtained on the nanostructured FPI microchip with a blank Au-coated nanostructured surface in the range of 550 nm to 850 nm, typical average shifts were 5.13 ± 0.02 nm after the HSC10COOH/HSC8OH was added and reacted with the gold-coated surface. A shift of 9.48 ± 0.02 nm was observed after EDC/NHS was added and reacted with the surface, and a shift of 13.68 ± 0.02 nm was observed after the antibodies (mAbs) were added and attached to the surface.
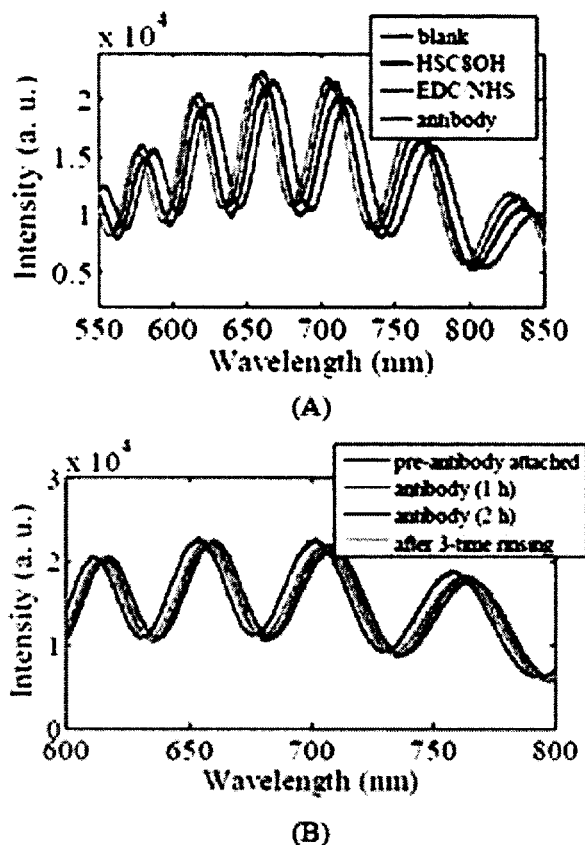
Figure 7.2 Measured signals for antibody attaching process.

The more detailed real-time monitoring of the process of the attachment of antibodies (mAbs) is given in Figure 7.2 (B). When the mAbs were flowed into the chip, the optical signals were monitored at different time intervals. It would take some time for the antibodies to be immobilized and attached to the SAM layer. The measurements showed a clear shift of the fringes after a 1hr incubation at room temperature relative to that of pre-antibody being applied. The shift further increased after a 2 hr incubation, indicating that possibly more antibodies were immobilized or attached. Thereafter, three rigorous rinsings by flowing PBS solution were carried out to remove the unbounded or loosely bounded antibodies. As expected, the shift of the fringes decreased relative to that of pre-antibody attached condition, namely the fringes had a red-shift. Experiments found

that after three cycles of rinsing using PBS solution, no further shift of fringes was observed, suggesting that all unbounded antibodies had been gotten rid of from the microchip. After antibodies were attached and immobilized, the measured final average fringe shift was 4.21 ± 0.02 nm when compared to the fringe of the pre-attachment of antibodies.

The real-time monitoring of the transducing signals is an important step to verify that each chemical modification of the sensing surface has actually occurred. This measurement is particularly useful and effective since there is no need to utilize any fluorescent dyes to tag organic molecules or biomolecules to visually observe and confirm the occurrence of each surface modification. In addition, it was also a simple approach to ensure that the unbounded and loosely bounded molecules had been completely rinsed away. This is a critical step to guarantee consistent measurements from each microchip, especially for future reliable and reproducible arrayed microchips for multiplexed biodetection.

7.3.2 <u>Detection of Cancer Biomarker</u> <u>Free-PSA</u>

After antibodies (mAbs) were immobilized on the Au-coated nanostructured surface inside the microchip, the quantitative measurement of f-PSA was carried out. This part included upper detection range and DOL.

For the upper detection range of the f-PSA, the effect of the amount of antibodies immobilized on microchips (the same microchips used in experiments as reported in Figure 7.2) were evaluated. In this set of experiments, the antibody (mAb) concentration was 10 µg/mL and the incubation time was 2 hrs. Concentrations of f-PSA flowed onto the microchip were 100, 500, and 5,000 pg/mL in a PBS solution. The order of the

experiments was as follows. The f-PSA was flowed into microchip from lower concentration to higher concentration. For instance, the f-PSA at a concentration of 100 pg/mL was flowed into the chip first. After a 45 min incubation, PBS solution was flowed to rinse the microchip three times and measurements were carried out. Then, the f-PSA at higher concentrations (e. g., 500 and 5,000 pg/mL) were flowed into the chip. After incubation, a rinsing and measurement routine was carried out again. It was found that the binding sites had been almost totally occupied after f-PSA with a concentration of 500 pg/mL was flowed into the chip since interference fringes remained essentially unchanged even more f-PSA was added. As an example, the measurement in Figure 7.3 showed when the concentration of f-PSA reached 5,000 pg/mL, there was little observable shift of fringes compared to that of f-PSA at a concentration of 500 pg/mL, indicating the upper detection range of f-PSA was about 500 pg/mL.
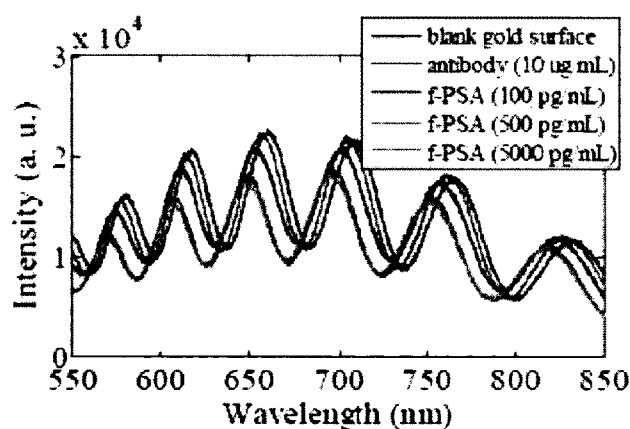
Figure 7.3 Upper detection range testing.

In order to expand the upper detection range, more antibodies on the microchip have to be immobilized so that more binding sites are available for f-PSA. However, it should be also noted that the amount of the antibodies cannot be too excessive; otherwise,

the antibodies immobilized on the sensing surface are too closely packed and crowded to allow f-PSA to approach the binding sites efficiently and consequently to be attached to them. For instance, in one of these experiments, antibodies (mAbs) at a concentration of 100 μg/mL were immobilized on the sensing surface with a 24 hr incubation, and the f-PSA at several concentrations was flowed into the chip for the testing. After rinsing by the PBS solution, it turned out that essentially no f-PSA had been attached to the antibodies, resulting in negligible shift in the fringes.

For the DOL, the experiments were carried out on four individual microdevices in Set II. All the measurements gave consistent results. In this case, the antibodies at concentration of 10μg/mL were flowed into the chip with incubation time of 4 hrs. The concentrations of f-PSA flowed into the microchip were 0, 5, 10, 50, 100 and 500 pg/mL in a PBS solution. The f-PSA was flowed into microchip from lower concentration to higher concentration sequentially. Specifically, the f-PSA at a concentration of 0 pg/mL was flowed into the chip first; after sufficient time (45 mins) for incubation, the PBS solution was flowed to rinse the microchip three times and measurements were carried out. Thereafter, the f-PSA at concentration of 5 pg/mL was flowed into the microchip for the testing. After a 45 min incubation, a rinsing and measurement routine was carried out. Similarly, the experiments were performed for f-PSA at concentrations of 10, 50, 100, and 500 pg/mL in sequence, respectively. All these results were obtained by multiple measurements on four individual microchips, and the average fringe shift for each concentration was obtained accordingly.

A representative measurement of the transducing signals with the f-PSA flowed into microchip at concentrations of 0 and 5 pg/mL is shown in Figure 7.4.
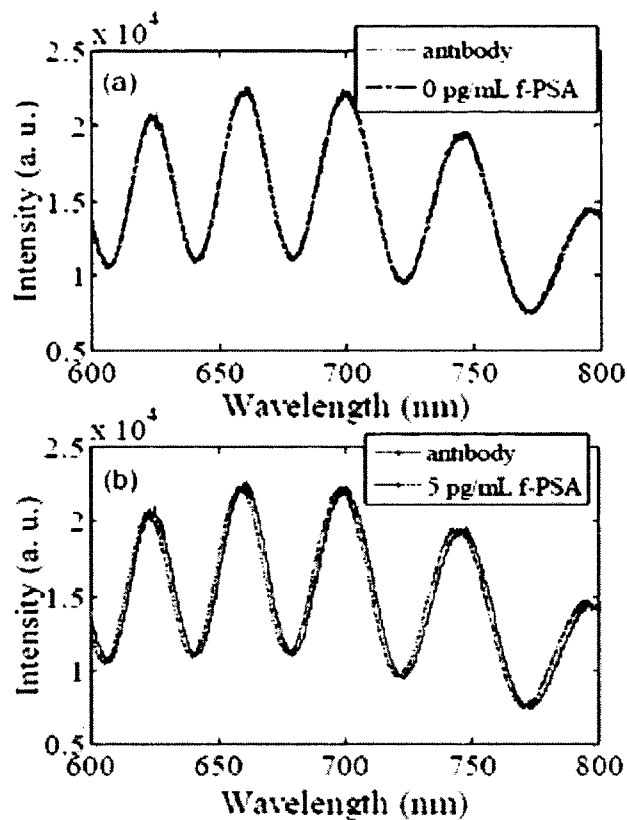
Figure 7.4 Measured signals with different concentrations of f-PSA.

As expected, the interference fringes showed no or a negligible shift with the f-PSA at 0 pg/mL, since no f-PSA was actually available to be bounded to the antibodies. The average shift of the fringes was about 2.19 ± 0.02 nm with the f-PSA at a concentration of 5 pg/mL in the range of 550 nm to 850 nm, relative to the fringes for the device with immobilized antibodies. By increasing the concentration of the f- PSA to 10, 50, 100, and 500pg/mL in sequence, the average fringe shift increased as expected since increasing amount of f-PSA were bounded to the antibodies. The rest of the optical signals were not overlaid in the plot in order to make the shift clearly readable and visible for the f-PSA at 5 pg/mL. Experiments have also found that the fringe shift was not clearly distinguishable when the concentration of the f-PSA was below 5 pg/mL using

these microchips for the experiments. This undistinguishable shift might be due to the resolution limit (± 0.02 nm) of the optical spectrometer used in the experiments or the DOL of these microchips, indicating that the DOL of current microchips for the f-PSA detection is about 5 pg/mL.

FT has been applied on the measured transducing signals, and the EOT of the nanostructured layer and the biomolecules immobilized on it was obtained. Using the EOT after the immobilization of the antibodies as a reference, which is 7,487 ± 2 nm, ΔEOT was obtained after the application of f-PSA at different concentrations. In Figure 7.5, ΔEOT under different concentrations of the f-PSA is summarized.
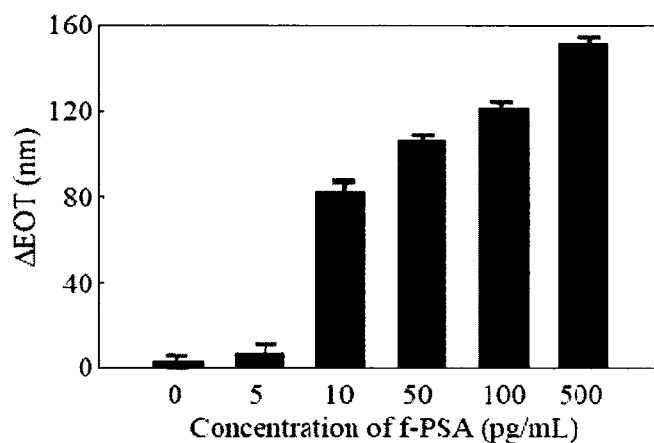
Figure 7.5 Changes of EOT with different concentrations of f-PSA.

As expected, the lower the concentration of the f-PSA, the less the f-PSA was bounded to the antibodies, hence the smaller the ΔEOT. The EOT for each case was obtained by averaging several measurements. Again, as can be seen based on the ΔEOT, the DOL is about 5 pg/mL or lower, which is ~140 fM, for the detection of f-PSA.

7.3.3 Control Experiment

Finally, control experiments were carried out on microdevices to demonstrate the specificity and selectivity of the bioassay. In this case, the incubation time of antibodies at a concentration of 10 µg/mL was 4 hrs. BSA solutions with different concentrations of 50, 100, 500, and 5,000 pg/mL were flowed into the microdevice. For each concentration of BSA, the incubation time was 60 mins, followed by rigorous PBS solution rinsing three times. Representative measurements are given in Figure 7.6. No or negligible shifts in fringes were observed when BSA with four different concentrations was applied to microchips, confirming the specific recognition between antibodies (mAbs) and f-PSA. Similarly, experiments were performed to check if antibodies were bounded to rabbit IgG at concentrations of 50, 100, 500, and 5,000 pg/mL, respectively. No or negligible shifts in fringes were observed, indicating again that antibodies were only specific to f-PSA. Overall, these two types of control experiments (BSA and rabbit IgG) suggested excellent selectivity of the immunoassay.
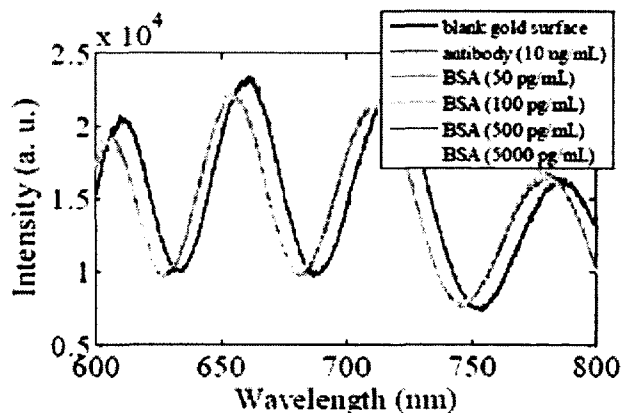
Figure 7.6 Controlled experiment using microdevices.

It should be noted that even though the three sets of devices have somewhat different transducing signals (i. e., the positions of the fringe peaks were different), for each set of the devices, a nanostructured FPI device with a blank Au-coated nanostructured surface from the same set was used as the reference. Hence, consistent measurement results for the bioassay were obtained for all three types of tests.

As demonstrated, the nanostructured FPI microdevices offered sufficient sensitivity for the detection of clinically relevant cancer biomarkers, typically in the range of picomolar concentration levels or lower. Initial experiments have also found that the sensitivity of a nanostructured FPI device can be further improved by increasing its finesse by changing the size of and interspacing among nanopores, under further investigation in our lab. Furthermore, even though this work only reports the detection of one cancer biomarker, since arrayed devices can be batch-fabricated in an inexpensive and efficient manner, a disposable platform based on arrayed nanostructured FPI devices which can be developed for the multiplexed biomolecular detection and analysis may be seen in the future.

7.4   Summary

In summary, the detection of f-PSA has been demonstrated using nanostructured FPI microchips successfully. It has been demonstrated that the chemical and biochemical functionalization of the nanostructured sensing surface can be monitored in real-time. The upper dynamic detection range can be changed by varying the amount of capture antibodies immobilized on the sensing surface. Currently, the DOL of the nanostructured FPI microchip for f-PSA is about 5 pg/mL, which can be further lowered by optimizing optical properties of the microchip. Experiments have also demonstrated the high

specificity and selectivity of the immunoassay used in the biosensing, indicating the great promise for the detection of cancer biomarkers at trace levels in biofluids. Finally, due to the feasibility of fabricating hundreds of nanostructured FPI microdevices on a single chip, this technical platform offers great potential for highly multiplexed, label-free biodetection for the diagnosis of various cancers or diseases in a clinic setting and for anticancer drug screen and discovery applications.

CHAPTER 8

CONCLUSIONS AND FUTURE WORK

8.1   Conclusions

In this dissertation, an innovative biosensing platform using a nanostructured Fabry-Perot interferometer was developed, fabricated, and tested. This biosensing platform was tested for proof-of-concept demonstration and applied for ultrasensitive detection of the cancer biomarker f-PSA.

For the past few decades, biosensors have seen an expanding market, particularly in the current climate of growing and aging populations. The need for accurate, inexpensive, and simple biosensors is going to continually increase. Biosensing can be achieved by labeled and label-free techniques. Traditional labeled biosensing techniques require labels such as fluorescent dyes, radioisotopes or epitope tags to be attached to analytes in order to identify whether there are interactions or not. Therefore, the labeled technology has shortcomings, such as the limited shelf life of labels, the inherent toxicity caused by labels which could also modify properties of biomolecules, the need for specific read-out instruments with intelligent software, and skilled lab personnel. In contrast to labeled biosensing, label-free techniques are attractive for biosensing since no labels need to be attached to biomolecules. As a result, the experimental cost can be reduced dramatically, and the possible perturbation of properties of biomolecules can be completely avoided. For label-free biosensing techniques, there are three major types of

93

label-free biosensors in terms of transducing mechanisms. These transducing mechanisms include electrical, mechanical, and optical transductions. Due to its high degree of sensitivity, the capability of multiplexing, and the immunity to the environmental noise, the optical technique is more attractive for sensing applications than other techniques. With the advancement of micro- and nanofabrication technologies, many optical components have been miniaturized. As a result, the field of microoptics and nanooptics has emerged, triggering extensive research to scale down the optics-based sensing platforms for past decades. One example is the miniaturization of Fabry-Perot interferometers. FPIs have been designed and implemented for chemical sensing, gas sensing, biosensing, ultrasonic sensing, and optical modulation. However, for biochemical sensing, a conventional FPI has following intrinsic limitations. First, it has a limited sensing surface area, which means that binding sites available for biomolecules are limited, resulting in low transducing signals. Second, the optical sensitive range/area is essentially limited only to the surface of the planar glass plate. Finally, it has a limited intensity of transducing signals due to optical power losses of the reflected light from the FPI at the interface of FPI plates.

In order to enhance the optical transducing signal, an innovative biosensing platform using a nanostructured FPI has been designed. Each FPI consists of a PDMS plate, an Au-coated nanopore layer and a glass plate. The Au-coated nanopore layer is anchored on the glass plate, forming a nanopore plasmonic substrate. The PDMS microfluidic layer can be batch fabricated using an inexpensive, rapid, soft lithography process. The nanopore structures can be fabricated using a standard two-step anodization process. The Au-coated nanostructure layer inside the FPI cavity offers significantly

enhanced optical interference signals due to the L-SPR effect and the increased sensing surface area.

Measurements have been carried out on the prototype devices to evaluate their performance using different chemicals. Systematic experiments found that for an Au-coated nanostructured FPI with a nanopore size of 50 nm, it had approximately a twenty fold improvement in FSR, approximately a two fold improvement in finesse and approximately a four fold improvement in contrast of optical transducing signals over a traditional µFPI even without any device performance optimization. From the comparison, this novel design offers at least three advantages over a traditional µFPI including the increased sensing surface area, the extended penetration depth of the excitation light, and the tremendous amplification of the optical transducing signal due to the L-SPR effect. The Raman signal of R6G was also amplified significantly on the Au-coated AAO, which indirectly confirmed that the optical signal enhancement is enabled by the nanoscale roughness of the Au thin film coated on the nanopore structures due to the L-SPR effect. The FEA of the intensity distribution for arrayed nanopores also confirmed great enhancements of optical transducing signals.

The control experiment incubating IgG on gold surface confirmed the small affinity of IgG to the Au-coated sensing surface. Then, using fluorescent images, shifts of interference fringes for IgG and BSA interaction were indirectly confirmed.

Using this technical platform, the immobilization of capture proteins (Protein A) on the nanostructure layer and their binding with IgG were monitored in real time, resulting in the shift of interference fringes of optical transducing signals, which demonstrated the operation and label-free biomolecular detection capability of the

nanostructured FPI at room temperature. The Au-coated nanostructure layer inside the FPI cavity offers significantly enhanced optical interference signals due to the L-SPR effect and the increased sensing surface area. FT was performed on the measured interference spectra for simplifying the transducing signal analysis. Experimental results indicated that DOL of the nanostructured FPI biosensor should be lower than 10 pg/mL for IgG-Protein A binding, which is ~55 fM of IgG. Control experiments were performed to check if Sea Block binds with Protein A or IgG to confirm that the biodetection is only specific to Protein A and IgG recognition. Measurements found that for both cases, interference fringes had a negligible shift, indicating Sea Block does not bind with either Protein A or IgG.

After the proof-of-concept demonstration, the label-free detection of a cancer biomarker f-PSA using this nanostructured FPI microchip was performed. Specifically, the prostate cancer biomarker f-PSA was detected with a mouse anti-human PSA monoclonal antibody (mAb) as the receptor. Experiments found that the DOL of the current Au-coated nanostructured FPI microchip for f-PSA was about 5 pg/mL and the upper detection range for f-PSA could be dynamically changed by varying the amount of mAb immobilized on the sensing surface. Control experiments also demonstrated that the immunoassay protocol used in these experiments showed excellent specificity and selectivity, suggesting the great potential to detect cancer biomarkers at trace levels in biofluids.

In summary, in this dissertation an innovative biosensing platform has been designed, fabricated, and tested. This nanostructured FPI microchip-based platform could

provide an ideal ultrasensitive label-free biodetection tool for point-of-care diagnostic application and anti-cancer drug screen and discovery.

8.2   Future Work

The ultrasensitive label-free biosensor has been successfully developed and demonstrated in this dissertation. However, there are a few recommendations for further improvements.

In this dissertation, nanostructures have arrayed pores with the size of ~50 nm in diameter. Experiments found that the size of the nanostructure, as well as the spacing among them, could be tuned by changing operational parameters during the fabrication process. Therefore, the sensitivity of a nanostructured FPI device may be further improved by changing the size of and interspacing among nanopores, which is under further investigation.

Due to the advantage of an inexpensive, rapid, soft lithography fabrication process, a disposable platform based on arrayed nanostructured FPI devices can be developed for the multiplexed biomolecular detection and analysis in the future, as shown in Figure 8.1.
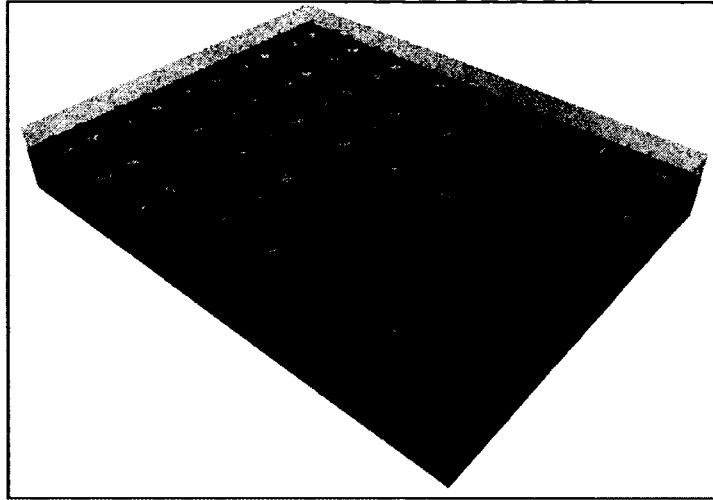
Figure 8.1 Arrayed nanostructured FPIs on a single chip.

A close up look of a single nanostructured FPI from arrayed nanostructured FPIs is shown in Figure 8.2.
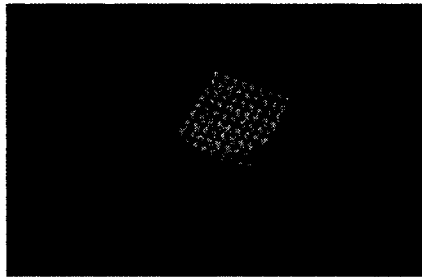
Figure 8.2 A close up look of a single nanostructured FPI.

The optical signal input and output module were achieved by anexpensive customized optical fiber probe, shown inFigure 8.3.
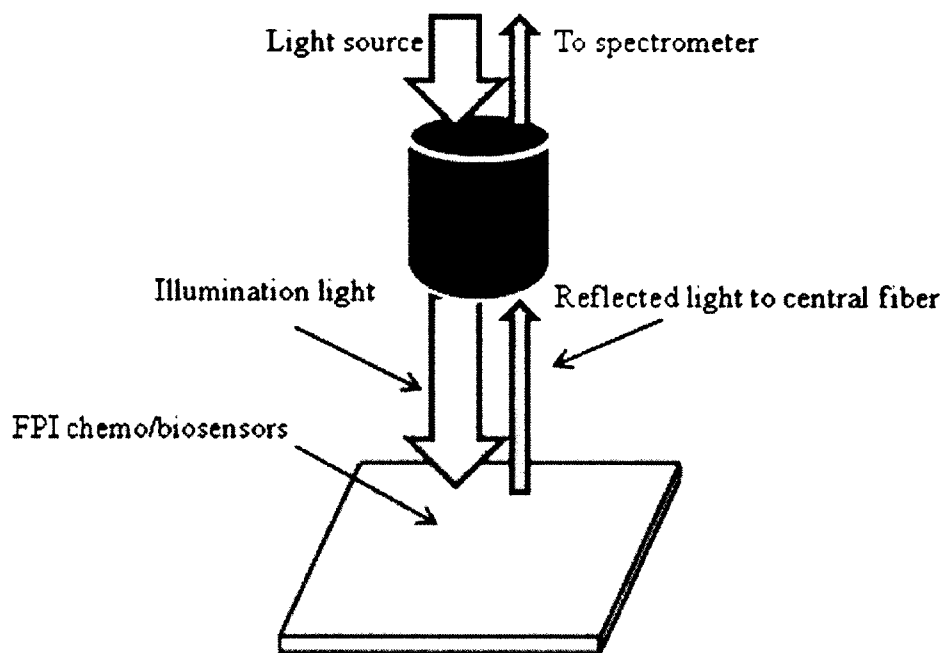
Figure 8.3 Reflected signal measurement setup.

This module consists of a tight bundle of seven optical fibers in a stainless steel ferrule, as shown inFigure 8.4. The center fiber is to collect the reflected light while the outer six fibers deliver the illumination light to the FPI chemo/biosensor. The incident light and reflected transducing light are both on the same side, which makes the structure complicated and expensive.
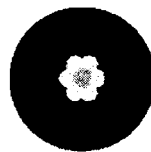
Figure 8.4 End surface of customized probe.

In the reflected transducing signal measurement setup,each single biosensorcan be tested at one time. From the fabrication process, it has been found that the nanostructure can be made semi-transparent. By using the transmitted optical transducing signal, a

simple setup can be achieved to separate the incident light and the transducing light as shown in Figure 8.5. In this transmitted transducing signal measurement setup, only one light source is needed and multiple biosensors can be tested simultaneously.

Light source

Illumination light

Arrayed chemo/biosensors

Transmitted light
to separate fibers

To spectrometer
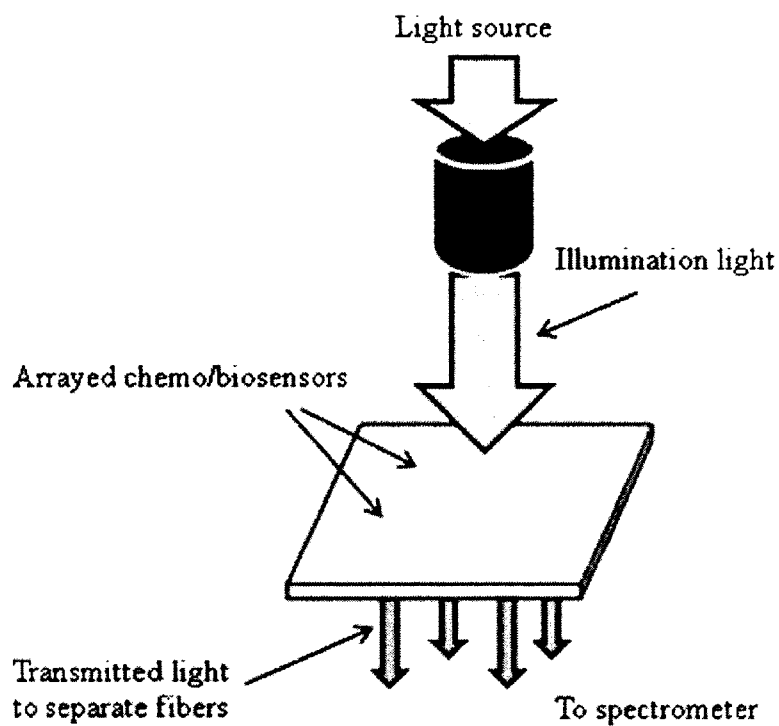
Figure 8.5 Transmitted signal measurement setup.

APPENDIX

COMSOL IMPLEMENTATION

COMSOL Multiphysics is a powerful FEA software. The graphical user interface for COMSOL consists of several windows, such as Model Builder, Settings, Graphics, Messages, Progress, Help, Main Menu, and Main Toolbar. The process flow for simulation includes model wizard setup, global definition for parameters, geometry, material, module definition, mesh, study, and results.

The geometry for arrayed nanopores is shown in Figure A-1. The bottom domain is the alumina domain. The diameter of a nanopore is 50 nm. The spacing among nanopores is 50 nm. The top domain is the air domain. On top of the air domain is a 5 nm thick gold layer. L is defined as the pore to pore distance. D is the pore diameter.
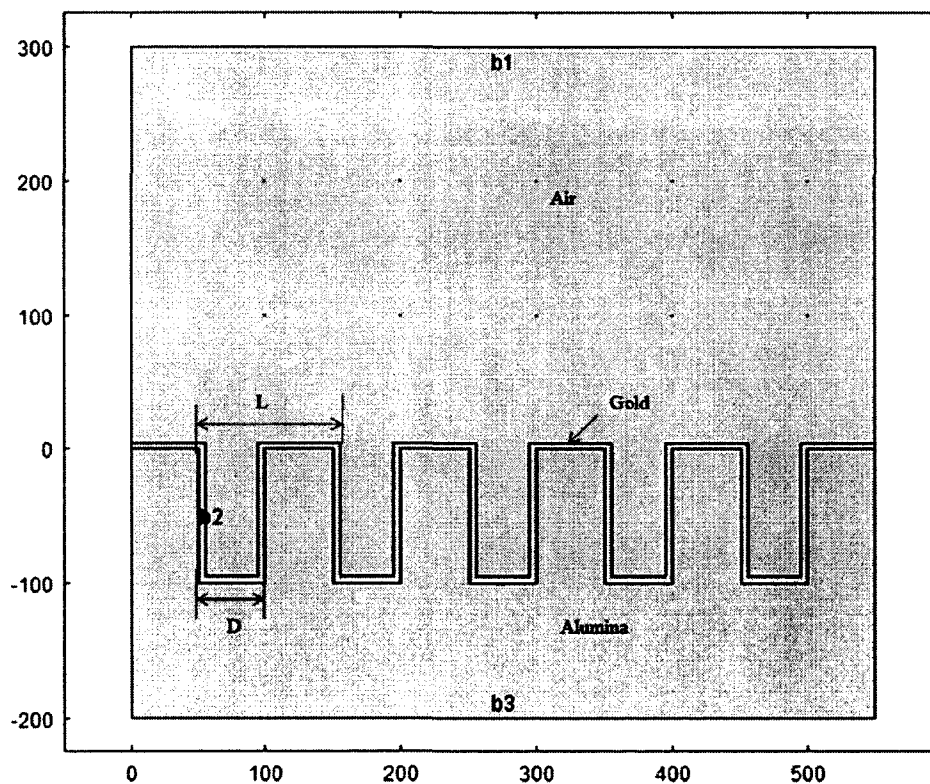
Figure A-1 Geometry of arrayed nanopores.

In order to simulate arrayed nanopores, the periodic boundary condition is set for a single nanopore cell on both left and right hand side boundaries. The boundary on the top of the geometry is set as the input source. The geometry of a nanopore with periodic boundaries is shown in Figure A-2.
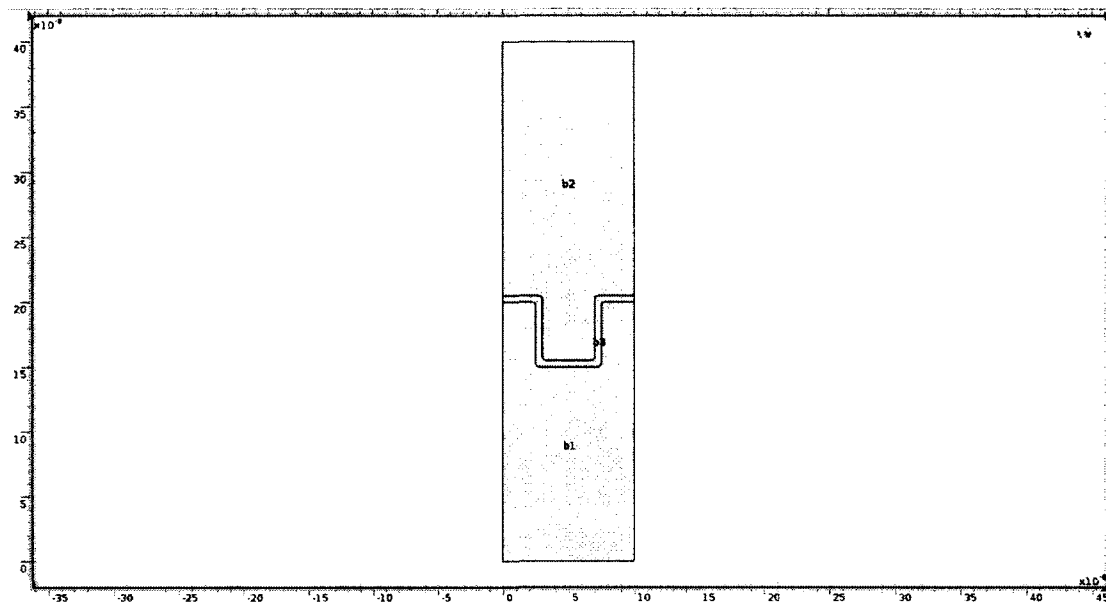
Figure A-2 Geometry of a nanopore with periodic boundaries.

Material properties are assigned to each domain from the material library. The refractive index for air is 1. The refractive index for alumina is 1.77 at the wavelength of 600 nm. The relative permittivity for gold is -1.74-5.4i at the wavelength of 600 nm.

Mesh for the gold domain is customized with a maximum element size of 0.5 nm in order to get an extremely fine mesh. The remaining domain is predefined coarse to balance the calculation time. The mesh result is shown in Figure A-3. The framed part is the customized mesh for the gold domain.
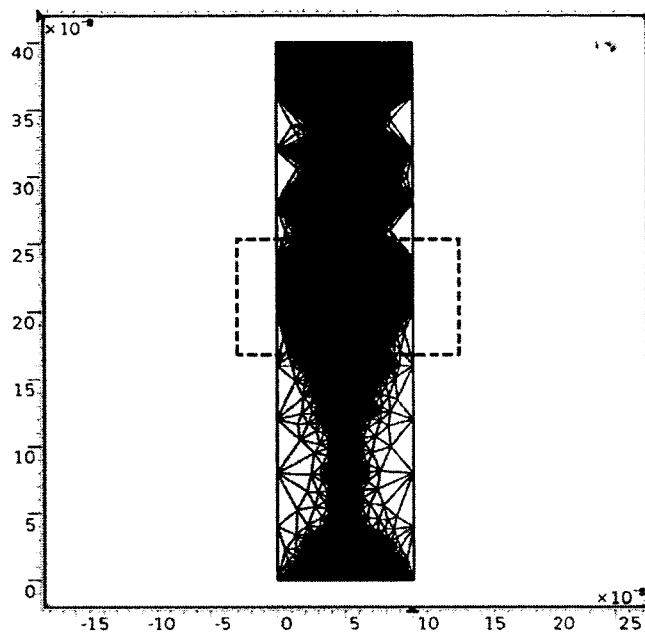
Figure A-3 Mesh for a single nanopore cell.

In order to quantify the enhancement of gold coated nanopores comparing to bare nanopores, the data from COMSOL are exported to the text file and then imported into the excel file. After converting the COMSOL data into the excel file, MATLAB is used to load the data and perform the calculation. All mesh points in the nanopore region are added together. Thereafter, the sum is divided by the number of points to get an average value of magnitude enhancement.

REFERENCES

[1]   L. C. Clark, Jr. and C. Lions, "Electrode systems for continuous monitoring in cardiovascular surgery," *Automated and Semi-Automated Systems in Clinical Chemistry*, vol. 102, 2006, pp. 29-45.

[2]   E. C. Nice and B. Catimel, "Instrumental biosensors: new perspectives for the analysis of biomolecular interactions," *Bioessays*, vol. 21, 1999, pp. 339-352.

[3]   H. H. We, "Chemical sensors and biosensors, update, what, where, when and how," *Biosensors and Bioelectronics*, vol. 14, 1999, pp. 237-242.

[4]   M. E. Tess and J. A. Cox, "Chemical and biochemical sensors based on advances in materials chemistry," *Journal of Pharmaceutical and Biomedical Analysis*, vol. 19, 1999, pp. 55-68.

[5]   C. M. Braguglia, "Biosensors: an outline of general principles and application," *Chemical and Biochemical Engineering Quarterly*, vol. 12, 1998, pp. 183-190.

[6]   D. R. Thevenot, K. Toth, R. A. Durst and G. S. Wilson, "Electrochemical biosensors: recommended definitions and classification," *Biosensors and Bioelectronics*, vol. 16, 2001, pp. 121-131.

[7]   M. Mascini and S. Tombelli, "Biosensors for biomarkers in medical diagnostics," *Biomarkers*, vol. 13, 2008, pp. 637-657.

[8]   T. Vo-Dinh and B. Cullum, "Biosensors and biochips: advances in biological andmedical diagnostics," *Fresenius Journal of Analytical Chemistry*, vol. 366, 2000, pp. 540-551.

[9]   J. Polster, G. Prestel, M. Wollenweber, G. Kraus and G. Gauglitz, "Simultaneous determination of penicillin and ampicillin by spectral fibre-optical enzyme optodes and multivariate data analysis based on transient signals obtained by flow injection analysis," *Talanta*, vol. 42, 1995, pp. 2065-2072.

[10] A. Erdem, K. Kerman, B. Meric, U. S. Akarca and M. Ozsoz, "A novelhybridization indicator methylene blue for the electrochemical detection of shortDNA sequences related to the hepatitis B virus," *Analytica Chimica Acta*, vol. 422, 2000, pp. 139-149.

[11] S. Sawata, E. Kai, K. Ikebukuro, T. Iida, T. Honda and I. Karube, "Application of peptide nucleic acid to the direct detection of deoxyribonucleic acid amplified by polymerase chain reaction," *Biosensors and Bioelectronics*, vol. 14, 1999, pp. 397-404.

[12] C. M. Niemeyer, L. Boldt, B. Ceyhan and D. Blohm, "DNA-directed immobilization: efficient, reversible, and site-selective surface binding of proteins by means of covalent DNA-streptavidin conjugates," *Analytical Biochemistry*, vol. 268, 1999, pp. 54-63.

[13] G. Marrazza, I. Chianella and M. Mascini, "Disposable DNA electrochemical sensor for hybridization detection," *Biosensors and Bioelectronics*, vol.14, 1999, pp. 43-51.

[14] A. Bardea, F. Patolsky, A. Dagan and I. Willner, "Sensing and amplification of oligonucleotide-DNA interactions by means of impedance spectroscopy: a route to a Tay-Sachs sensor," *Chemical Communications*, vol. 21, 1999, pp. 21-22.

[15] J. Wang, G. Rivas, J. R. Fernandes, J. L. L. Paz, M. Jiang and B. Waymire, "Indicator-free electrochemical DNA hybridization biosensor," *Analytica Chimica Acta*, vol. 375, 1998, pp. 197-203.

[16] H. Mukundan, H. Xie, A. S. Anderson, W. K. Grace, J. E. Shively and B. I. Swanson, "Optimizing a waveguide-based sandwich immunoassay for tumor biomarkers: evaluating fluorescent labels and functional surfaces," *Bioconjugate Chemistry*, vol. 20, 2009, pp. 222-230.

[17] X. Liu, Q. Dai, L. Austin, J. Coutts, G. Knowles, J. Zou, H. Chen and Q. Huo, "A one-step homogeneous immunoassay for cancer biomarker detection using gold nanoparticle probes coupled with dynamic light scattering," *Journal of the American Chemical Society*, vol. 130, 2008, pp. 2780-2782.

[18] D. Georganopoulou, L. Chang, J. Nam, C. Thaxton, E. Mufson, W. Klein and C. Mirkin, "Nanoparticle-based detection in cerebral spinal fluid of a soluble pathogenic biomarker for Alzheimer's disease," *Proceedings of the National Academy of Sciences of the United States of America*, vol. 102, 2005, pp. 2273-2276.

[19] C. Haynes, A. McFarland and R. V.Duyne, "Surface enhanced Raman spectroscopy," *Analytical Chemistry*, vol. 4, 2005, pp. 338-346.

[20] E. Smith and R. Corn, "Surface Plasmon resonance imaging as a tool to monitor biomolecular interactions in an array based format," *Applied Spectroscopy*, vol. 57, 2003, pp. 320-332.

[21] S. Mandal and D. Erickson, "Nanoscaleoptofluidic sensor arrays," *Optical Express*, vol. 16, 2008, pp. 1623-1631.

[22]   L. L. Chan, S. Gosangari, K. L. Watkin and B. T. Cunningham, "Label-free imaging of cancer cells using photonic crystal biosensors and application to cytotoxicity screening of a natural compound library," *Sensors and Actuators B*, vol. 132, 2008, pp. 418-425.

[23]   M. Wilson and W. Nie, "Multiplex measurement of seven tumor markers using an electrochemical protein chip," *Analytical Chemistry*, vol. 78, 2006, pp. 6476-6483.

[24]   W. Henne, D. Doorneweerd, J. Lee, P. Low and C. Savran, "Detection of folate binding protein with enhanced sensitivity using a functionalized quartz crystal microbalance sensor," *Analytical Chemistry*, vol. 78, 2006, pp. 4880-4884.

[25]   G. Wu, R. Datar, K. Hansen, T. Thundat, R. Cote and A. Majumdar, "Bioassay of prostate-specific antigen (PSA) using microcantilevers," *Nature Biotechnology*, vol. 19, 2000, pp. 856-860.

[26]   A. Gupta, P. Nair, D. Akin, S. Broyles, M. Ladisch, A. Alam and R. Bashir, "Anomalous resonance in a nanomechanical biosensor," *Proceedings of the National Academy of Sciences of the United States of America*, vol. 103, 2006, pp. 13362-13367.

[27]   G. Zheng, F. Patolsky, Y. Cui, W. Wang and C. M. Lieber, "Multiplexed electrical detection of cancer markers with nanowire sensor arrays," *Nature Biotechnology*, vol. 23, 2005, pp. 1294-1301.

[28]   R. Tian, S. Regonda, J. Gao, Y. Lin and W. Hu, "Ultrasensitive protein detection using lithographically defined Si multi-nanowire field effect transistors," *Lab on a Chip*, vol. 11, 2011, pp. 1952-1961.

[29]   S. D. Alvarez, C. Li, C. E. Chiang, I. K. Schuller and M. J. Sailor, "A label-free porous alumina interferometric immunosensor," *ACS Nano*, vol. 3, 2009, pp. 3301-3307.

[30]   S. Nie and S. Emory, "Probing single molecules and single nanoparticles by surface enhanced Raman scattering," *Science*, vol. 275, 1997, pp. 1102-1106.

[31]   A. Yanik, A. Cetin, M. Huang, A. Artar, S. Mousavi, A. Khanikaev, J. Connor, G. Shvets and H. Altug, "Seeing protein monolayers with naked eye through plasmonic nano resonances," *Proceedings of the National Academy of Sciences of the United States of America*, vol. 108, 2005, pp.11784-11789.

[32]   X. Gao, Y. Cui, R. Levenson, L. Chung and S. Nie, "In vivo cancer targeting and imaging with semiconductor quantum dots," *Nature Biotechnology*, vol. 22, 2004, pp. 969-976.

[33] M. Hu, J. Yan, Y. He, H. Lu, L. Weng, S. Song, C. Fan and L.Wang, "Ultrasensitive, multiplexed detection of cancer biomarkers directly in serum by using a quantum dot-based microfluidic protein chip,"*ACS Nano*, vol. 4, 2010, pp. 488-494.

[34] R. Gaster, D. Hall, C. Nielsen, S. Osterfeld, H. Yu, K. Mach, R. Wilson, B. Murmann, J. Liao, S. Gambhir and S. Wang, "Matrix-insensitive protein assays push the limits of biosensors in medicine," *Nature Medicine*, vol. 15, 2009, pp. 1327-1332.

[35] V. Lin, K. Motesharei, K. Dancil, M. Sailor and M. Ghadiri, "A porous silicon-based optical interferometric biosensor," *Science*, vol. 278, 1997, pp. 840-843.

[36] S. Pan and L. Rothberg, "Interferometric sensing of biomolecular binding using nanoporous aluminum oxide templates," *Nano Letters*, vol. 3, 2003, pp. 811-814.

[37] L. Zhou, L. Ou, X. Chu, G. Shen and R. Yu, "Aptamer-based rolling circle amplification: a platform for electrochemical detection of protein," *Analytical Chemistry*, vol. 79, 2007, pp. 7492-7500.

[38] Y. Imafuku, G. S. Omenn and S. Hanash, "Proteomics approaches to identify auto-immune antibodies as cancer biomarkers," *Disease Markers*, vol. 20, 2004, pp. 149-153.

[39] H. J. Lee, A. Wark and R. M. Corn, "Microarray methods for protein biomarker detection," *Analyst*, vol. 133, 2008, pp. 975-983.

[40] D. Healy, C. Hayes, P. Leonard, L. McKenna and R. O'Kennedy, "Biosensor developments: application to prostate-specific antigen detection," *Trends Biotechnology*, vol. 25, 2007, pp. 125-131.

[41] S. Ray, G. Mehta and S. Srivastava, "Label-free detection techniques for protein microarrays:Prospects, merits and challenges," *Proteomics*, vol. 10, 2010, pp. 731-748.

[42] V. Espina, E. C. Woodhouse, J. Wulfkuhleand H. D. Asmussen, "Protein microarray detection strategies: focus on direct detection technologies," *Journal of Immunological Methods*, vol. 290, 2004, pp. 121-133.

[43] P. S. Cremer, "Liquid crystalline platforms offer fast, simple and inexpensive detection of incoming analytes on two-dimensional fluid biomembrane mimics," *Nature Biotechnology*, vol. 22, 2004, pp. 172-173.

[44] Y. H. Yun, E. Eteshola, A. Bhattacharya, Z. Dong, J. S. Shim, L. Conforti, D. Kim, M. J. Schulz, C. H. Ahn and N. Watts, "Tiny medicine: nanomaterial-based biosensors," *Sensors*, vol. 9, 2009, pp. 9275-9299.

[45]   B. Malhotra and A. Chaubey, "Biosensors for clinical diagnostics industry," *Sensors and Actuators B*, vol. 91, 2003, pp. 117-127.

[46]   N. Ramachandran, D. Larson, P. Stark, E. Hainsworth and J. LaBaer, "Emerging tools for real-time label-free detection of interactions on functional protein microarrays," *FEBS Journal*, vol. 272, 2005, pp. 5412-5425.

[47]   Y. Cui, Q. Wei, H. Park and C. M. Lieber, "Nanowire nanosensors for highly sensitive and selective detection of biological and chemical species," *Science*, vol. 293, 2001, pp. 1289-1292.

[48]   A. Mulchandani and N. V. Myung, "Conducting polymer nanowires-based label-free biosensors," *Biotechnology*, vol. 22, 2011, pp. 502-508.

[49]   R. E. Kunz and K. Cottier, "Optimizing integrated optical chips for label-free (bio-) chemical sensing," *Analytical and Bioanalytical Chemistry*, vol. 384, 2006, pp.180-190.

[50]   N. R. Frometa, "Cantilever Biosensors," *Biotecnologia Aplicada*, vol. 23, 2006, pp. 320-323.

[51]   J. Han, "Fabry-Perot cavity chemical sensors by silicon micromachining techniques," *Applied Physics Letters*, vol. 74, 1999, pp. 445-447.

[52]   N. Neumann, M. Ebermann, K. Hiller and S. Kurth, "Tunable infrared detector with integrated micromachined Fabry-Perot filter," *Proceedings of the SPIE*, vol. 6466, 2007, p. 646606.

[53]   L. Que, "Two-dimensional tunable filter array for a matrix of integrated fiber optic input-output light channels," US Patent 6449410, September 10, 2002.

[54]   L. Que, "Raman system on a chip," US Patent 7505128, March 17, 2005.

[55]   T. Dohi, K. Mstsumoto and I. Shimoyama, "The optical blood test device with the micro Fabry-Perot interferometer," *Proceedings of IEEE MEMS*, 2004, pp. 403-406.

[56]   T. Dohi, K. Mstsumoto and I. Shimoyama, "The micro Fabry-Perot interferometer for the spectral endoscope," *Proceedings of IEEE MEMS*, 2005, pp. 830-833.

[57]   S. Kingsmore, "Antiviral market overview," *Nature Reviews Drug Discovery*, vol. 1, 2006, pp. 11-12.

[58]   H. Ren, F. Vollmer, S. Arnold and A. Libchaber, "High-Q microsphere biosensor analysis for adsorption of rodlike bacteria," *Optical Express*, vol. 15, 2007, pp. 17410-17423.

[59] J. T. Gohring, P. S. Dale and X. Fan, "Detection of HER2 breast cancer biomarker using the opto-fluidic ring resonator biosensor," *Sensors and Actuators B*, vol. 146, 2010, pp. 226-230.

[60] L. Washburn, L. C. Gunn and R. C. Bailey, "Label-free quantitation of a cancer biomarker in complex media using silicon photonic microring resonators," *Analytical Chemistry*, vol. 81, 2009, pp. 9499-9506.

[61] T. Zhang, P. Pathak, S. Karandikar, R. Giorno and L. Que, "A polymer nanostructured Fabry-Perot interferometer based biosensor," *Biosensors and Bioelectronics*, vol. 30, 2011, pp. 128-132.

[62] J. Homola, "Present and future of surface plasmon resonance biosensors," *Analytical and Bioanalytical Chemistry*, vol. 37, 2006, pp.528-539.

[63] I. M. White, H. Oveys, and X. Fan, "Liquid-core optical ring resonator sensors," *Optics Letters*, vol. 31, 2006, pp.1319-1321.

[64] Y. Guo, J. Ye, C. Divin,T. P. Thomas, A. Myc, T. F. Bersano-Begey, J. R. Baker and T. B. Norris, "Label-free biosensing using a photonic crystal structure," *Optical Express*, vol. 18, 2005, pp. 19120-19128.

[65] C. Pacholski, C. Yu, G. M. Miskelly, D. Godin and M. J. Sailor, "Reflective interferometric Fourier Transform spectroscopy: a self-compensating label-free immunosensor using double-layers of porous SiO_2," *Journal of the American Chemical Society*, vol. 128, 2006, pp. 4250-4252.

[66] S. Jiang, B. Zeng, Y. Liang and B. Li, "Optical fiber sensor for tensile and compressive strain measurements by white-light Fabry-Perot interferometry," *Optical Engineering*, vol. 46, 2007, pp. 136-143.

[67] M. Born and E. Wolf, "Principles of Optics, 7th ed.,"*Cambridge University Press*, 1999.

[68] T. Zhang, S. Talla, Z. Gong, S. Karandikar, R. Giorno and L. Que, "Biochemical sensing with a polymer-based micromachined Fabry-Perot sensor," *Optical Express*, vol. 18, 2010, pp. 18394-18400.

[69] T. Zhang, Z. Gong, R. Giorno and L. Que, "Signal sensitivity and intensity enhancement for a polymer-based Fabry-Perot interferometer with embedded nanostructures in its cavity," *Proceeding of 15th International Conference on Solid-State Sensors, Actuators & Microsystems*, 2009, pp. 2310-2313.

[70] J. Zhao, X. Zhang, C. R. Yonzon, A. J. Haes and R. P. V.Duyne, "Localized surface Plasmon resonance biosensors," *Nanomedicine*, vol. 1, 2006, pp. 219-228.

[71]   J. A. Caravella, D. Wang, S.M. Glaser and A. Lugovskoy, "Structure-guided design of antibodies," *Current Computer-Aided Drug Design*, vol. 6, 2010, pp. 128-138.

[72]   A. Pautsch and G. E. Schulz, "Structure of the outer membrane Protein A transmembrane domain," *Nature structural biology*, vol. 5, 1998, pp. 1013-1017.

[73]   M. Graille, E. A. Stura, A. L. Corper, B. J. Sutton, M. J. Taussig, J. B. Charbonnier and G. J. Silverman, "Crystal structure of a Staphylococcus aureus A domain complexed with the Fab fragment of a human IgM antibody: structural basis for recognition of B-cell receptors and superantigen activity," *Proceedings of the National Academy of Sciences of the United States of America*, vol. 97, 2000, pp. 5399-404.

[74]   K. Singh, H. C. Bajaj, P. Ingole and A. Bhattacharya, "Comparative study of enantioseparation of racemic tryptophan by ultrafiltration using BSA-immobilized and BSA-interpenetrating network polysulfone membranes," *Separation Science and Technology*, vol. 45, 2010, pp. 346-354.

[75]   A. Johansson, G. Blagoi and A.Boisen, "Polymeric cantilever-based biosensors with integrated readout," *Applied Physics Letters*, vol. 89, 2006, p. 173505.

[76]   J. Greener, W. Li, J. Ren, D. Voicu, V. Pakharenko, T. Tang and E. Kumacheva, "Rapid, cost-efficient fabrication of microfluidic reactors in thermoplastic polymers by combining photolithography and hot embossing," *Lab on a Chip*, vol. 10, 2009, pp. 522-524.

[77]   N. S. Chronis, "Lab-on-a-chip mechanical and optical components for the manipulation and detection of biological species," Ph.D thesis, *University of California at Berkeley*, 2004.

[78]   J. Liu, B. Cai, J. Zhu, G. Ding, X. Zhao, C. Yang and D. Chen, "Process research of high aspect ratio microstructure using SU-8 resist," *Microsystem Technologies*, vol. 10, 2004, pp. 265-268.

[79]   B. Wang, J. H. Horton and R. D. Oleschuk, "Sulfonated-polydimethylsiloxane (PDMS) microdevices with enhanced electroosmotic pumping and stability," *Canadian Journal of Chemistry*, vol. 84, 2006, pp. 720-729.

[80]   M. Kucera and J. Lanikova, "Thermal stability of polydimethylsiloxane. II. Formation of stable complexes on basic active centers," *Journal of Polymer Science*, vol. 59, 1962, pp. 79-85.

[81]   S. K. Sia and G. M. Whitesides, "Microfluidic devices fabricated in poly (dimethylsiloxane) for biological studies," *Electrophoresis*, vol. 24, 2003, pp. 3563-3576.

[82] J. C. McDonald and G.M. Whitesides, "Poly(dimethylsiloxane) as a material for fabricating microfluidic devices," *Accounts of Chemical Research*, vol. 35, 2002, pp. 491-499.

[83] R. Zondervan, F. Kulzer, S. B. Orlinskii and M. Orrit, "Photoblinking of rhodamine 6G in poly (vinyl alcohol): radical dark state formed through the triplet," *Journal of Physical Chemistry A*, vol. 107, 2003, pp. 6770-6776.

[84] Z. Jiang, S. Sun, C. Kang, X. Lu and J. Lan, "A new and sensitive resonance-scattering method for determination of trace nitrite in water with rhodamine 6G," *Analytical and Bioanalytical Chemistry*, vol. 381, 2005, pp. 896-900.

[85] A. Liang, Z. Jiang, B. Zhang, Q. Liu, J. Lan and X. Lu, "A new resonance scattering spectral method for the determination of trace amounts of iodate with rhodamine 6G," *Analytica Chimica Acta*, vol. 530, 2005, pp. 131-134.

[86] A. K. Ray, S. Kundu, S. Sasikumar, C. S. Rao, S. Mula, S. Sinha and K. Dasgupta, "Comparative laser performances of pyrromethene 567 and rhodamine 6G dyes in copper vapour laser pumped dye lasers," *Applied Physics B*, vol. 87, 2007, pp. 483-488.

[87] G. Zhu, V. I. Gavrilenko and M. A. Noginov, "Emission of Au nanoparticles with and without rhodamine 6G dye," *Journal of Chemical Physics*, vol. 126, 2007, p. 104503.

[88] Y. Xia and G. M. Whitesides, "Soft lithography," *Annual Review of Materials Science*, vol. 28, 1998, pp. 153-184.

[89] H. Masuda and K. Fukuda, "Ordered metal nanohole arrays made by a two-step replication of honeycomb structures of anodic alumina," *Science*, vol. 268, 1995, pp. 1466-1468.

[90] A. J. Haes and R. P. V.Duyne, "A unified view of propagating and localized surface Plasmon resonance biosensors," *Analytical and Bioanalytical Chemistry*, vol. 379, 2004, pp. 920-930.

[91] T. J. Wang and W. S. Lin, "Electro-optically modulated localized surface Plasmon resonance biosensors with gold nanoparticles," *Applied Physics Letters*, vol. 89, 2006, p. 173903.

[92] J. W. Goodman, "Introduction to Fourier optics," *Roberts & Company Publishers*, 2005.

[93] C. Poweleit, D. H. Naghski, S. M. Lindsay, J. T. Boyd and H. E. Jackson, "Near field scanning optical measurements of optical intensity distributions in semiconductor channel waveguides," *Applied Physics Letters*, vol. 69, 1996, pp. 3471-3473.

[94] S. H. Christiansen, M. Becker, S. Fahlbusch, J. Michler, V. A. Sivakov, G. Andra and R. Geiger, "Signal enhancement in nano-Raman spectroscopy by gold caps on silicon nanowires obtained by vapour-liquid-solid growth," *Nanotechnology*, vol. 18, 2007, p. 035503.

[95] W. Bao, J. Zheng, X. F. Xu, J. G. Cao, Z. J. Yang, N. Ren, Y. Tang, Y. Cao, J. P. Huang and L. W. Zhou, "Short axis contact in the chaining of ellipsoidal particles of polar molecule dominated electrorheological fluid," *Journal of Physics: Condensed Matter*, vol. 22, 2010, p. 324105.

[96] C. Xie, L. Hanson, Y. Cui and B. Cui, "Vertical nanopillars for highly localized fluorescence imaging," *Applied Biological Sciences*, vol. 108, 2011, pp. 3894-3899.

[97] Y. Choi, J. Kwak and J. Park, "Nanotechnology for early cancer detection," *Sensors*, vol. 10, 2010, pp. 428-455.

[98] M. Ferrari, "Cancer nanotechnology: opportunities and challenges," *Nature Reviews Cancer*, vol. 5, 2005, pp. 161-171.

[99] S. Food, M. Pirrung, L. Stryer, A. Lu and D. Solas, "Light-directed, spatially addressable parallel chemical synthesis," *Science*, vol. 251, 1991, pp. 767-773.

[100] L. Farwell and V. Joshi, "DNA sequencing of cancer-related genes for biomarker discovery," *Methods in Molecular Biology*, vol. 520, 2009, pp. 205-220.

[101] R. C. Zangar, D. S. Daly and A. M. White, "ELISA microarray technology as a high-throughput system for cancer biomarker validation," *Expert Review of Proteomics*, vol. 3, 2006, pp. 37-44.

[102] L. H. Choe, B. G. Werner and K. H. Lee, "Two-dimensional protein electrophoresis: from molecular pathway discovery to biomarker discovery in neurological disorders," *NeuroRx*, vol. 3, 2006, pp. 327-335.

[103] L. A. Bradley, E. H. John and L. D. Kevin, "The role of mass spectrometry in biomarker discovery and measurement," *Current Drug Metabolism*, vol. 7, 2006, pp. 525-539.

[104] E. F. Petricoin, V. Rajapaske, E. H. Herman, A. M. Arekani, S. Ross, D. Johann, A. Knapton, J. Zhang, B. A. Hitt, T. P. Conrads, T. D. Veenstra, L. A. Liotta and F. D. Sistare, "Toxico proteomics: serum proteomic pattern diagnostics for early detection of drug induced cardiac toxicities and cardioprotection," *Toxicologic Pathology*, vol. 32, 2004, pp. 1-9.

[105] O. Stoevesandt, M. Taussig and M. He,"Protein microarrays: high-throughput tools for proteomics," *Expert Review of Proteomics*, vol. 6, 2009, pp. 145-157.